Numerical and experimental investigations on the influencing factors of dry granular materials collapse

Von der Fakultät für Bauingenieurwesen

der Rheinisch-Westfälischen Technischen Hochschule Aachen

zur Erlangung des akademischen Grades eines Doktors der Ingenieurwissenschaften

genehmigte Dissertation

vorgelegt von

Yucheng Li

Berichter: Univ.-Prof. Dr. Raul Fuentes

Univ.-Prof. Dr. Miguel Angel Cabrera

Tag der mündlichen Prüfung: 11.07.2025

Table of Contents

List of Figures

List of Tables

List of Symbols

a	[-]	Aspect ratio
r_0	[m]	Initial radius
r_∞	[m]	Deposit run-out distance
R^* or L^*	[m]	Normalized run-out distance
ΔL	[km]	Travel length by the front landslide
L_∞	[km]	Total travel length of the landslide
h_0	[m]	Initial height
h_∞	[m]	Final height
H^*	[-]	Scaled final height
Δp	[mm]	Particle spacing of SPH sample
μ	[-]	Substrate friction coefficient
ρ	[kg/m^3]	Mass density of granular materials
v	[-]	Poisson's ratio
φ	[°]	Angle of friction
E	[MPa]	Young's modulus
G	[MPa]	Shear modulus
K	[MPa]	Bulk modulus
S	[-]	Sphericity
A_r	[-]	Particle aspect ratio
C_V	[-]	Convexity
R	[-]	Roundness
E_0	[J]	Initial potential energy
E_P	[J]	Potential energy
E_I	[J]	Internal energy
E_D	[J]	Basal dissipated energy
E_K	[J]	Kinetic energy
E_{kt}	[J]	Transitional kinetic energy
E_{kr}	[J]	Rotational kinetic energy

E_{DA}	[J]	All dissipated energy
g	[m/s²]	Gravitational acceleration
t_∞	[s]	Collapse time
τ_c	[s]	Characteristic time
α_{repose}	[°]	Angle of repose
θ	[°]	Flow mobility angle
θ'	[°]	Modified flow mobility angle
D_f	[-]	Fractal dimension
D_2	[-]	The second Spherical Harmonic descriptor
η	[-]	Damping ratio
ε	[-]	Coefficient of restitution
I_{AM}	[-]	Average friction mobilisation index

Abstract

Granular materials are widely encountered in both nature and industry, significantly impacting our daily lives. Although substantial progress has been made in experimental and theoretical studies over the past two decades, several influencing factors remain insufficiently understood. In this work, we aim to analyse some uncertain factors influencing the granular column collapse phenomenon.

First, we investigate the role of basal friction in granular column collapse through a series of numerical simulations using Smoothed Particle Hydrodynamics (SPH). Our study systematically examines the influence of basal friction on the deposit geometry, proposing an expression to predict run-out distance. The numerical results are compared with experimental findings from previous studies. Additionally, we analyse the effects of basal friction on final height, deposit regime transitions, and energy conversion, offering new insights into plate-grain friction mechanism.

Second, as space exploration advances, understanding the collapse of granular materials under non-Earth gravity conditions becomes increasingly relevant. We investigate the effects of varying gravity levels on the collapse behaviour of granular columns, using dimensional analysis to assess how different gravity levels influence material behaviour. Two models are proposed to predict collapse time, accounting for gravitational acceleration (g). Our findings suggest that gravity has minimal influence on deposit run-out distance and final height, supported by observations of natural landslides across the Solar System. Moreover, as the aspect ratio increases, both the flow mobility angle (θ) and the modified flow mobility angle (θ') decrease, independent of gravity level. Our small-scale results align with large-scale results across varying gravity levels, indicating that the collapse run-out depends on sample volume and initial potential energy rather than gravity.

Third, we address the limitations of previous studies on particle shape, which often were coupled with other non-particle shape factors (such as volume and stiffness) or used unrealistic particle geometries (primarily consisting of convex shapes without concave features). We utilized spherical harmonic (SH) functions and a high-precision 3D printing machine to fabricate ideal particles, isolating particle shape effects on flow dynamics. Subsequently, we designed a laboratory platform to investigate the influence of particle shape on flow dynamic properties. We also input the STL files of particles generated by the SH functions into Discrete Element Method (DEM) software for numerical analysis. Our study explored the effects of particle shape (varying in D_f and D_2, where D_f and D_2 are obtained by fitting the results of spherical harmonic descriptors and spherical harmonic degree) on deposit morphology, deposit geometry (run-out distance, final height, and its related scaling laws constants), energy conversion, and interlocking ability during collapse. Additionally, we quantitatively analysed the influence of particle geometric parameters, such as sphericity, particle aspect ratio, convexity, and roundness on deposit run-out distance, final height, and flow mobility. Furthermore, we proposed a model to directly predict run-out distance

using particle relative roughness (R_r), derived from D_f and D_2, which shows strong agreement with numerical results. This is the first attempt to predict run-out distance from a particle shape perspective.

Our findings enhance the understanding of dry granular collapse phenomenon and its underlying mechanisms. This research serves as a valuable reference for the application of granular materials in geotechnical and other related fields.

Kurzfassung

Granulare Materialien finden sich sowohl in der Natur als auch in der Industrie und haben einen erheblichen Einfluss auf unser tägliches Leben. Trotz des signifikanten Fortschritts in experimentellen und theoretischen Studien in den letzten zwei Jahrzehnten bleiben mehrere Einflussfaktoren unzureichend verstanden. In dieser Arbeit zielen wir darauf ab, einige unsichere Faktoren zu analysieren, die das Phänomen des Kollapses granularer Säulen beeinflussen.

Zunächst untersuchen wir die Rolle der Grundreibung beim Kollaps granularer Säulen durch eine Reihe numerischer Simulationen unter Verwendung der Methode der geglätteten Partikel-Hydrodynamik (SPH). Unsere Studie prüft systematisch den Einfluss der Grundreibung auf die Geometrie des Ablagerungsbereichs und schlägt einen Ausdruck zur Vorhersage der Ablaufsdistanz vor. Diese Ergebnisse werden mit experimentellen Befunden aus früheren Studien verglichen. Darüber hinaus analysieren wir die Auswirkungen der Grundreibung auf die Endhöhe, den Übergang des Ablagerungsregimes und die Energieumwandlung und bieten neue Einblicke in die Reibung zwischen Platten und Körnern.

Zweitens, da die Weltraumforschung fortschreitet, wird das Verständnis des Kollapses granularer Materialien unter Bedingungen mit nicht-erdgebundeter Schwerkraft zunehmend relevant. Wir untersuchen die Auswirkungen variierender Schwerkraftniveaus auf das Kollapsverhalten granularer Säulen und nutzen die dimensionsanalytische Methode, um zu bewerten, wie unterschiedliche Schwerkraftniveaus das Materialverhalten beeinflussen. Zwei Modelle werden vorgeschlagen, um die Kollapszeit unter Berücksichtigung der Gravitationsbeschleunigung (g) vorherzusagen. Unsere Ergebnisse legen nahe, dass die Schwerkraft einen minimalen Einfluss auf die Ablaufsdistanz und die Endhöhe der Ablagerungen hat, unterstützt durch Beobachtungen natürlicher Erdrutsche im gesamten Sonnensystem. Darüber hinaus zeigen wir, dass mit zunehmendem Seitenverhältnis sowohl der Fließmobilitätswinkel (θ) als auch der modifizierte Fließmobilitätswinkel (θ') abnehmen, unabhängig vom Schwerkraftniveau. Unsere Ergebnisse im kleinen Maßstab stimmen mit Ergebnissen im Großmaßstab über verschiedene Schwerkraftniveaus hinweg überein, was zeigt, dass der Kollapsbereich von dem Probenvolumen und der anfänglichen potentiellen Energie abhängt, nicht von der Schwerkraft.

Drittens gehen wir auf die Einschränkungen früherer Studien zur Partikelform ein, die häufig mit anderen Faktoren, die nicht die Partikelform betreffen (wie Volumen und Steifigkeit), gekoppelt oder unrealistische Partikeldesigns verwendet haben (hauptsächlich bestehend aus konvexen Formen ohne konkave Merkmale). Wir verwendeten sphärische harmonische (SH) Funktionen und eine hochpräzise 3D-Druckmaschine, um ideale Partikel zu fertigen und die Effekte der Partikelform auf die Fließdynamik zu isolieren. Anschließend entwarfen wir eine Laborplattform, um den Einfluss der Partikelform auf die dynamischen Fließeigenschaften zu untersuchen. Wir

haben auch STL-Dateien von durch die SH-Funktionen erzeugten Partikeln in Software für die diskrete Elementemethode (DEM) eingegeben, um eine numerische Analyse durchzuführen. Unsere Studie erforschte die Auswirkungen der Partikelform (variierend in D_f und D_2, die aus der Anpassung der Ergebnisse der sphärischen harmonischen Deskriptoren und der sphärischen harmonischen Ordnung abgeleitet sind) auf die Morphologie der Ablagerung, die Geometrie der Ablagerung (Ablaufsdistanz, Endhöhe und die damit verbundenen Skalierungsgesetze von Konstanten), die Energieumwandlung und die Verzahnungsfähigkeit während des Kollapses. Darüber hinaus analysierten wir quantitativ den Einfluss von Partikelformparametern wie Sphärizität, Partikelseitenverhältnis, Konvexität und Rundheit auf die Ablaufsdistanz, die Endhöhe und die Fließmobilität. Darüber hinaus haben wir ein Modell zur direkten Vorhersage der Auslaufstrecke unter Verwendung der relativen Rauheit der Partikel (R_r) vorgeschlagen, das aus D_f und D_2 abgeleitet wurde und eine gute Übereinstimmung mit den numerischen Ergebnissen zeigt. Dies stellt den ersten Versuch dar, die Ablaufsdistanz aus der Perspektive der Partikelform vorherzusagen.

Unsere Ergebnisse erweitern das Verständnis des Phänomens des Kollapses trockener Granulate und seiner zugrunde liegenden Mechanismen. Diese Forschung dient als wertvolle Referenz für die Anwendung granularer Materialien in der Geotechnik und in anderen verwandten Bereichen.

1 Introduction

1.1. Background

Granular materials are widely encountered in both nature and daily life, including riverbed sediments, landslides, debris flows, aeolian deposits on Mars or the Moon, as well as industrial materials such as sand, gravel, and grains. When subjected to external disturbances or internal instabilities, these materials can undergo rapid collapse, triggering complex dynamic processes with significant impacts on the environment and human society. Understanding the collapse mechanisms of granular materials is essential for predicting and mitigating natural disasters.

Over the past two decades, significant progress has been made in understanding granular flows through experiments and theoretical analysis. A widely accepted conclusion (Lube et al., 2004, Lajeunesse et al., 2004, Szewc, 2017) is that the collapse behaviour of granular flow is primarily governed by initial aspect ratio, a (defined as $a = h_0/r_0$, where h_0 is the initial height and r_0 is the initial radius). Additionally, parameters such as initial column porosity (Fern and Soga, 2016), particle shape (Tapia-McClung and Zenit, 2012, Wei et al., 2018, Hoang and Nguyen, 2023), inter-particle friction (Lai et al., 2023), particle size (Lai et al., 2017, Cabrera and Estrada, 2021, Su et al., 2022), grain size effects (Warnett et al., 2014, Cabrera and Estrada, 2019, Man et al., 2021b), cohesive materials collapse (Jing et al., 2018a, Zhu et al., 2022), and collapse in water (Thompson and Huppert, 2007, Jing et al., 2018b, Polanía et al., 2022) have been extensively investigated. Researchers have also explored the impact of boundary geometry parameters, such as erodible surface (Crosta et al., 2009, Mangeney et al., 2010), air fluidization (Roche et al., 2011), lateral wall width (Zhang et al., 2021b) and cross-section shape (Teng Man, 2022) on granular column collapse. One common application of these studies is the validation of constitutive models using the granular collapse phenomenon (Mast et al., 2015, Peng et al., 2015, Szewc, 2017, Fávero and Borja, 2018). However, there are still some influencing factors that need to be understood. This work aims to analyse some of these uncertainties in the granular column collapse phenomenon.

First, the role of basal friction in granular column collapse remains debated. Some researchers argue that it has no significant effect (Lube et al., 2004, Frank, 2006), while others suggest it does influence the collapse behaviour (Sheikh et al., 2021). Therefore, a systematic investigation of the effect of basal friction on collapse behaviour are necessary to clarify its role in the collapse mechanism.

Second, as space exploration advances, the prospect of exploring resources on other planets and even considering human settlement becomes more plausible. Understanding granular collapse under non-Earth gravity conditions is an emerging and promising field of study. While it is well-known that higher gravity levels accelerate the free fall of particles, there is a lack of systematic

studies evaluating this acceleration effect. Additionally, the influence of gravity on the collapse behaviour, such as run-out distance and deposit morphology, which are of great concern in natural hazards like landslides, still requires further understanding.

Third, many studies have investigated the influence of particle shape through experimental and numerical methods, focusing on aspects such as flow regimes, mobility, and deposition. In these studies, particle shape is often coupled with other factors, including density, size, and stiffness. Although some numerical studies use idealized particle shapes to isolate the effect of shape from other mechanical parameters, these particles are typically unrealistic and consist mostly of convex shapes without concave features. Moreover, quantitative analysis, such as comparing particles of equal volume, is often lacking. As a result, the effects of particle geometric parameters (e.g., convexity, aspect ratio, and roundness) on flow dynamics and morphology remain unclear. There is also a lack of formula that predicts the final run-out distance directly from the particle shape perspective.

1.2. Research contribution

In this study, we investigated the effects of uncertain influencing factors on the granular material collapse mechanism. Our main contributions are summarized as follows:

(1) The effect of basal friction on the collapse of granular column was investigated. We developed a series of Smoothed Particle Hydrodynamics (SPH) models with varying basal friction to systematically investigate the effect of base friction on the collapse mechanism. An expression for predicting the run-out distance, accounting for different friction coefficients, was proposed. Additionally, the effects of basal friction on final height, deposit regime transition, and energy conversion were investigated, providing new insights into the effect of plate-grain friction dynamics.

(2) The effect of gravity level on the collapse of granular column was investigated. A dimensional analysis of system scaling factors was conducted to assess the impact of varying gravity levels. Two predictive models were proposed to estimate collapse time, both considering the scaling relationship with gravitational acceleration (g). The effects of gravity on deposit run-out distance and final height were further examined and validated through comparisons with natural landslides within the Solar System. By comparing our simulation results and current experimental results with natural landslide occurrences, a multi-scale analysis was achieved. Furthermore, a modified mobility angle (θ') was introduced to effectively eliminate the influence of initial geometry when describing the flow mobility of granular materials.

(3) More realistic particles (with both concave and convex features) were used to analyse the collapse responses. The results reveal that particle shape significantly affects velocity fields, deposit responses, and energy dissipation. A proposed friction mobilization index (I_{AM}) highlights the interlocking effect of different shaped particles, demonstrating that the interlocking ability increases with particle irregularity (i.e., an increase in D_f, D_2 or R_r), but diminishes at higher columns, despite variations in particle shape. Additionally, the effects of particle geometric

parameters (e.g., sphericity, convexity, and roundness) on run-out distance and flow mobility are systematically analysed. Furthermore, a predictive model was developed to estimate run-out distance based on relative particle roughness (R_r), showing strong agreement with numerical results. This work represents the first attempt to predict run-out distance from a particle shape perspective.

1.3. Dissertation structure

This dissertation has been prepared according to the guidelines of the faculty of civil engineering at RWTH Aachen University for obtaining the degree of Doctor of Engineering. Some parts of these chapters have been either published or submitted for possible publication in peer-review journals and international conferences. The dissertation includes 7 chapters, which present a system study of the influencing factors of granular column collapse.

The dissertation is organized as follows:

Chapter 1 presents a brief background, outlines the research contribution, and describes the structure of this dissertation.

Chapter 2 introduces the existing influencing factors, relevant literature, and recent developments regarding the granular column collapse phenomenon.

In Chapter 3, we systematically analyse the effect of basal friction on gravity-driven granular column collapse using a validated Smoothed Particle Hydrodynamics (SPH) model. By fitting our simulation results for various basal friction coefficients μ, we propose a modified model to predict run-out distance that incorporates the basal friction coefficient. This model considers two extreme cases, i.e., $\mu = 0$ and $+\infty$, to ensure physical consistency. Additionally, we analyse the effect of basal friction on final height, deposit regime transition, and energy conversion, providing new insights into the effect of plate-grain friction.

In Chapter 4, we investigate the effect of gravity level on granular column collapse via SPH method based on the Mohr-Coulomb model. After validating our model against existing experimental studies, we conduct a dimensional analysis of the system scaling factors to assess the influence of varying gravity levels. We analyse the effect of gravity on collapse time and propose two models to predict collapse time, both considering the scaling relationship with gravitational acceleration (g). Furthermore, we examine the effects of gravity on deposit run-out distance and final height, comparing them with existing landslide data from different planets to explore the influence of gravity conditions across different scales. Additionally, we introduce a modified mobility angle (θ') to effectively eliminate the influence of initial geometry in describing material flow mobility.

In Chapter 5, we employ spherical harmonics (SH) functions to represent and reconstruct the 3D surface of granular material particles, which are then fabricated using a high-precision 3D printing device. Each printed particle exhibits both concave and convex properties. This method enables full control over shape parameters, such as particle sphericity, while maintaining a constant

volume, ensuring that particle shape is the sole variable parameter. Following this, we design an experimental platform to conduct granular column collapse experiments, investigating the effects of particle shape parameters on flow dynamics, the centre of mass of flows, and deposit geometry. We further examine the angle of repose of the printed particles.

In Chapter 6, we import the particle STL files generated by SH functions into DEM software to achieve a more realistic particle representation. After validating our numerical model with the experimental results from Chapter 5, we conduct numerical investigations into the effects of particle shape on collapse behaviour. Our study explored how particle shape influences deposit morphology, geometry, and energy conversion. A proposed friction mobilization index (I_{AM}) highlights the interlocking effect of different shaped particles. We also quantitatively analyse the effect of particle geometric parameters (sphericity, particle aspect ratio, convexity, and roundness) on the collapse run-out distance and flow mobility. Additionally, we propose a model to directly predict run-out distance based on particle shape parameter R_r.

Chapter 7 summarizes the research activities conducted in this study and provides an outlook for further research in this area.

All applied abbreviations or notations are presented in Appendix of this thesis.

2 State of the Art on Factors Influencing the Collapse of Granular Materials

This thesis investigates the factors influencing the collapse behaviour of dry granular materials, a topic of considerable significance in geophysical processes. Although extensive research has been conducted over the past two decades, many findings are limited by constraints in experimental setups and the current state of numerical modelling techniques. These limitations restrict the ability to perform precise quantitative analyses, complicating the isolation of collapse behaviour from confounding factors. As a result, certain influencing factors remain insufficiently understood and require further investigation. One such factor is the role of basal friction in collapse dynamics, which continues to be debated within the field. Accurately quantifying particle-surface friction under laboratory conditions remains a significant challenge. While some studies report that basal friction has negligible influence, others suggest that it exerts a subtle yet measurable effect. This chapter provides a systematic review of the key factors governing the collapse of granular materials and examines existing research gaps. Sections 2.1 through 2.5 explore the primary factors affecting granular collapse, while Section 2.6 discusses additional considerations that may contribute to collapse behaviour.

2.1. Aspect ratio

To better understand the collapse behaviour of granular flows, Lube et al. (2004) and Lajeunesse et al. (2004) conducted fundamental experiments. They filled cylindrical columns with granular materials and allowed them to spread on a horizontal surface under gravity. Their results revealed that the collapse characteristic (e.g., flow pattern, run-out distance, and final height) is governed by the initial aspect ratio, a (defined as $a = h_0/r_0$, where h_0 is initial height and r_0 is initial radius of the column). Depending on the value of a, two distinct regimes can be distinguished. For low aspect ratios, the flow is friction-dominated. In this regime, the column's edges fall while leaving its inner part relatively undisturbed. During this stage, a simple linear relationship between the run-out distance and the initial aspect ratio has been widely reported (Lube et al., 2004, Lajeunesse et al., 2004, Szewc, 2017). As a increases, the governing mechanism shifts. The shear plane gradually moves inwards until the entire free surface collapses, and the spreading of the granular material becomes influenced by pressure gradient. In this regime, the run-out distance follows a power law relationship with the aspect ratio. The final deposit morphology also varies with the initial aspect ratio. For samples with low a, the deposits typically form truncated cone shape in three dimensions (3D) or trapezoid shapes in two dimensions (2D). In contrast, samples with high a trend to form conical or triangular shaped deposits.

The aspect ratio (a) is a key dimensionless parameter describing the initial geometry of the sample, and it is now widely accepted that deposit geometry is governed by this ratio (Lube et al., 2004,

Lajeunesse et al., 2004, Lajeunesse et al., 2005, Balmforth and Kerswell, 2005, Staron and Hinch, 2007, Thompson and Huppert, 2007). Different deposit morphologies have been observed in both experiments and simulations, and these are significantly influenced by a.

The fundamental studies on deposit geometry analysis conducted by Lube et al. (2004), who used five types of grains (different particle sizes, different particle shapes), and Lajeunesse et al. (2004) who used two types of glass beads (particles sizes, same particle shape). Both studies propose a bilinear relationship between the initial aspect ratio and the normalized run-out distance or rescaled final height, which can be expressed through scaling law of the form $R^* or\ H^* = \alpha \cdot a^{\beta}$ (where the coefficient α and exponent β are obtained from experimental results), as shown in Equations (2.1), (2.2), and (2.3). The relevant experimental and numerical results are summarized in Table 2-1.

$$R^* = \frac{r_\infty - r_0}{r_0} = C_\alpha a, \qquad when\ (a \le a_{CL}) \tag{2.1}$$

$$R^* = \frac{r_\infty - r_0}{r_0} = C_\beta a^{c_{EL}}, \qquad when\ (a \ge a_{CL}) \tag{2.2}$$

$$H^* = \frac{h_\infty}{r_0} = C_\gamma a^{c_{EH}}, \qquad when\ (a \ge a_{CH}) \tag{2.3}$$

where the critical aspect ratio (a_{CL} and a_{CH}) and scaling constants (C_α, C_β, and C_γ) in the above scaling laws are determined from the regression analysis of the deposit geometry results.

Table 2-1 Summary of scaling law literatures (Exp. is experiment, and Num. is numerical simulation)

Study	Condition	Scaled normalized run-out distance R^* or L^*				Scaled retained height H^*		
		a_{CL}	C_α	C_β	c_{EL}	a_{CH}	C_γ	c_{EH}
Lube et al. (2005)	Quasi 2D, Exp.	<1.8 or >2.8	1.6	2.2	2/3	1.15	1	2/5
Lajeunesse et al. (2005)	Quasi 2D, Exp.	3	1	1	2/3	0.7	1	1/3
Lacaze. et al. (2008)	Quasi 2D, Exp.	2.2 to 4.0	-	1	0.72 ± 0.03 to 0.81 ± 0.03	-	-	-
Staron and Hinch (2005)	2D, Num.	2	2.5	3.25	0.705 ± 0.022	$1 \le a_{CH} \le 10$ or $a_{CH} \ge 10$	0.65 or 1.45	0.35 or 0
Nguyen et al. (2020)	2D, Num.	3	2.62	3.32	0.76	-	-	-
Hoang and Nguyen (2023)	Quasi 2D, Num. (same isotropic particles (n=1)	3 (m=2)	1.4830	2.0760	0.6872	1	0.9838	0.4546
		3.5 (m=4)	1.3346	2.0453	0.6586	>1 & <1.5	1.0618	0.4879

	with different blockiness, m)	4 (m=6)	1.2804	2.1443	0.6156	>1 & <1.5	1.0768	0.4840
Lube et al. (2004)	3D, Exp.	1.7	1.24	1.6	1/2	1		
Lajeunesse et al. (2004)	3D, Exp.	3	1	1	1/2	0.74	0.74	0
Trepanier and Franklin (2010)	3D, Exp.	1.1 ± 0.3	-	1	1.2 ± 0.1 ($a \leq a_{CL}$) 0.6 ± 0.1 ($a \geq a_{CL}$)	-	-	-
Szewc (2017)	3D, Num.	1.7	0.72	1.02	3/5	-	-	-
Fávero and Borja (2018)	3D, Num.	1.7	1.11	1.66	0.48	1	0.87	0.16

2.2. Inter-particle friction

In terms of effects of inter-particle friction on the dynamics of the granular materials, many researchers have conducted experimental studies and numerical simulations. Two distinct perspectives exist regarding the influence of inter-particle friction. Staron and Hinch (2007) investigated the role of inter-particle friction on dynamics using 2D DEM simulations. Their results showed that the run-out distance of cases with an inter-particle friction coefficient of 0.01 was nearly three times larger than for cases with a friction coefficient of 1. However, this difference is small when compared to the factor of 100 between the two friction values. They concluded that inter-particle friction does not change the dependence of the run-out distance on a, which dominates the spreading dynamics rather than the specifics of the interactions between the grains. Nevertheless, lower inter-particle friction values led to large increased spreading distances and reduced final height.

Using Finite Element (FE), Particle Finite Element Method (PFEM), and Material Point Method (MPM) numerical simulations, Crosta et al. [29], Zhang et al. [30] and Mast et al. [31] observed a similar trend, where the macroscopic effective friction in continuum models significantly affects granular column collapse. Lube et al. (2004) found no significant differences in experimental results when using various types of particles, such as sand, salt, rice, couscous, and sugar, suggesting that the influential factors are complex and cannot solely be attributed to the particle friction coefficient. Conversely, 2D DEM simulations by Zenit (2005) indicated that inter-particle friction does not significantly affect the deposit shape. Lo et al. (2009) observed that the collapse dynamics are nearly independent of inter-particle friction in their 3D DEM simulations. Owen et al. (2009) used a slow-motion releasing wall with constant speed instead of instant release, found that final deposits were invariant to changes in inter-particle friction. The relevant results regarding the effects of inter-particle friction from physical experiments or numerical simulations are given in Table 2-2.

Table 2-2 Summary for physical experiments (Exp.) or numerical simulations (Num.) of granular column collapse (improved from ref. Lai et al. (2023))

Source	Condition	r_0/d	a	μ_p	Effect conclusion
Lube et al. (2004)	3D Exp.	12.7-303	0.1-10	0.58,0.60,0.67,0.70 (Macroscopic friction angle)	Uncertain due to other influential factors
Zenit (2005)	2D DEM Num.	-	0.1-10	0.30 & 0.57	Not significantly
Staron and Hinch (2007)	2D DEM Num.	10-45	0.9	0.05, 0.10, 0.50, 1.0 & 2.0	Significantly
Lo et al. (2009)	2D DEM Num.	Approximately 10	5	0.2, 0.4, 0.6, 0.8	Not significantly
Crosta et al. (2009)	2D FEM Num.	-	0.6-20	0.70 & 0.84 (Macroscopic friction angle)	Significantly
Owen et al. (2009)	2D/3D DEM Num.	-	1.5-5.5	0.42, 0.47, 0.52, 0.57 & 0.62	Negligible
Mast et al. (2015)	2D MPM Num.	-	0.25-10	0.47-1.19 (Macroscopic friction angle)	Significantly
Lai et al. (2023)	3D DEM Num	60 or 80	0.25-8	0.1-1.0	Significantly

2.3. Basal friction

Through a comprehensive literature review, only a handful of studies are dedicated to the effect of the friction coefficient between the substrate and column grains; herein called basal friction coefficient, μ. This limited attention has led to a lack of consensus on whether it has an effect and where exactly it is most prominent.

In experimental research, Goujon et al. (2003) conducted experiments to study the effect of roughness of the inclined plane on the dynamics of granular flows with different-sizes beads flowing over a planes where a layer of the same beads was glued. It appears from these experiments that the relative roughness, defined as the ratio between the size of flowing beads and the size of glued beads is critical. They also showed that the run-out distance depended on this relative roughness. However, Lube et al. (2004) reported that the roughness of the ground made no significant effect on the deposit results. Lajeunesse et al. (2004) found that for larger aspect ratios models, roughness had no effect on the final run-out distance, and only had influence on the final height. Roche et al. (2011) generated a column of particles initially fluidized with air to eliminate the inter-particle friction in the granular columns. They concluded that fluidization reduces contacts between the grains and increase the coefficient α ($R^* = \alpha \cdot a^{\beta}$) compared to dry flows but it has no effect on the exponent β. However, fluidized particles also reduce the friction between column grains and run-out plate although they did not analyse this.

In numerical studies, Cleary and Frank (2006b) used the three-dimensional discrete element method (DEM) to study the effect of the static friction coefficients (μ_s=0.4 and μ_s=0.65) on the collapse of granular column with a fixed aspect ratio of a = 1.91. They discovered that the run-out distance and final deposit height remain unaffected by the static friction coefficient. Zhang et al. (2016) studied the quasi-static collapse of two-dimensional granular columns using particle finite element method (PFEM) simulations. They reported that the change of basal roughness not only significantly influences the collapse process quantitatively, but may lead to new failure patterns that have not been observed in the experiments of quasi-static collapse. Sheikh et al. (2021) proposed two frictional boundary algorithms (penetration method and momentum method) of SPH and then test them to investigate the effect of basal friction (μ = 0.0, 0.2, 0.4 and 0.9) on the collapse behaviour of granular columns. Their results show that the flow of a collapsing granular column can be divided into three flow regimes and the interaction of collapsing regimes is affected by basal friction. Also, their results show that the normalized run-out distance increases as μ decrease and this effect becomes negligible for large aspect ratios. However, they do not have a systematic analysis of μ and do not incorporate it into the formula for predicting run-out distance. Furthermore, with consideration of both inter-particle friction and particle-boundary friction, Man et al. (2021a) proposed a dimensionless number, the effective aspect ratio, $\alpha_{eff} = \sqrt{\frac{1}{\mu_w+\beta\mu_p}}\left(\frac{h_0}{r_0}\right)$ (where μ_w is the basal friction coefficient, μ_p is the inter-particle friction coefficient, and β is a fitting parameter) to analyse the deposit morphology of the granular column collapse. However, they did not consider the extreme conditions (zero and +∞) of the particle-boundary friction, which resulted in findings that only show one transition zone between three types of deposit regimes. Despite the mounting evidence, no study has yet systematically investigated the basal friction coefficient influence on collapse behaviour.

2.4. Gravitational acceleration

As space exploration advances, the prospect of utilizing resources from other planets and facilitating human immigration is becoming increasingly viable. Humanity's understanding of outer planets is poised to expand significantly with ongoing national space programs, including National Aeronautics and Space Administration (NASA) ’s Artemis program, which aims to return to the moon and send astronauts to Mars. On 15 May 2021, China’s Zhu Rong rover successfully landed on Mars, making China the second country to operate a Mars rover. Through these endeavours, humanity has deepened its understanding of space and the origins of planets. However, landslides occurring on various celestial bodies pose significant threats to both human activities and extraterrestrial exploration (see Figure 2.1). Therefore, understanding granular materials collapse under different gravitational conditions has some several potential applications, including: (1) direct impacts on scientific discoveries; (2) insights into planetary surface processes, such as the formation of impact craters, sand dunes, granular flows, pyroclastic cones, and scree slopes; and (3) the design of stable foundations for structures, prediction of slope behaviour, and mitigation of landslide risks.

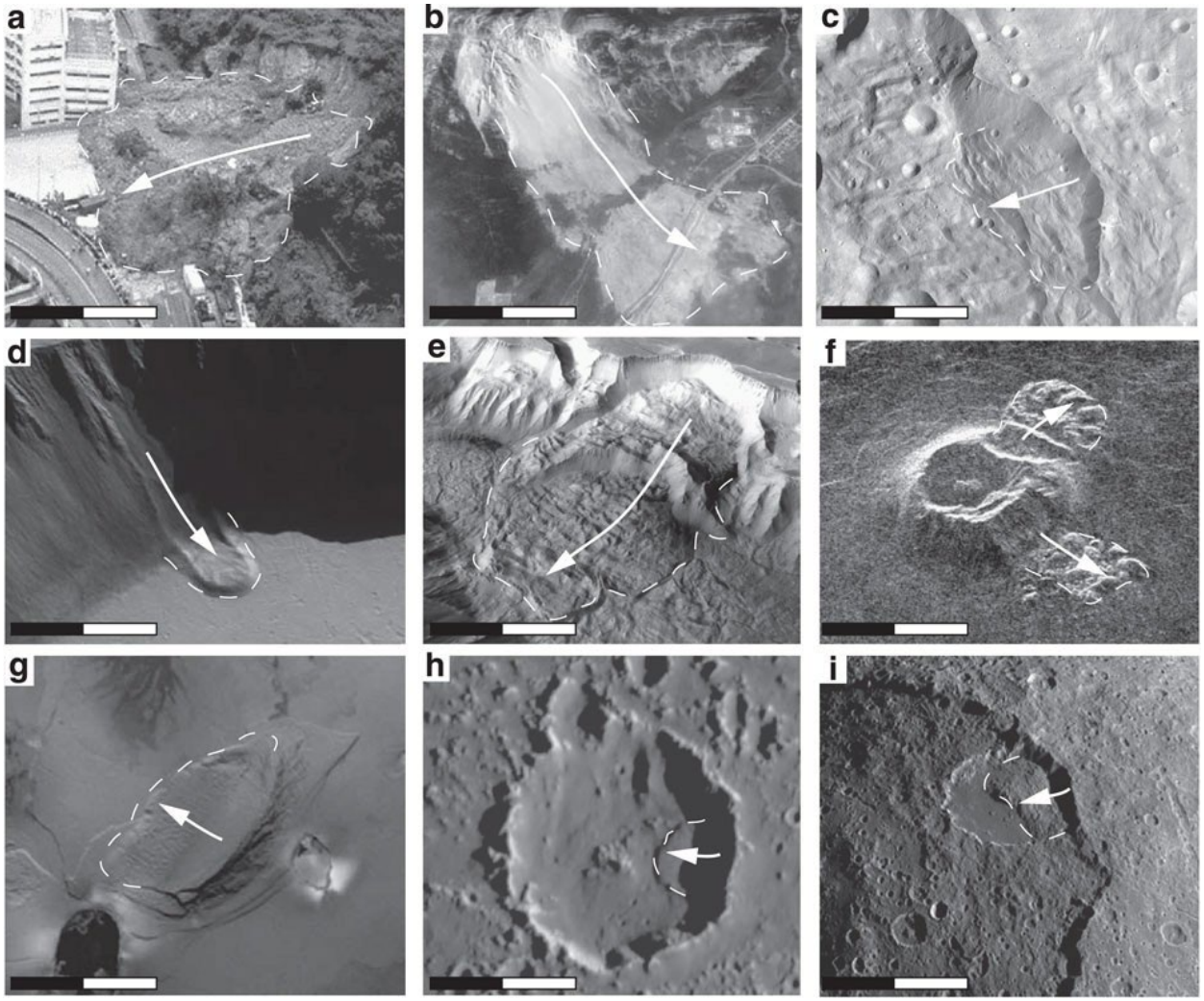

Figure 2.1 Examples of landslides observed in the Solar System. Sizes range from tens of metres to hundreds of kilometres. On Earth: (a) Fei Tsui, Hong Kong (scale bar, 30m); (b) Frank Slide, Canada (scale bar, 1km). On Vesta (c) in the South pole region (scale bar, 80km). On Mars: (d) Olympus Mons (scale bar, 2km) and (e) Tithonium Chasma (scale bar, 10km). On Venus: (f) in the Navka Region (scale bar, 25km). On Jupiter's moons: (g) Euboea Montes on Io (scale bar, 100km). (h) Inside Callisto's crater (scale bar, 10km). On Saturn's moons: (i) Malun Crater on Iapetus (scale bar, 100km). Deposits and sliding direction are highlighted with dashed white lines and arrows, respectively. Pictures of these landslides are reported in Lucas et al. (2014).

In terms of research, understanding the properties of granular material (e.g., angle of repose, collapse behaviour) under varying gravity levels is crucial for space exploration. Several studies have investigated the dependence of the dynamic angle of repose on gravity; however, no consensus exists. While P. G. Hofmeister (2009) and Kleinhans et al. (2011) demonstrated a dependence on gravity, Nakashima et al. (2011) and Atwood‐Stone and McEwen (2013) found no such relationship. This controversy was addressed by Marshall et al. (2018), whose classical passive earth pressure experiments conducted during reduced gravity flights showed that the angle of repose is independence of gravity. Inspired by these previous studies on the angle of repose tests, we focus on the collapse behaviour of granular materials. The first models for granular flows in centrifuge systems were based on granular flow in a rotating drum (Arndt et al., 2006). Recent

research has expanded these flow configurations to include sliding down on curved channels (Bowman et al., 2010, Gue. et al., 2010) and studying the flow rate during the discharge of a silo (Dorbolo et al., 2013). Cabrera and Wu (2017) investigated the dynamic of granular flows under centrifugal acceleration, revealing that as the slope angle and equivalent centrifuge acceleration increase, the flow velocity increase and flow height decreases asymptotically until a constant height. Compared to experimental studies, numerical simulations offer a more economical and accessible approach for investigating the effect of varying gravity levels. Cabrera et al. (2020) investigated the scaling principles for granular flow in a centrifugal acceleration field using discrete element method (DEM). Results show that granular flows scale consistently only when the Coriolis acceleration is negligible, and are severely altered otherwise. Recently, Yang et al. (2024) conducted SPH simulations to investigate granular flow under reduced-gravity conditions (0.01g-0.3g). Their findings indicate that at the steady flow time-scale, the run-out distance positively correlates with gravity. Zhang et al. (2024) employed centrifuge modelling to study dry granular collapse under deflective Coriolis conditions. Their results suggest that to mitigate the impact of Coriolis acceleration, a larger initial column height is recommended, specifically with height/width ratio exceeding 1. This implies that previous experimental studies, such as that by Hofmeister et al. (2009), may have been influenced by Coriolis effects. Zheng et al. (2024) performed DEM simulations of granular chute flow under varying inclination angles and gravitational conditions. By analysing the macroscopic flow velocity, stress and rheology of granular materials after reaching steady-state flow, they analysed the influence mechanism of gravitational environment on the rheological properties of granular materials. Their results show that with the increase of gravity, the granular flow velocity, shear rate and velocity fluctuation all increase. Additionally, they showed that with the increase of inclination angle, the change of gravity environment significantly affects the rheological state of granular materials.

To our knowledge, only a few studies have explored the effect of gravity levels on granular column collapses, especially concerning deposit morphology. Therefore, the study aims to analyse the impact of varying gravity levels on the deposit behaviour of gravity-driven particle columns. After validating our model against existing experimental studies, we conduct a comprehensive analysis of the scaling relationship between gravity levels and collapse responses. By comparing our simulations results with natural landslides in the Solar System, ranging from laboratory to large-scale scenarios, we establish a regression line that supports our conclusions.

2.5. Particle shape

Qualitative and quantitative terminologies, such as symmetry, sphericity, convexity, regularity, elongation, and flatness, are commonly used to describe particle shapes. Naturally occurring particles tend to display arbitrary shapes, including concave and irregular forms. In contrast, engineered granular materials often favour regular shapes that are easier to describe, manipulate, and manufacture. Three common methods for reconstructing the shapes of real particles in numerical modelling of granular particles were summarized (Zhao et al., 2023), as illustrated in Figure 2.2. These methods include particle-based approaches, such as the sphere-clump or sphere-

cluster methods in DEM, mesh-based approaches, such as triangular meshes methods, and analytical-surface approaches, including spherical harmonics (SH) methods, which are widely used to reconstruct the real particles.

To understand the collapse behaviour of granular flow, fundamental studies of the deposit morphology were conducted by Lube et al. (2004) and Lajeunesse et al. (2004). They filled cylindrical column with granular materials and allowed them to spread on the horizontal surface under gravity. Their results revealed that collapse characteristic (e.g., flow pattern, run-out distance, and final height) is governed by initial aspect ratio. Notably, Lube et al. (2004) conducted the first column collapse study involving irregular particle shapes, such as sand, rice, salt, and couscous. Their findings indicated that particle shape had minimal influence on flow patterns, deposit morphology, or scaling law constants. However, the variation in particle shape was accompanied by changes in other material parameters, such as particle volume, making it difficult to isolate the effects of particle shape alone.

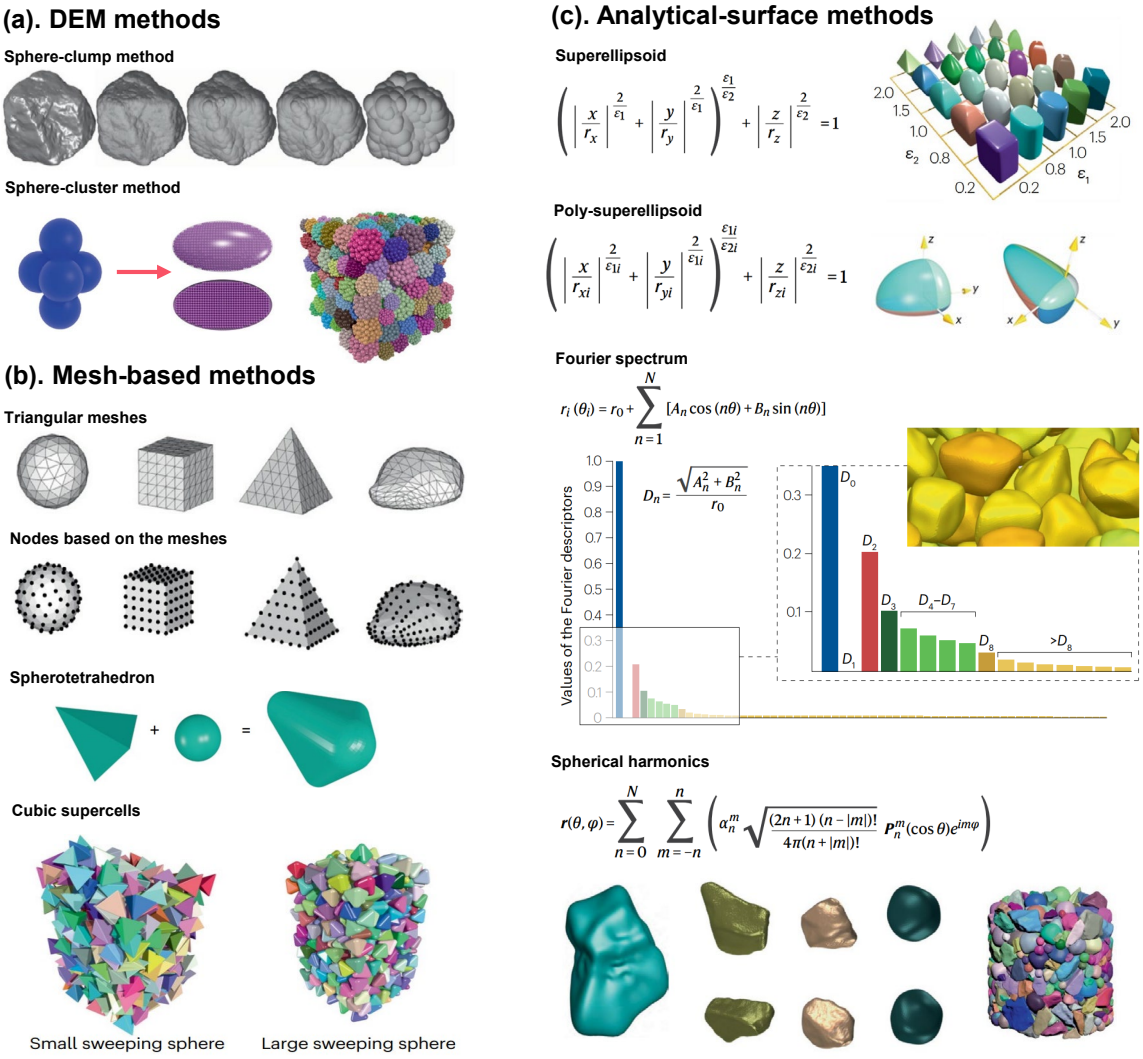

Figure 2.2 Numerical methods on particle shape representation. (a) DEM clumped methods. (b) Mesh-based methods. (c) Analytical-surface methods. For definition of variables, see the corresponding references. (picture represented from (Zhao et al., 2023)).

Lube et al. (2004) conducted a seminal column collapse study involving irregular particle shapes, such as sand, rice, salt, and couscous. Their findings indicated that particle shape had minimal influence on flow patterns, deposit morphology, or scaling law constants. In their experiments, the variation in particle shapes was accompanied by the changes of material properties, making it difficult to isolate the effects of particle shape alone. Numerical simulations provide several advantages compared to experimental methods for investigating the effects of particle shape, particularly in isolating specific parameters for individual examination. Most studies have relied on Discrete Element Method (DEM) where methods such as setting rolling resistance for spherical particles, sphere-clump or sphere-cluster approaches are commonly used to simulate irregularly shaped particles.

First, focusing on final deposit responses, Staron and Hinch (2005), using 2D DEM simulations of granular collapse, showed that perfectly spherical particles produced a larger run-out distance and a smaller final height compared to more realistic particle shapes. Cleary and Frank (2006a) demonstrated that particle shape is a limiting factor in reproducing experimental results and were convinced that particle shape can have a significant impact on the flow and final deposit shape. Conversely, Tapia-McClung and Zenit (2012) employed the multi-sphere approach to model the collapse of elongated particles and concluded that particle elongation did not affect the deposit run-out distance or deposit height, being consistent with the findings of Lube et al. (2005). Achieving similar conclusions, Trepanier and Franklin (2010) reported similarities between the collapse responses of these rod-like particles and spherical ones. However, their study was limited to one particle shape, ellipses, but for a wide aspect ratios range from 2.6 to 47.5. Albaba et al. (2015) developed a numerical model to assess the impact of dry granular flow on a rigid wall using clumped particles, calibrated with experimental data from dry gravel flow. Their results showed that clumped particles reduced rotational velocity by up to 70% compared to spherical particles. Kermani et al. (2015) used a rotational resistance factor to reduce particle rotation of uniform spherical particles to represent non-spherical particles, and observed that higher rotational resistance leads to higher final deposit height and shorter run-out distance. This indicated a particle shape effect. Likewise, Owen et al. (2009) used superquadric DEM with particles of varying aspect ratios and blockiness in planar columns, finding that increased blockiness significantly enhanced material strength, leading to a larger angle of repose, shorter bed length, and increased bed height. Supporting these results, Hoang and Nguyen (2023) also used superquadric DEM to examine the effects of blockiness and particle aspect ratio on granular column collapse. They also found an effect on deposit geometry and scaling law constants where elongated and platy particles caused uneven deposit surfaces, but their effects on deposit geometry and scaling laws varied between the two shapes. Torres-Serra et al. (2021) confirmed these results using elongated spheroids, observing an increase in deposit height and a decrease in run-out distance compared to spherical particles. Dong (2023) conducted a series of DEM simulations to study run-out distance and deposition in granular flows. His results revealed that particle shape significantly impacts granular mobility, ranking it in terms of granular mobility from highest to lowest as sphere-like particles, pyramid-like particles, slab-like particles, cube-like particles, and rod-like particles. Dong further proposed

that particle shape primarily affects granular mobility through its influence on energy dissipation via tangential collisions and rolling friction.

Besides, non-spherical particles also affect the energy conversion during the granular collapse according to various actors. Tapia-McClung and Zenit (2012) observed a reduction in the rates of change and maximum normalised kinetic energy during the collapse of elongated particles. They also suggested that the final normalized potential energy is independent of particle length. Kermani et al. (2015) reported a decrease in normalised dissipated energy with increased rotational resistance between particles, implying that non-spherical particles dissipate less energy, which is not universally correct. Zou et al. (2022) compared the fraction of sliding contacts, referred to as sliding fraction, between spheres and elongated spheroids. They found that the sliding fraction of elongated spheroids was higher than that of spheres, suggesting a transition from rolling-dominated to sliding-dominated as shape deviates from spheres. This potentially leads to more dissipated energy due to the increase in frictional effect in sliding, contrary to the findings of Kermani et al. (2015).

In summary, previous studies have primarily focused on convex shapes, such as spheres, elongated spheroids, and platy particles, while naturally occurring particles exhibit arbitrary shapes with both concave and convex features. Quantitative research on irregularly concave shaped particles is still limited. In this work, to address this, we conducted a systematic and comprehensive investigation into the effects of a wide range of particle shapes on granular flow responses. Spherical Harmonic (SH) functions were used to reconstruct and test realistic particles with specific shape parameters. A DEM model is then validated against these tests and extract new features to understand the influence of particle shape on collapse behaviour.

2.6. Other factors

Many researchers have examined the effect of Particle Size Distributions (PSD) on collapse behaviour. Lai et al. (2017) investigated the effect of fractal PSD on the mobility of dry granular flows, both numerically and experimentally, through the collapse of granular columns. Their findings indicated that, given the same initial configuration (e.g., height, width, and porosity), a granular column with a higher fractal dimension exhibits greater flow mobility due to the "lubricant effect" of an increasing number of fine particles. However, Cabrera and Estrada (2021) challenged this, arguing that flow mobility in Lai et al. (2017) is independent of the PSD effects, as long as the system-to-grain size ratio of the studied system is sufficiently large. This was further supported by the constant steady-state shear strength across granular assemblies with varying fractal dimensions, regardless of the inertia number.

Polanía et al. (2022) extended these studies to an immersed condition, finding that particle size polydispersity significantly influences on the mobility of granular flows. Similarly, Linero et al. (2017) presented that elongation and flatness of colluvial grains weathered from anisotropic sedimentary rocks decreased and increased, respectively, with particle size, while the roundness seemed was not correlated with particle size. Inspired by their results, Nie et al. (2024) explored

the role of fines in the mobility of dry granular flows, considering the actual particle size-shape correlation. This study revealed that the presence of fines either enhances or has little effect on flow mobility, depending on the actual particle size-shape correlation.

In addition to PSD, numerous studies have explored other factors influencing granular flow behaviour. For example, research has focus on the effects on erodible surfaces (Crosta et al., 2009, Mangeney et al., 2010), collapse in water or cohesive materials (Thompson and Huppert, 2007, Jing et al., 2018a, Zhu et al., 2022), and the influence of grain size (R_0/d, where R_0 is the system dimension, d is the particle diameter) (Cabrera and Estrada, 2019, Man et al., 2021b).

3 Effect of Basal Friction on Granular Column Collapse

The collapse behaviour of granular materials is influenced by many factors, such as aspect ratio and inter-particle friction. However, the specific impact of basal to grain friction on column collapse remains poorly understood. In this study, we systematically analyse the effect of basal friction on gravity-driven granular column collapse using a validated smoothed particle hydrodynamics (SPH) model. The results show that such the basal friction coefficient does influence deposit geometry, deposit morphology, and energy conversion. To predict the run-out distance, we propose a modified formula that incorporates the basal friction coefficient, considering two extreme cases, i.e., $\mu = 0$ and $+\infty$. The basal friction also exerts an influence on the final height, with higher friction coefficients resulting in greater final heights. As the friction coefficient increases, the aspect ratio corresponding to the maximum final height also increase. However, we observe a convergence of the effect of basal friction on the final height when $\mu > 0.5$. Furthermore, the competition mechanism between the initial column aspect ratio and basal friction coefficient reveals two transition zones between the three main deposit regimes (regime I, regime II, and regime III). This suggests that the deposit regime can be influenced by basal friction. Additionally, an analysis of energy conversion supports many of the conclusions provided in the text and exhibits the interplay between pressure gradient and base friction. Our findings show the clear influence of basal friction on the collapse behaviour of granular materials and therefore should be carefully considered in future studies.

This Chapter was published in the following paper:

Yucheng Li*, Deheng Wei, Ningning Zhang, Raul Fuentes (2024). Effect of basal friction on granular column collapse. Granular matter. 26-62.

3.1. Mohr-Coulomb elastic-plastic model

The Mohr-Coulomb elastic-plastic model was used because it matches the experimental results of Lube et al. (2004) and numerical results of Man et al. (2021a). Additionally, Yang et al. (2020) showed that all, Mohr-Coulomb, $\mu(I)$ and *DP* models provided similar matches to the experimental results of Lube et al. (2004). They also showed that $\mu(I)$ model underestimates the final height, while the *DP* model overestimates the final height. Therefore, we believe that the simpler Mohr-Coulomb model was appropriate for the purpose of this study. The equations are presented using the Einstein convention, where α, β, and γ denote the Cartesian coordinates.

The Mohr-Coulomb yield surface and its plastic potential function are expressed as follows, respectively:

$$f = \sin\varphi I_1 + \frac{1}{2}\left[3(1-\sin\varphi)\sin\theta + \sqrt{3}(3+\sin\varphi)\cos\theta\right]\sqrt{J_2} - 3c\cos\varphi = 0, \tag{3.1}$$

$$g = \sin\psi I_1 + \frac{1}{2}\left[3(1-\sin\psi)\sin\theta + \sqrt{3}(3+\sin\psi)\cos\theta\right]\sqrt{J_2} - 3c\cos\psi, \tag{3.2}$$

where φ and ψ are the soil internal friction and dilatant angles, respectively; I_1, J_2, and J_2 are the first principal, second, and third deviatoric stress invariants, respectively; c is cohesion; and θ is the Lode angle, $\theta = \frac{1}{3}\cos^{-1}(1.5\sqrt{3}\frac{J_3}{J_2^{1.5}})$.

Substituting the yield function and plastic potential function into the generalized form of the elastic-perfectly plastic model shown in Appendix. A.

The Jaumann stress tensor is adopted to allow modelling for large deformation. Hence, the final form of the stress-strain relation for Mohr-Coulomb elastic-perfectly plastic constitutive model can be expressed by:

$$\dot{\sigma}^{\alpha\beta} = \sigma^{\alpha\gamma}\dot{\omega}^{\beta\gamma} + \sigma^{\gamma\beta}\dot{\omega}^{\alpha\gamma} + 2G\dot{e}^{\alpha\beta} + K\dot{\varepsilon}^{\gamma\gamma}\delta^{\alpha\beta} - \dot{\lambda}\left[3K\sin\varphi\,\delta^{\alpha\beta} + 2G\left(\frac{\partial g}{\partial J_2}s^{\alpha\beta} + \frac{\partial g}{\partial J_3}t^{\alpha\beta}\right)\right], \tag{3.3}$$

where $\dot{\varepsilon}^{\alpha\beta}$ and $\dot{\omega}^{\alpha\beta}$ are the strain and spin rate tensors, which can be related to the gradient of the velocity as follows:

$$\dot{\varepsilon}^{\alpha\beta} = \frac{1}{2}\left(\frac{\partial v^{\alpha}}{\partial x^{\beta}} + \frac{\partial v^{\beta}}{\partial x^{\alpha}}\right), \tag{3.4}$$

$$\dot{\omega}^{\alpha\beta} = \frac{1}{2}\left(\frac{\partial v^{\alpha}}{\partial x^{\beta}} - \frac{\partial v^{\beta}}{\partial x^{\alpha}}\right). \tag{3.5}$$

3.2. SPH method

SPH has been broadly demonstrated for the modelling of large deformation granular materials, including granular column collapse (Chen and Qiu, 2012, Szewc, 2017, Fávero and Borja, 2018, Kermani and Qiu, 2018b, Yang et al., 2020, Bui and Nguyen, 2021). We use the SPH solver in LS-DYNA (Hallquist, 2006), that uses an explicit code developed for the dynamic analysis of non-linear problems and has the advantage of widely available material models suitable for granular materials. In SPH the governing equations for the bulk are discretised over a set of particles, each representing a certain volume and therefore with a certain mass obtained from the initial density of the material they represent. Each particle is used to calculate the different variables, such as velocity and stresses (forces) where the continuum is approximated by a summation of quantities for each particle, as shown in Figure 3.1. For this, a kernel function $W(\boldsymbol{x}, h)$ is used, where h is the smoothing length. The kernel approximations are used to compute forces from the spatial derivatives of stresses. The spatial derivatives of velocity are used to calculate strain rates using the Jaunmann stress approach, as already mentioned.

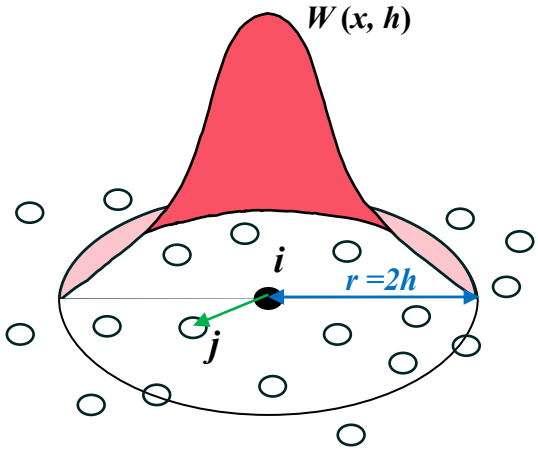

Figure 3.1 Particle approximations within the influence domain of the smoothing function W (x, h) for particle i.

Hence, a variable (e.g., velocity or stress) can be approximated everywhere using the function,

$$\langle f(x)\rangle = \int_{\Omega} f(x')W(x-x',h)dx'. \tag{3.6}$$

The discrete form of Equation (1) can be written as,

$$\langle \nabla \cdot f(x)\rangle = \int_{\Omega} [\nabla \cdot f(x')]W(x-x',h)dx', \tag{3.7}$$

where Ω is the interpolation region, f is a function of the location vector $\boldsymbol{x}$ of the particle, and d$\boldsymbol{x}$ is a volume. The kernel function $W(x, h)$ is defined using the function θ though the relation,

$$W(x,h) = \frac{1}{h(\boldsymbol{x})^d}\theta(q), \tag{3.8}$$

where d is the number of space dimensions, and q is the relative distance, $q = |x - x'|/h$. Here, $\theta(q)$ is the most commonly function cubic B-spline function and defined as,

$$\theta(q) = C\begin{cases} 1 - \frac{3}{2}q^2 + \frac{3}{4}q^3, & 0 \le q \le 1 \\ \frac{1}{4}(2-q)^3, & 1 \le q \le 2 \\ 0, & otherwise \end{cases}, \tag{3.9}$$

where C is a constant of normalization that depends on the number of the space dimensions.

By converting integral representations (as given in Equations (3.6) and (3.7)) into a particle approximation form, the equations take on a more practical and computationally manageable representation in the SPH framework:

$$\langle f(x_i)\rangle = \sum_{j=1}^{N} \frac{m_j}{\rho_j} f(x_j) W(x_i - x_j, h), \tag{3.10}$$

$$\langle \nabla \cdot f(x_i)\rangle = \sum_{j=1}^{N} \frac{m_j}{\rho_j} f(x_j) \nabla \cdot W(x_i - x_j, h), \tag{3.11}$$

where m_j is the mass of particle j, ρ_j is the density of particle j.

The general governing equations of mass and momentum conservation can be applied to granular material collapse as follows:

$$\frac{D\rho}{Dt} = -\rho \frac{\partial v^\alpha}{\partial x^\alpha}, \tag{3.12}$$

$$\frac{Dv^\alpha}{Dt} = \frac{1}{\rho}\frac{\partial \sigma^{\alpha\beta}}{\partial x^\beta} + b^\alpha, \tag{3.13}$$

where ρ is the material density; v^α is the velocity component; $\sigma^{\alpha\beta}$ is the stress tensor component; b^α is the acceleration due to the external forces.

The SPH approximation of governing equations can be derived using Equations (3.12) and (3.13). Writing partial differential governing equations in a discrete form. The mass conservation and momentum conservation in the framework of standard SPH becomes,

$$\frac{D\rho_i}{Dt} = \sum_{j=1}^{N} m_j \left(v_i^\alpha - v_j^\alpha\right) \frac{\partial W_{ij}}{\partial x_i^\alpha}, \tag{3.14}$$

$$\frac{Dv_i^\alpha}{Dt} = \frac{1}{\rho_i}\sum_{j=1}^{N} \frac{m_j}{\rho_j}\left(\sigma_i^{\alpha\beta} + \sigma_j^{\alpha\beta}\right) \frac{\partial W_{ij}}{\partial x_i^\beta} + b_i^\alpha, \tag{3.15}$$

where b_i^α is the force per unit mass due to gravitation.

To stabilize the simulation and improve its accuracy, the artificial viscosity is imported into Equation (3.15), obtaining the final form of Equation (3.16). Artificial viscosity is shown in Appendix. B.

$$\frac{Dv_i^\alpha}{Dt} = \sum_{j=1}^{N} m_j \left(\frac{\sigma_i^{\alpha\beta} + \sigma_j^{\alpha\beta}}{\rho_i \rho_j} + \Pi_{ij} \delta^{\alpha\beta} \right) \frac{\partial W_{ij}}{\partial x_i^\beta} + b_i^\alpha . \quad (3.16)$$

Combined with the constitutive equation introduced in the Sec 3.1, the above system of governing equations can be solved. The calculation steps in LS-DYNA are shown in Figure 3.2.

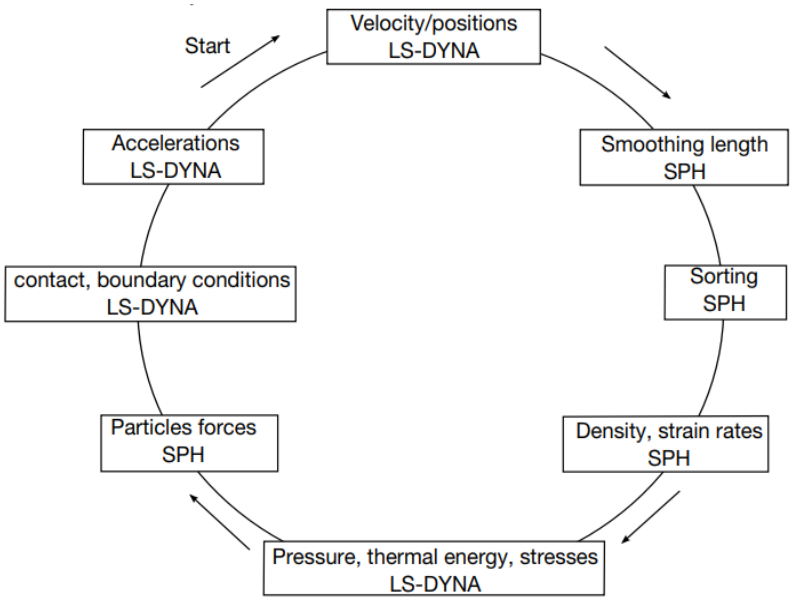

Figure 3.2 The calculation cycle for SPH methodology in LS-DYNA.

3.3. SPH model set-up

A sketch of granular column collapse is shown in Figure 3.3(a), where a cylindrical domain discretised by SPH particle is placed over a rigid horizontal surface. The friction force (F_s) between the rigid plane and SPH particles is limited by the friction coefficient, μ, in the dry Coulomb friction model: $F_s = \mu F_N$, where F_N is the normal contact force. μ was initially set to 0.4 in accordance with the validation experiments of Ref. (Lube et al., 2004). Several relevant papers utilizing SPH simulations have validated the experimental results of Ref. (Lube et al., 2004), with their respective material parameters summarized in Table 3-1.

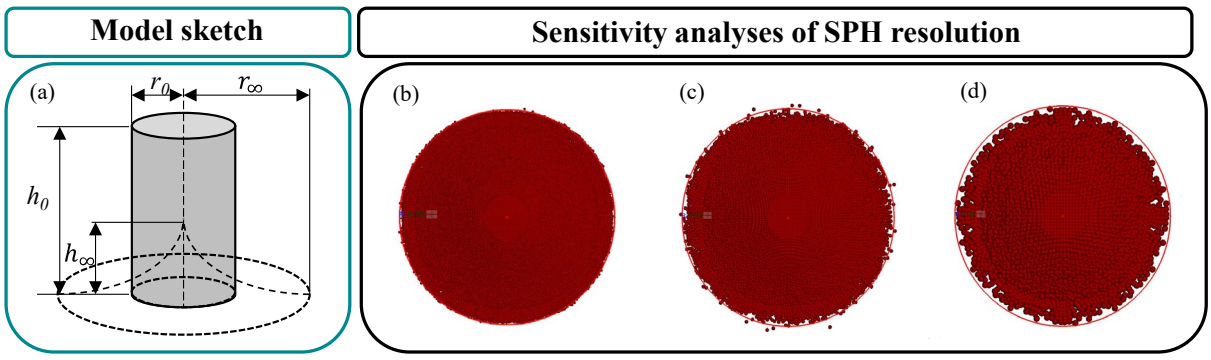

Figure 3.3 (a) A sketch of the axisymmetric granular collapse: shaded region denotes the initial column (r_0: initial radius, h_0: initial height), dashed curve denotes deposit geometry (r_∞: final run-out distance, h_∞: final height). (b) Particle spacing: Δp = 2.0mm, a = 0.55. (c) Δp = 3.0mm, a = 0.55. (d) Δp = 5.0mm, a = 0.55.

Prior to conducting the simulation, we performed a sensitivity analysis to determine the optimal number of particles that can balance computational cost and accuracy. Figure 3.3(b), (c), and (d) illustrate three final deposit patterns with different particle spacings, Δp (the distance between adjacent particles in the global coordinate of 2.0, 3.0 and 5.0mm), with corresponding SPH particle numbers of 220,080, 63,378, and 13,904, respectively. A red circle with a radius of 0.176m was used as a standard reference size for better comparisons. We observed similar results for Δp of 2.0 and 3.0mm, while the boundary was discontinuous for Δp = 5.0mm due to the insufficient number of particles. Hence, Δp = 3.0mm was chosen for all simulations in this study.

Table 3-1 Material parameters used in previous studies.

Database	*Setup*	*ρ/kg.m^{-3}* *Density*	*a/-* *Aspect ratio*	*φ/°* *Angle of friction*	*υ/-* *Poisson's ratio*	*E* /MPa *Young's modulus*
Lube et al. (2004)	Expt. axisymmetric	2600	0.19-13.8	-	-	-
Chen and Qiu (2012)	Num. axisymmetric	2600	0.225-20	30	0.3	6
Szewc (2017)	Num. axisymmetric	2600	0.25-9.5	30	-	-
Fávero and Borja (2018)	Num. axisymmetric	2600	0.5-4.0	33/37	0.3	20.16
Kermani and Qiu (2018a)	Num. axisymmetric	1570	0.5-11	28	0.3	12
Peng et al. (2019)	Num. axisymmetric	2600	0.5	37	-	-
Yang et al. (2020)	Num. axisymmetric	2600	0.2-30	30	0.3	5.98
This study	Num. axisymmetric	2600	0.4-25	37	0.3	6.00

As summarized in Table 3-2, 18 cases with different granular column aspect ratios covering a wide range from 0.4 to 25 were simulated. Note that in the models only the column height was changed, while the column radius (r_0 = 0.1m) remained constant.

Table 3-2 Test series of granular column collapse

Case ID	$a = h_0/r_0$	h_0 /m	No. of particles
1	0.4	0.04	49,294
2	0.55	0.055	63,378
3	0.7	0.07	84,504
4	0.8	0.08	95,067
5	0.9	0.09	105,630

6	1.0	0.10	119,714
7	1.5	0.15	176,050
8	2.75	0.275	323,932
9	4	0.4	471,814
10	6	0.6	704,200
11	8	0.8	940,107
12	9	0.9	1,056,300
13	10	1.0	1,176,014
14	12	1.2	1,408,400
15	13.8	1.38	1,619,660
16	15	1.5	1,760,500
17	18	1.8	2,112,600
18	25	2.5	2,932,993

3.4. Initial validation

To validate whether our SPH can capture the rheological behaviour of granular columns, these results focus on flow patterns, while run-out distances that also serve as validation will be illustrated in Section. 3.5. Figure 3.4 compares evolutions of numerical flow patterns with experimental patterns of three typical aspect ratios from Lube et al. (2004). The three aspect ratio values induce three clearly different flow patterns and final deposition characteristics. For small aspect ratios (e.g., a = 0.55), the collapse starts from the perimeter and spreads to the interior of the model, maintaining the initial height during the process. After collapse, a flat surface remains at the top of the model. For intermediate aspect ratios (e.g., a = 2.75), the model cannot maintain its initial height during the collapse, and the top surface changes from a flat plate to a conical tip. For large aspect ratios (e.g., a = 13.8), the top surface of the model maintains a flat shape during the collapse until the upper particles reach the static area at the bottom, after which it begins to collapse around the static area, resulting in a transition from a plane to revealing the tip (cusp) of the conical static area. During this process, the sand forms an outward propagating wave that transfers mass from the centre to the edge of the diffusion, forming a concentric wave at the final deposit. Our numerical flow patterns agree well with their experimental results.

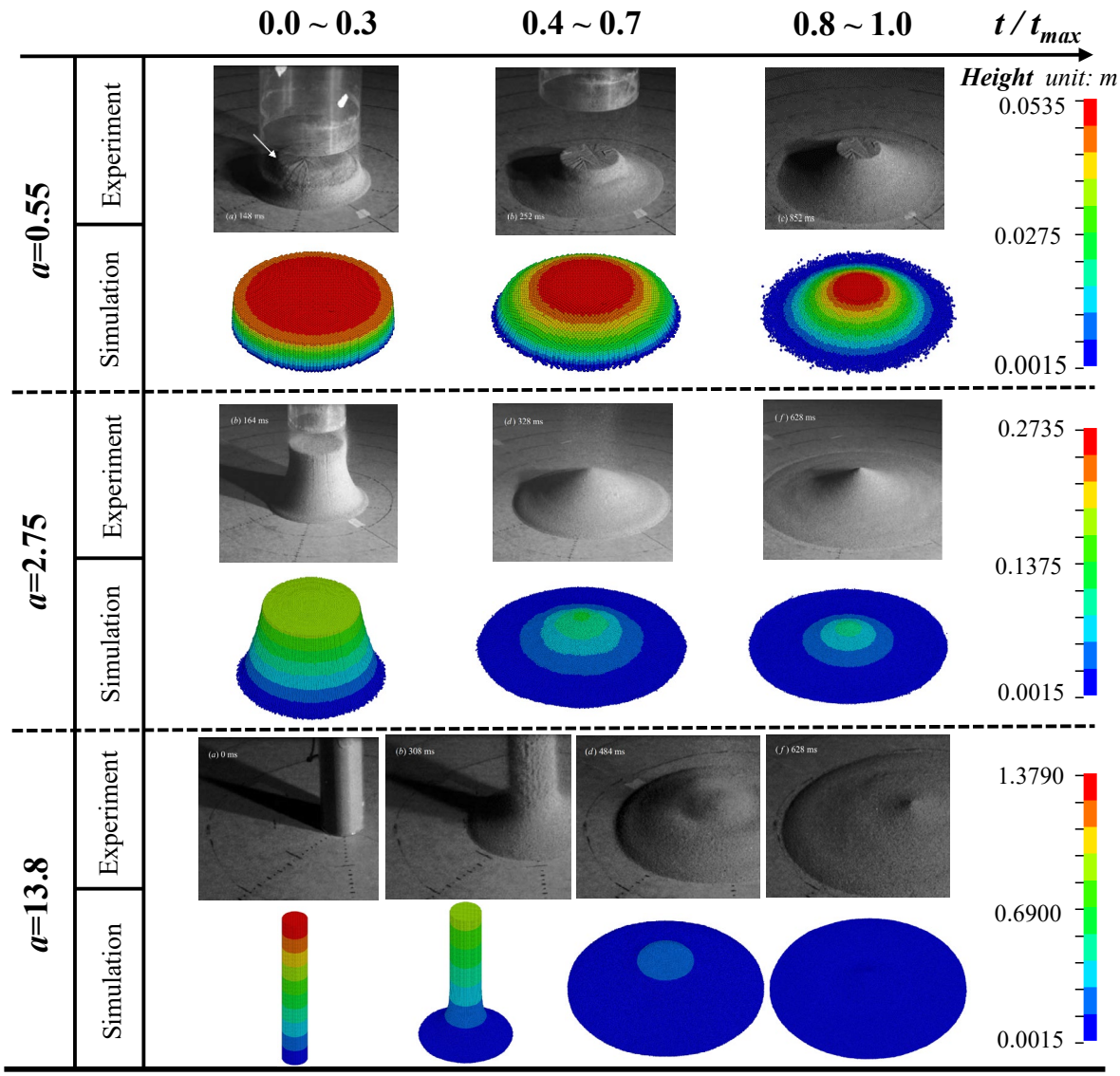

Figure 3.4 Granular column collapse evolution at various time points observed in three columns with representative aspect ratios (coloured images with colour bar) and final experimental collapse patterns reported in Lube et al. (2004) (grey images).

3.5. Results and discussion

Values of the basal friction coefficient (μ) from 0.1 to 1.8 were used to investigate its influences on the deposit results of sand column collapse, including run-out distance, final height, morphology, and energy conversion analysis. While classical physics typically deals with friction coefficients between 0 and 1.0, a basal friction coefficient larger than 1.0 implies a situation where the force required to overcome the resistance to motion at the base is greater than the force pushing the material downwards due to gravity. This may happen in extreme cases such as very textured or rough surfaces or cohesive forces.

3.5.1. Run-out distance

We determine the run-out distance of the granular column using the 'effective' run-out distance method proposed by Yang et al. (2020). Figure 3.5 shows a comparison of the normalized run-out distance between simulations and experiments. For μ = 0.4, cited by Lube et al. (2004), the numerical results shows a good agreement with the experimental data, but also are consistent with the other types of simulations (Szewc, 2017, Fávero and Borja, 2018). Reported experimental and numerical simulations have indicated a bilinear relationship between the initial column aspect ratio and the normalized run-out distance (see Equations (2.1) and (2.2) and Table 3-3). This critical aspect ratio of 1.7 can be explained from a physical and mathematical point of view. Mathematically, calculating the transition point as the intersection of both sides of Equation (3.23) results in different values for each friction. However, the average value is 1.7 which agrees with Lube et al. (2004) and also provides reasonable match to all the experimental results. Physically, when $a < 1.7$, the collapse is dominated by friction, and when $a > 1.7$, the dominating factor is the pressure gradient. Hence, it is a transition from first to second order that has also been shown by the experimental results of Lube et al. (2004). Figure 3.6 clearly present the deposit geometry of the particle column is governed by a combination of aspect ratio, and basal friction.

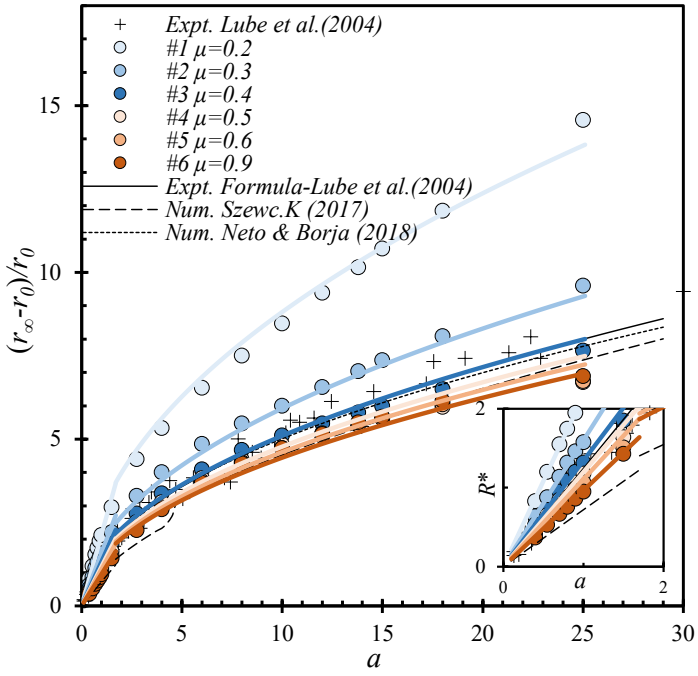

Figure 3.5 Comparison of the normalized run-out distance between different simulations and experiments. Coloured lines fitted according to Equation (3.23).

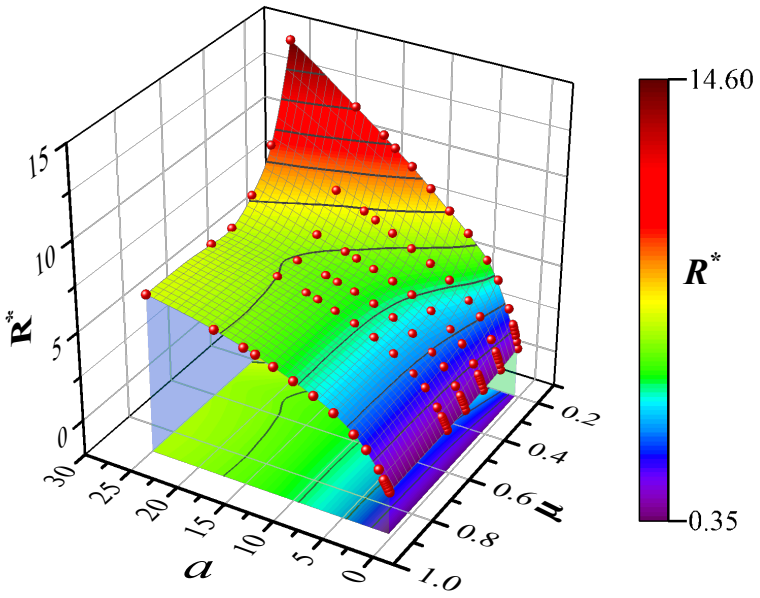

Figure 3.6 Three-dimensional (3D) plot of the normalized run-out distance R^* versus aspect ratio a and friction coefficient μ.

Table 3-3 Proposed formula for predicting the deposit run-out distance.

Database	Formula form
Expt. axisymmetric: Lube et al. (2004)	$R^* = \frac{r_\infty - r_0}{r_0} \simeq \begin{cases} 1.24a, & a < 1.7 \\ 1.6a^{1/2}, & a \geq 1.7 \end{cases}$
Num. axisymmetric: Szewc (2017)	$R^* \simeq \begin{cases} 0.72a, & a < 1.7 \\ 1.02a^{3/5}, & a \geq 1.7 \end{cases}$
Num. axisymmetric: Fávero and Borja (2018)	$R^* \simeq \begin{cases} 1.11a, & 0 \leq a < 1.7 \\ 1.66a^{0.48}, & a \geq 1.7 \end{cases}$

3.5.1.1. For lower aspect ratio models

The inset of Figure 3.5 shows that R^* varies linearly with the aspect ratios when $a < 1.7$. Hence, we propose the introduction of μ to R^* by writing

$$R^* = f(\mu) \cdot a^{\beta 1}, \tag{3.17}$$

where $f(\mu)$ is an unknown function. To achieve plausible forms of f over the whole range of a, we must make sure that for $\mu = 0$, the collapsed grains would never stop and thus $R^* \to \infty$. Following the same logic, when $\mu \to \infty$, every grain would become quiescent at all times as soon as it touches the substrate, under which the column can be deemed collapsed onto one layer of its composed grains. With these two asymptotic values of $f(\mu)$ in mind, we assume that

$$f(\mu) = \frac{O}{\mu^P} + Q, \tag{3.18}$$

where O, P, and Q are fitted parameters and are all positive.

This form of f, satisfies that for increases of μ, the difference between slope between R^* and a gradually vanishes (see Figure 3.7(a)). When μ approaches to zero, the particles are not limited in the horizontal surface, and when μ is infinity, the bottom layer particles are fixed to the substrate, and other particles slide on the bottom layer particles. The fitting curve to the numerical simulations in Figure 3.7(b) gives values of "$O = 0.1834$, $P = 1.268$, $Q = 0.7536$" with a high R^2 value (see Table 3-4). The fact that $f(\mu)$ approaches to 0.7536 when $\mu \to \infty$, means that the minimum run-out distance for a given μ increases linearly as the aspect ratio increases, with a slope of 0.7536. Somewhat surprisingly, this value is equal to the tangent value of the internal friction angle (tan 37° = 0.7536) of the material. This would indicate that the minimum run-out distance depends on the material internal friction angle. Using the fitted values, the proposed formula is:

$$R^* = \left(\frac{0.1834}{\mu^{1.268}} + 0.7536\right) \cdot a \tag{3.19}$$

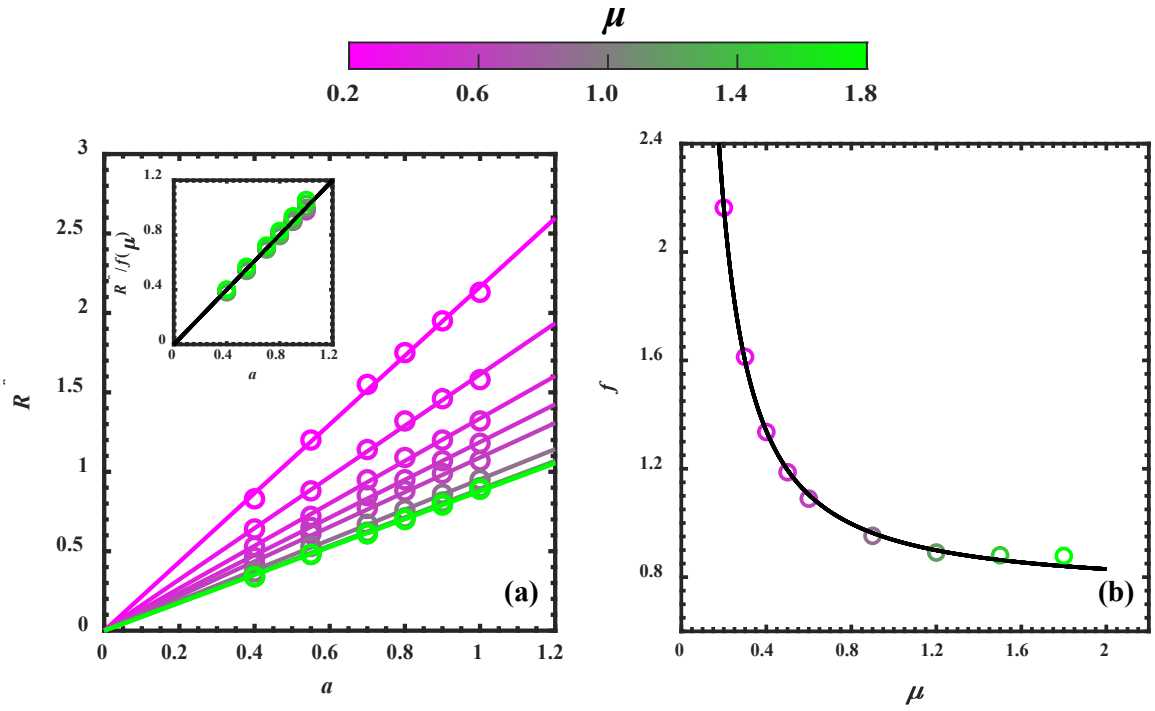

Figure 3.7 (a) Evolution of normalised run-out distance R^* with low aspect ratios and the fitting results. (b) Fitting results of $f - \mu$.

Table 3-4 Fitting results for low aspect ratios.

μ	f	R^2
0.2	2.163703	0.996497
0.3	1.612932	0.996517
0.4	1.335783	0.997382
0.5	1.187215	0.998206
0.6	1.08964	0.99676
0.9	0.952388	0.999187
1.2	0.890816	0.997525
1.5	0.880822	0.998204
1.8	0.8781778	0.998513

3.5.1.2. For higher aspect ratio models

When $a \geqslant 1.7$, the relation between μ and R^* is assumed as an exponential function such as:

$$R^* = \alpha(\mu) \cdot a^{\beta 2} \tag{3.20}$$

where $\alpha(\mu)$ is an unknown function. By fitting our simulation results, we obtain a constant value of $\beta 2$ equal to 0.49 in Table 3-5. For the function of $\alpha(\mu)$, we use the same approach as for $f(\mu)$

$$\alpha(\mu) = \frac{A}{\mu^B} + C \tag{3.21}$$

where A, B, and C are fitted parameters and are all positive. The fitting results are presented in Figure 3.8(b), with the corresponding parameter values of $A = 0.023$, $B = 2.572$, $C = 1.408$, and $R^2 = 0.993$. The linearity of each point, as indicated by the slope ratio of 0.49, is verified by the inset plot of Figure 3.8(a) that we plot in logarithmic scale. The same explanation provided for low aspect ratios in term of the influence of μ applies here. Finally, conversely to low aspect ratios, when $\mu \to \infty$, the final run-out distance depends on aspect ratio and $R^* = 1.408a^{0.49}$. The final formula for higher aspect ratios is:

$$R^* = \left(\frac{0.023}{\mu^{2.572}} + 1.408\right) \cdot a^{0.49} \tag{3.22}$$

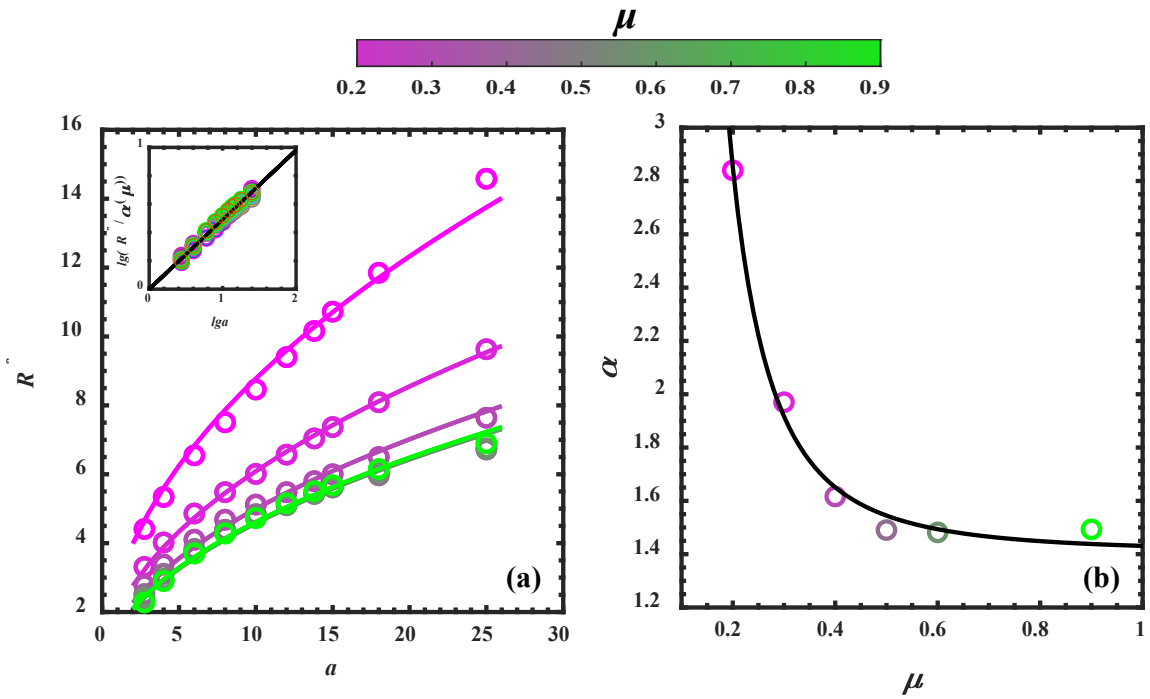

Figure 3.8 (a) Evolution of normalised run-out distance with higher aspect ratios in different friction coefficients. (b) Fitting results for higher aspect ratio models.

Table 3-5 Fitting results for larger aspect ratios.

μ	α	$\beta 2$	R^2
0.2	2.840004	0.49	0.9861
0.3	1.969984	0.49	0.9978
0.4	1.616418	0.49	0.9883
0.5	1.490427	0.49	0.9666
0.6	1.481723	0.49	0.9822
0.9	1.493148	0.49	0.9888

Finally, the modified formulas for predicting the run-out distance, as summarized in Equation (3.23), are presented alongside the corresponding fitting curves in Figure 3.5. Compared with those in Table 3-3, we find that the frontier factors (f and α) are highly dependent on the basal friction coefficient, while the index parameters (β) are independent of it. For lower aspect ratios (a < 1.7), the R^* and the initial aspect ratio show a linear relationship and the index parameter is the same as that proposed by Lube et al. (2004); and for higher aspect ratio (a > 1.7), the R^* and the initial aspect ratio follows a power law and our result of 0.49 is very close to the result of Lube et al. (2004) of 0.5.

$$\frac{r_\infty - r_0}{r_0} = \begin{cases} \left(\frac{0.1834}{\mu^{1.268}} + 0.7536\right) \cdot a, & a < 1.7 \\ \left(\frac{0.023}{\mu^{2.572}} + 1.408\right) \cdot a^{0.49}, & a \geq 1.7 \end{cases} \tag{3.23}$$

3.5.2. Final height

The relationship between the rescaled final height, h_∞, and aspect ratio for various friction coefficients can be characterized by three distinct stages shown in Figure 3.9. Initially, there is a linear increase stage, followed by a power increase stage. Subsequently, a decrease stage occurs. We observed that the basal friction does not affect the linear increase stage (where the model maintains the initial height), but it becomes more relevant in the other stages. Particularly for larger values of a, the final height decreases as the aspect ratio increases. Our results ($\mu = 0.4$) are plotted in Figure 3.9 and compared to experimental and numerical results as well the proposed formula by Lube et al. (2004) shown in Equation (3.24) . Our simulations fit well with their experimental results as well as their proposed formula when $a < 10$. They did not provide a relationship for $a > 10$. Yang et al. (2020) carried out analysis for values of $a > 10$ using SPH method. Our results seem to fit the experimental results of Lube et al. (2004) better whilst confirming the trend as Yang et al. (2020). This allows us to propose a trilinear approximation proposed in Equation (3.25). Critically, our finding is in agreement with the results of Yang et al. (2020) and Roche et al. (2011). The reason is simply the transition from Regime II (conical shape) to Regime III (with a double threshold can be observed in Figure 3.11). Additionally, Figure 3.9 shows that this critical aspect ratio, after which the height reduces at increasing aspect ratios, increases with increasing base friction coefficient. It highlights again the important role of base friction.

$$\frac{h_\infty}{r_0} = \begin{cases} a, & 0 \leq a < 1.7 \\ 0.88a^{1/6}, & 1.7 \leq a < 10 \end{cases} \tag{3.24}$$

The extended forms in this study for axisymmetric granular column collapse with a wide range of aspect ratios are:

$$\frac{h_\infty}{r_0} = \begin{cases} a, & 0 \leq a < 0.86 \\ 0.88 \cdot a^{1/6}, & 0.86 \leq a < 10 \\ 1.853 \cdot a^{-0.189}, & a \geq 10 \ (Updated) \end{cases} \tag{3.25}$$

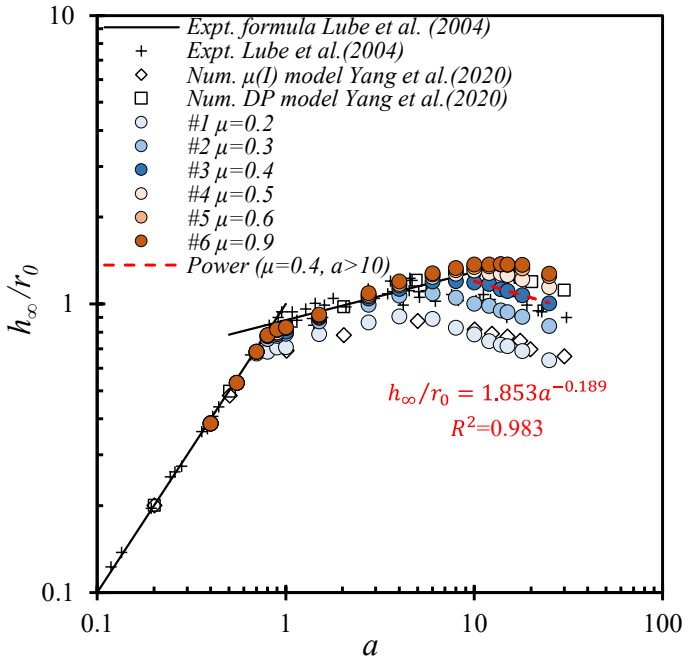

Figure 3.9 The relationship between rescaled final height and aspect ratio.

Figure 3.10 shows the contour map of 3D surface of rescaled final height (same way as illustrated in Figure 3.6) projected on a μ-a plane, closed method like. There are turning points in the contour area for the different colours, marked by the orthogonal points of the black arrow and contour lines, which represent the maximum rescaled final height point for each friction coefficient. It indicates that an increase in the friction coefficient affects the separation point (maximum final height) between the exponential increase stage and the decrease stage, resulting in an increase in the aspect ratio corresponding to the maximum final height. When $a < 2.5$, the effect of μ on the final height is negligible. Conversely, for cases where $a > 2.5$, the final height is influenced by μ. This is the reason why Lajeunesse et al. (2004) found that roughness only had influence on the final height of the larger aspect ratio models. It is worth noting that when the friction coefficient exceeds 0.5, there is a red trapezoidal zone (maximum h_∞/r_0 = 1.3-1.4 as shown in Figure 3.10), which is due to the redundancy of the friction at the substrate, where the effect of friction on the final height converges into a single value. This non-linear relationship between the friction coefficient and maximum height highlights the complexity of particle dynamics and the need for careful consideration of multiple factors when evaluating particle behaviour.

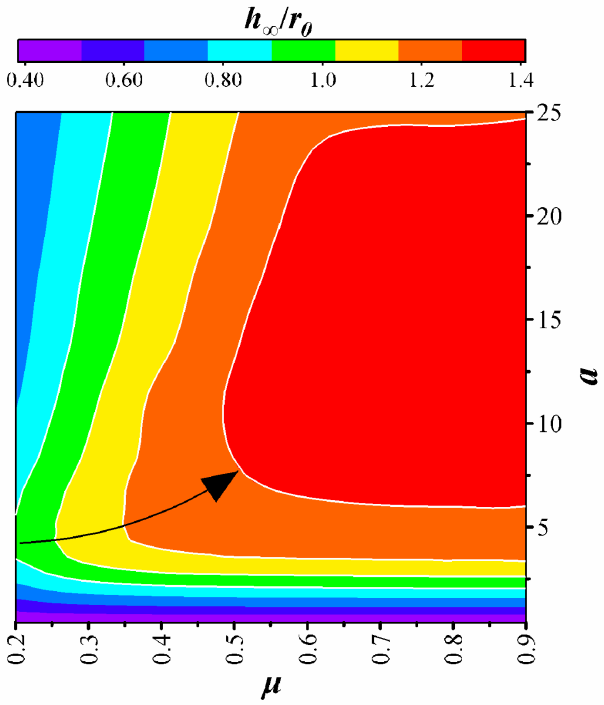

Figure 3.10 Contour map of rescaled final height projected on μ-a plane.

3.5.3. Deposit morphology

The granular columns collapse to form different morphology, primarily depending on the aspect ratio. The final deposit morphology is termed as 'deposit regime', not flow regime (Sheikh et al., 2021). Based on the literature, all final deposit morphologies can be classified by three regimes (Lube et al., 2004, Lajeunesse et al., 2004, Man et al., 2021a):

(1) Regime I: the granular materials spread through the avalanche on its flank and produces a circular undisturbed area at the upper surface of the column, forming a circular truncated cone, e.g., the flow pattern with $a = 0.55$ at $t/t_{max} = 0.8$-1.0 as shown in Figure 3.4;

(2) Regime II: the entire upper surface starts to flow immediately, forming a tip with a cone-like shape, e.g., the flow pattern with $a = 2.75$ at $t/t_{max} = 0.8$-1.0 as shown in Figure 3.4;

(3) Regime III: a concentric wave originates and propagates outwards, e.g., the flow pattern with $a = 13.8$ at $t/t_{max} = 0.8$-1.0 as shown in Figure 3.4. The final shape has been named differently by other researchers: 'Mexican hat' for $a > 3$ (Lajeunesse et al., 2004), liquid-like (Man et al., 2021a).

The regime identification process from the numerical models is illustrated in Appendix. C.

The results of deposit regime for all the models are shown in Figure 3.11, with each regime type represented by a different colour. The results show that the basal friction clearly influences the deposit regime. Two transition zones are revealed (indicated by dashed blue lines). Contrary to what was stated in previous studies, these depend on competition mechanism between the initial column aspect ratio and basal friction coefficient. The first transition (Zone 1 in the figure)

between regime I to regime II, occurs for when the friction coefficient varies from 0.1 to 0.2 and the aspect ratios between 0.5 and 0.8. Zone 2 (regime II to III) is defined by values of friction coefficient between 0.3 to 0.7 and aspect ratios from 8 to 25. Since Man et al. (2021a) does not consider the extreme conditions (zero and +∞) of the particle-boundary friction, their results only show one transition zone at $\mu > 0.1$.

These findings provide an explanation to the results reported by Lajeunesse et al. (2005), who showed that friction force dominates flow behaviour for small aspect ratios, without quantifying it fully. For models with medium aspect ratios ($0.7 < a < 6$), regime II is the sole regime observed, indicating that although basal friction continues to play a role, it is gradually replaced by pressure gradient effects. This is the reason why Frank (2006) found no influence of basal friction as they used $a = 1.91$. When the aspect ratio exceeds 6, a second transition zone emerges. Within this range, as the friction coefficient increases from 0.7 to 0.3 (as indicated by the direction of the black arrows), the deposit regime undergoes a transition from regime II to regime III. Finally, as the aspect ratio becomes sufficiently large, the influence of the friction coefficient decreases, and the pressure gradient effects become predominant and all morphologies correspond to regime III. These findings are consistent with those reported by Lajeunesse et al. (2005), who demonstrated that for large aspect ratios, flow behaviour is dominated by pressure gradient effects, not the basal friction coefficient.

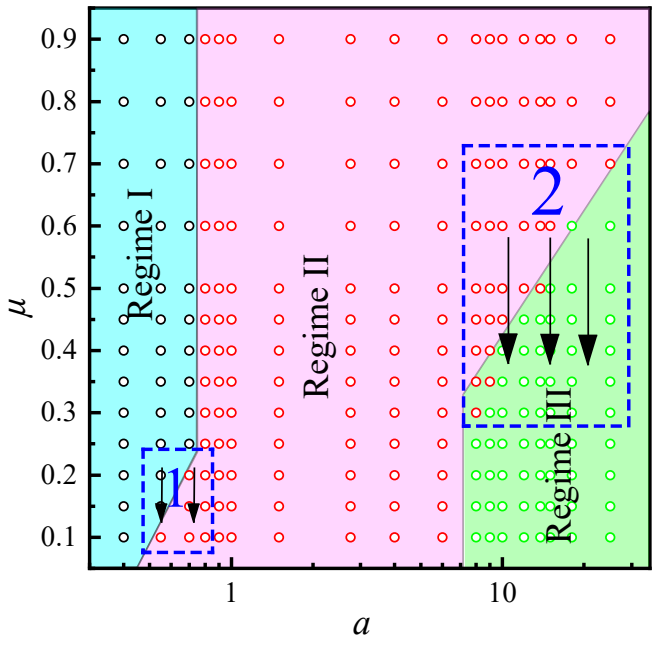

Figure 3.11 The results of deposit regimes vary with changes in basal friction coefficients and initial aspect ratios. Blue area: regime I, pink area: regime II, and blue area regime III; Two transition zones (blue dash zones 1 and 2); SPH results (black, red, and green circle points indicate regime I, regime II, and regime III, respectively).

3.5.4. Energy conversion analysis

For the gravity-driven dry granular flow, the total work of the system E_0 is the initial potential energy E_P. As the material flows, this energy is converted into kinetic energy E_K, basal dissipated energy E_D, and internal energy E_I. Basal dissipated energy is the change in kinetic energy of the SPH particles as a result of interaction with the basal surface, i.e., a proxy for base friction energy. The internal energy is the internal dissipated energy, including strain energy, internal heat energy, artificial viscosity energy, etc, i.e., proxy for internal friction of the material. The energy balance of the system at any given time is therefore,

$$E_0 = E_P + E_I + E_D + E_K. \tag{3.26}$$

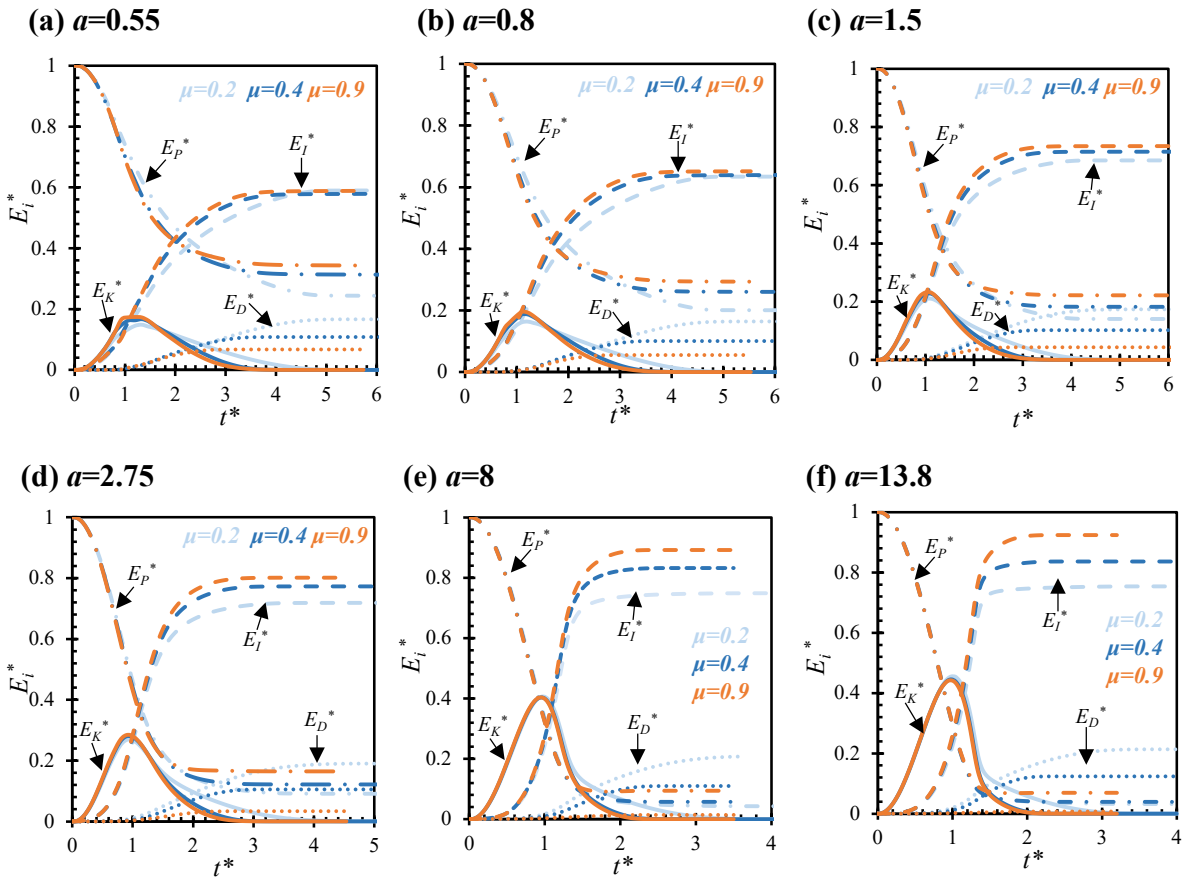

Figure 3.12 Influence of basal friction effect on the evolution of normalized energy with respect to normalized time under different aspect ratios. It provides insights for low columns with (a) a = 0.55, (b) a = 0.8, and (c) a = 1.5; medium columns with (d) a = 2.75 and (e) a = 8; and high column with (f) a = 13.8.

Figure 3.12 demonstrates the typical evolution of the above energy terms normalized with E_0, hereafter denoted by E_P^*, E_I^*, E_D^*, and E_K^*, with respect to the normalized time t^*, defined as the ratio of the collapse time t divided by characteristic time τ_c (where $\tau_c = \sqrt{h_0/g}$). The basal friction does affect the energy conversion. As the basal friction decreases, more potential energy converts into basal dissipated energy, while less converts to internal energy. This is because

smaller basal friction leads to larger run-out distance, that means an increase in the E_D^* and reduction E_I^*. Figure 3.12(c) and (d) reveal that for a = 1.5 (<1.7), the potential energy is transformed into internal energy E_I^* (frictional) and kinetic energy E_K^* at similar proportions, with frictional behaviour dominating. However, for a = 2.75 (>1.7) the potential energy transforms primarily into kinetic energy initially (small E_I^*), supporting the pressure gradient domination of the flow. This also supports the choice of a = 1.7 as the critical aspect ratio in Figure 3.5.

Figure 3.13 presents the maximum value of E_K^* respect to aspect ratios under different basal friction. It appears to show two critical values, that coincide with the previously defined critical values a = 1.7 and a = 10 (blue and red dash line in Figure 3.13). Overall, the influence of basal friction on the maximum value of E_K^* is minimal though (see the inset of Figure 3.13). This can also be observed in Figure 3.12 because most of the kinetic energy is mobilised in all cases earlier than the basal energy E_D^* that remains to that point negligible.

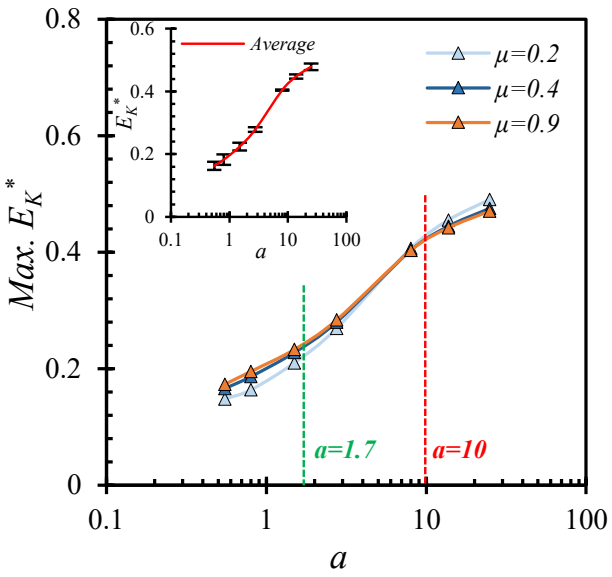

Figure 3.13 The maximum E_K^* in the energy conversion analysis. The mean line and its standard deviations for μ = 0.2, 0.4, and 0.9 are depicted in the inset figure.

Figure 3.14 presents the final stage value of E_P^*, E_I^*, E_D^*, and E_K^* for different aspect ratios. E_P^* increases as basal friction increases and decreases vs aspect ratio (see Figure 3.14(a)). The variation in E_D^* decreases rapidly as the base friction increases (see Figure 3.14(b)). Surprisingly, our results indicate that E_D^* gradually increases with a for smaller base friction conditions, but decreases with a for larger base friction conditions. The hinge point is around $\mu \sim 0.5$ which coincides with the value shown in Figure 3.10 delimiting an area in terms of final deposit height. It confirms the relationship between base friction and final height. For values of $a > 10$, E_D^* seems to be independent of basal friction. This demonstrates that when a increases, the collapse mechanism transitions from being controlled by basal friction transitions to primarily being governed by pressure gradients. This observation is further supported by E_I^* (see Figure 3.14(c)).

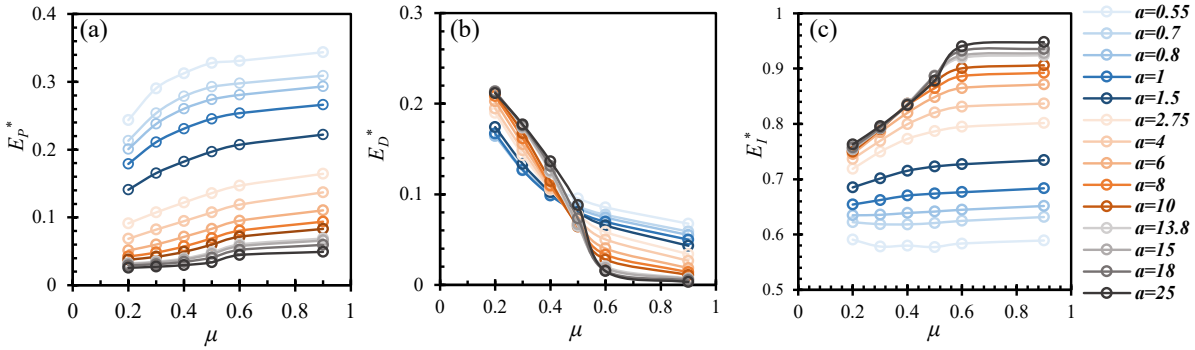

Figure 3.14 Correlations between basal friction and final stage energy terms (E_P^*, E_D^*, and E_I^*) in different aspect ratio cases. The blue colour, orange colour and grey colours present the low, medium, and high aspect ratio cases, respectively.

3.5.5. Front flow kinetic energy analysis

Polanía et al. (2022) propose a simplified model with the analogy of a sliding block with an initial velocity and opposite resistance such that: $M\ddot{x}(t) = -k\dot{x}(t)$, where $\ddot{x}(t)$ and $\dot{x}(t)$ are the block acceleration and velocity, respectively, and k is an equivalent suspension viscosity. The relevant derivation process of the model is shown in the Equations. (3.27)-(3.29). Based on their methods, we investigated the basal friction effect on the flow front kinetic energy, as shown in Figure 3.15. It was found that the effects of basal friction on R^* decreases as E_K^U increases (see Figure 3.15(b)). This further supports that, in high columns, the collapse mechanism is governed by the gravity pressure.

$$L_\infty - L_0 = MU/k, \tag{3.27}$$

where, U is the velocity in the steady stage of fluids resulting from the whole column mass M.

Both sides divided by L_0 and include E_K^U, in Equation (3.27), obtaining

$$L^* = \frac{\sqrt{2}}{kL_0}\sqrt{M}\sqrt{E_K^U} \tag{3.28}$$

where the kinetic energy during the steady propagation stage as $E_K^U = MU^2/2$, with $M = \sum_i^{N^p} m_i = \emptyset_0 \rho_p h_0 l_0$, where m_i denotes the mass of each particle.

According to Equation (3.28), obtaining

$$L^* \propto \sqrt{M}\sqrt{E_K^U} \tag{3.29}$$

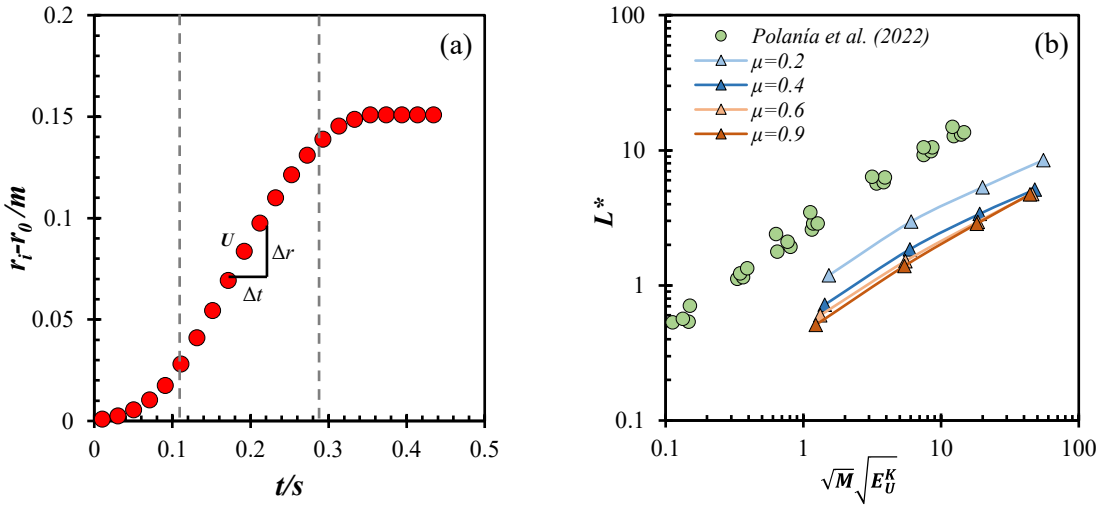

Figure 3.15 (a) The evolution of front position r_i for sample (μ = 0.6 and a =1.5). Dashed grey lines delimit the collapse steady propagation interval. (b) Scaling of the normalized run-out distance L^*(our study R^*) with column kinetic according to Equation (3.28) different basal frictions.

3.6. Conclusion

In this study, we have used SPH to systematically analyse the effects of basal friction on gravity-driven particle column collapse, which is both concluded the outside and internal conditions. An SPH model validated against experiments has revealed the following findings:

(1) Run-out distance, final deposit height, and final deposit morphology are all affected by the basal friction.

(2) To predict the run-out distance, we propose a modified formula ($R^* = \alpha \cdot a^{\beta}$) that incorporates the basal friction coefficient. Our analysis reveals that the basal friction coefficient μ has an obvious effect on the coefficient factor α in the formula while the exponent parameter β remains unaffected. This model shows two extreme conditions: for $\mu = 0$, the collapsed grains would never stop and thus $R^* \to \infty$; while for $\mu \to \infty$, every grain would become quiescent at all times as long as it touches the substrate, under which the column can be deemed collapsed onto one layer of its composed grains. That is to say, the influence of basal friction converges to that of grain friction. Somewhat surprisingly, for low aspect ratio models, the minimum run-out distance increases linearly as the aspect ratio increases, with a slope of 0.7536. And this value is equal to the tan value of the internal friction angle (tan 37° = 0.7536) of the materials. This means the minimum run-out distance depends on the material internal friction angle.

(3) The basal friction also exerts an influence on the final height. We observed that the basal friction does not affect the linear increase stage (where the model maintains the initial height), but it becomes more relevant in the other stages. Particularly for larger values of a, the final height decreases as the aspect ratio increases. Specifically, an increase in the friction coefficient affects

the separation point (maximum final height) between the power increase stage and the decrease stage, resulting in an increase in the aspect ratio corresponding to the maximum final height. However, we observe a convergence of the effect of basal friction on the final height when $\mu >$ 0.5. The effect of base friction was also studied using an energy conversion analysis that confirmed many of the previously stated findings. Critically, it shows that a critical base friction coefficient of $\mu \sim 0.5$ exists after which, the final non-dimensional height remains constant, as shown above.

(4) The basal friction also affects the deposit regime. The competition mechanism between the initial column aspect ratio and basal friction coefficient reveals two transition zones that delimit the three main deposit regimes reported in the literature. In zone 1 (regime I to regime II), the friction coefficient varies from 0.1 to 0.2 and the aspect ratios between 0.5 and 0.8. Zone 2 (regime II to III) is defined by values of friction coefficient between 0.3 to 0.7 and aspect ratios from 8 to 25.

(5) The energy conversion analysis also confirms the critical aspect ratios at $a = 1.7$ as transition from a friction-dominated to pressure gradient dominated flow. Additionally, it confirms that for values $a \sim 10$ (affected by the friction coefficient, μ), a regime transition exists that explains the different deposit morphologies.

(6) Refer to the front kinetic energy of Polanía et al. (2022), we investigated the basal friction effect on the flow front kinetic energy. It was found that the effects of basal friction on R^* decreases as E_K^U increases. This also supports that in high columns, the collapse mechanism is governed by the pressure gradient.

4 Effect of Gravity Level on the Granular Column Collapse

In this study, we investigated the effect of gravity level on the collapse of granular column using Smoothed Particle Hydrodynamics (SPH) method based on the Mohr-Coulomb model. After validating our model against existing experimental studies, we conducted a dimensional analysis of the system's scaling factors to assess the effect of varying gravity levels. The results show that gravity significantly influences the collapse dynamics, particularly in shortening the collapse time. To predict collapse time, we proposed two models that consider varying gravitational acceleration (g), both of which scale positively with $n^{-1/2}$ (where $g = nG$, n is the gravity scaling factor, and G = 9.81m/s^2). We find that the non-dimensional collapse time, t_∞/τ_c (where t_∞ is the collapse time, and $\tau_c = \sqrt{h_0/g}$, with h_0 representing the initial height), is not a constant value but is influenced by the initial aspect ratio. While gravity does impact collapse dynamics, its effects on the deposit run-out distance and final height consistently scaled at 1.0 across varying gravity levels. Additionally, we propose a modified mobility angle, θ', to investigate the effect of gravity on flow mobility, which aligns with expected gravity scaling. Furthermore, our findings are supported by observations of natural landslides in the Solar System. A multiscale analysis reveals that the run-out distance of collapse is contingent on the sample volume and initial potential energy as opposed to gravity. This study has potential applications for investigating the collapse mechanisms of granular materials in planetary exploration.

This Chapter was published in the following paper:

Yucheng Li* and Raul Fuentes (2025). Granular column collapse: Analysing the effects of gravity levels. *Computers and Geotechnics*, volume 183, 107207.

4.1. SPH Model

4.1.1. Model set-up

The SPH theory and constitutive model framework are described in Section 3.1 and 3.2. The dimensions of the granular column collapse model are illustrated in Figure 3.3(a). It consists of a cylindrical domain placed over a rigid horizontal surface. The friction coefficient, μ, between the rigid plane and SPH particle was set to 0.4 in accordance with the validation experiments conducted by Lube et al. (2004). Figure 3.3(b), (c), and (d) illustrate a sensitivity analysis of different particle spacings (Δp = 2.0, 3.0 or 5.0mm, representing the initial distance between adjacent particles) for an aspect ratio of 0.55. A red circle with a radius of 0.176 m was used as a standard reference size for better comparisons. Balancing computational cost and accuracy, the particle spacing, Δp = 3.0 mm was chosen for all simulations in this study.

The gravitational acceleration scaling factor, denoted as n (where $g = nG$, n = 1/6, 1/3, 1, 2, and 10, and G = 9.81m/s^2), is a crucial parameter in the simulation. Note that in the models, only the column height and gravitational acceleration was changed, while the column radius (r_0 = 0.1m) remained constant. The material density was 2600 $kg.m^{-3}$, the angle of friction was 37°, Poisson's ratio was 0.3, and Young's modulus was 6.0 MPa. A wide range of granular column aspect ratios are presented in Table 4-1.

Table 4-1 Series of example granular column collapse.

Case ID	$a = h_0/r_0$	h_0 /m	No. of particles
1	0.55	0.055	63,378
2	1.0	0.10	119,714
3	1.5	0.15	176,050
4	2.75	0.275	323,932
5	4	0.4	471,814
6	6	0.6	704,200
7	10	1.0	1,176,014
8	13.8	1.38	1,619,660
9	18	1.8	2,112,600
10	25	2.5	2,932,993

4.1.2. Model validation

The numerical model was validated against the experiments of Lube et al. (2004) under the Earth's gravitation acceleration, focusing on three key aspects: deposit pattern, run-out distance, and final height. Figure 3.4 presents deposit patterns of numerical simulations and experimental results. Depending on the aspect ratio values results, three distinctly different deposit patterns are shown.

For small aspect ratios (e.g., a = 0.55), a flat surface remains at the top of the model; for intermediate aspect ratios (e.g., a = 2.75), the top surface changes from a flat plate to a conical tip; for large aspect ratios (e.g., a = 13.8), the sand forms an outward propagating wave during the process, transferring mass from the centre to the edge of the diffusion. Our numerical flow patterns agree well with their experimental results (Lube et al., 2004, Lajeunesse et al., 2004) and numerical results (Man et al., 2021a, Sheikh et al., 2021). Importantly, the collapse time scales are matched with experiments (Li et al., 2024) and the final collapse time will be further investigated in Section 4.2.2.

Figure 4.1(a) shows the validation of the run-out distance. Our simulation results agree well with the experimental results of Lube et al. (2004), both for lower and higher aspect ratios. Our results of final height, h_∞, are plotted in Figure 4.1(b) and are in good agreement with the experimental and formula (see Equation (3.24)). The critical aspect ratio also fits well with the 1.0 proposed by Lube et al. (2004). When the aspect ratio is less than 1.0, the model shows circular truncated cones pattern. The model maintains the initial height (e.g., a = 0.55, see Figure 3.4). The morphology becomes more complex when the aspect ratio exceeds 1.0 (e.g., a = 2.75 or a = 13.8, see Figure 3.4). Although our initial validation against Lube at al. (2004) is only valid for 1G, the subsequent comparison to other experiments at other gravities (see Figure 4.6) provide further evidence the approach is appropriate.

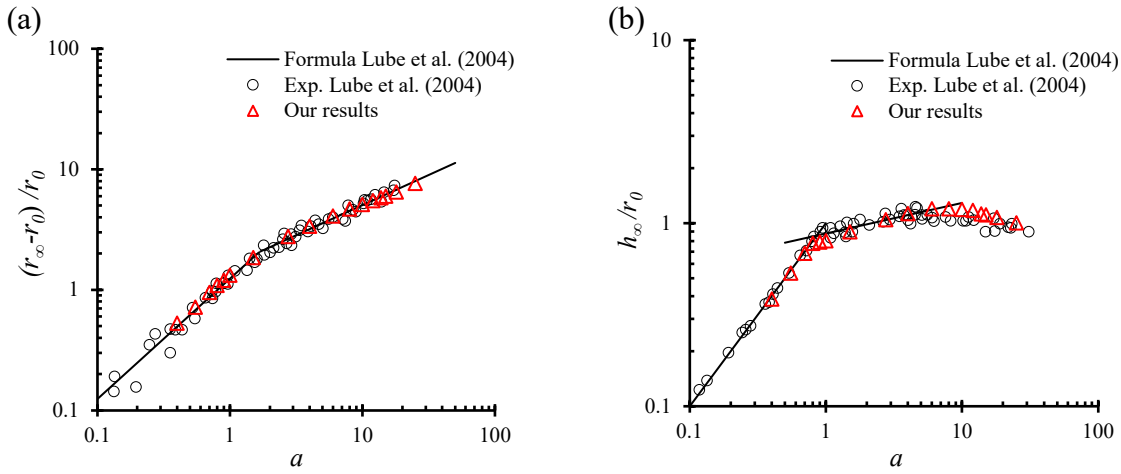

Figure 4.1 Validation of our numerical results (μ = 0.4) with experimental results of Lube et al. (2004). (a) run-out distance; (b) final height.

4.1.3. Assumption of scaling factors

Before analysing the results, we assume that the gravity level should obey certain scaling laws. To validate this assumption and extend it to other aspect ratios, and regimes, we conduct a scaling analysis of the problem, starting from a hypothesis that scaling derived from simple dimensional analysis is sufficient. The actual scaling factors of this hypothesis assume a scaling n of gravity and a scaling of 1.0 for density and length. This leads to the overall scaling factors shown in Table 4-2. In the following sections, we will compare these values with those in the literature and our

obtained results. It must be noted that we are using a purely frictional material here, characterised by the angle of shear resistance that scales as 1.0. In other material types with viscous effects or with cohesion, additional scaling factors will be needed.

Table 4-2 Scaling factors assuming a simple dimensional analysis. *Indicates enforced scaling parameters in the system.

Variable	Units	Scaling values
L^*	m	1
ρ^*	kg/m^3	1
g^*	m/s^2	n
F	N	n
$Stress$	N/m^2	n
v	m/s	$n^{1/2}$
t	s	$n^{-1/2}$
$Energy$	J	n

4.2. Results

4.2.1. Typical evolution of avalanche flow patterns

In Figure 4.2, a typical aspect ratio (e.g., $a = 4$) was used to demonstrate the effect of gravity levels on the evolution of flow patterns. As expected, higher gravity levels accelerate the collapse process. This is consistent with the conclusion of Meruane et al. (2010), who claimed that the flow velocity and duration of emplacement are gravity dependent. Our findings are further supported by Yang et al. (2024), who demonstrated that the run-out distance positively correlates with gravity at the steady flow time-scale ($2\tau_c$). In our case, this corresponds to $a = 4$, $t = 0.4$s (see Figure 4.2). Zheng et al. (2024) also showed similar results using DEM. Additionally, we initially find that the varying gravity levels produce same deposit morphologies (bottom row of Figure 4.2). This indicates that the gravity has a significant influence on the dynamics of the collapse of granular column but no impact on the deposit morphology.

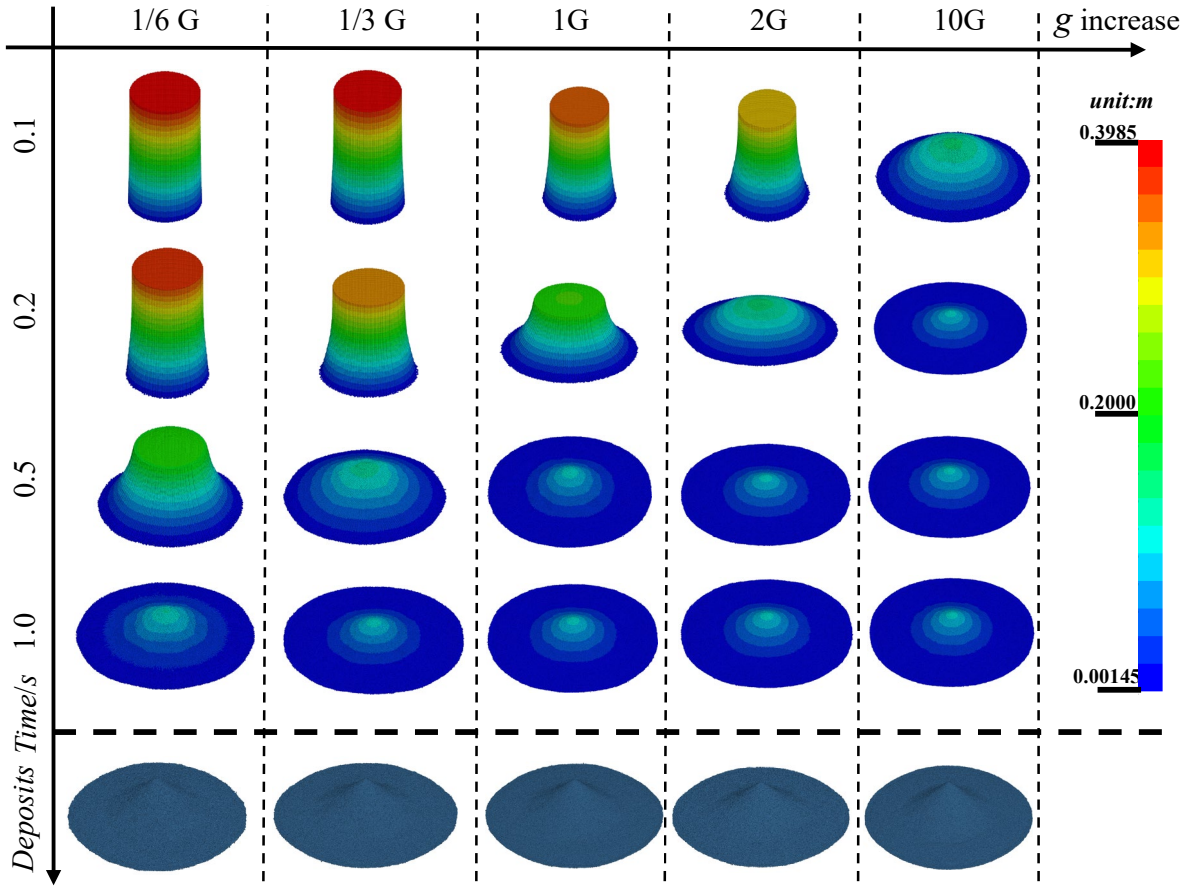

Figure 4.2 Snapshots of granular column collapse at different gravity levels. The bottom blue pictures are deposit morphologies.

4.2.2. Collapse time prediction models

4.2.2.1. Scaling by the initial geometry

The relationship between scaling factor (n) for varying gravity and the collapse time of a granular column was investigated. Lube et al. (2004) investigated scenarios with the same gravitational acceleration (g) but different initial radius (r_0 = 2.9, 7.5, and 9.7cm). Their findings indicated that different values of r_0 have no effect on the non-dimensional collapse time.

$$\frac{t_\infty}{\sqrt{r_0/g}} = f(a) \tag{4.1}$$

In this work, we keep r_0 constant while varying gravity levels to examine the effect of gravity on collapse dynamics. Figure 4.3 shows the non-dimensional collapse time and scaling laws derived from our results. Our new correlation is presented in Equation (4.2) with a value of R^2 = 0.995. This scaling by $1/\sqrt{g}$ aligns with the observations of Lube et al. (2004). Both our results and the experiments of Lube et al. (2004) demonstrate an increasing trend in non-dimensional time as the

aspect ratio increases. We observe a deviation for values of a larger than 5.0. The fit is satisfactory for $a < 5.0$, with discrepancies only present in scenarios with larger aspect ratios. The reason for this deviation may be the insufficient data for larger aspect ratios in their experiments. Another possible reason is the difficulty in determining the collapse time experimentally for these models due to their complex deposit morphology, as illustrated in Figure 3.4.

$$\frac{t_\infty}{\sqrt{r_0/g}} = 3.776 * a^{0.35} \tag{4.2}$$

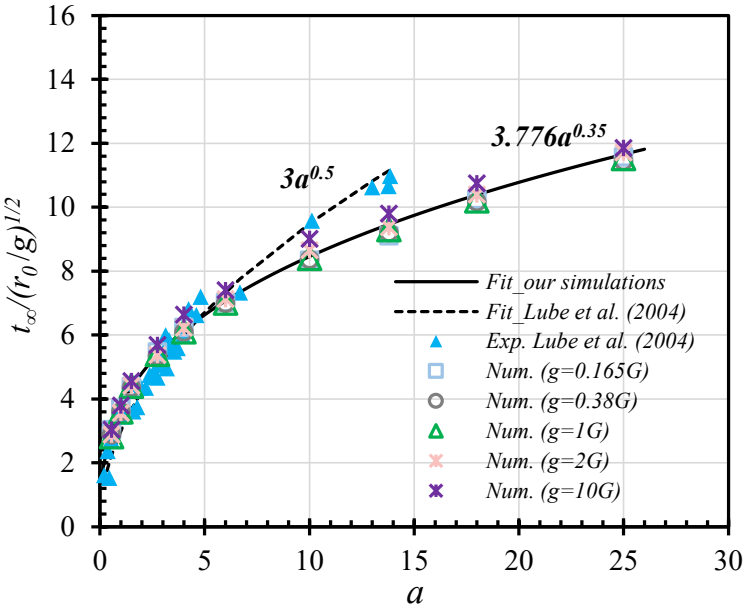

Figure 4.3 The scaling laws of collapse time and the scaling laws obtained from regression analysis for different gravity levels.

4.2.2.2. Scaling by the characteristic time

Another approach for predicting collapse time was used based on the analysis of single-particle free fall, where $h = \frac{1}{2}gt^2$, then $t = \sqrt{2h/g}$. Here, by introducing the characteristic time scale τ_c ($\tau_c = \sqrt{h_0/g}$) to evaluate the collapse time, we derive Equation (4.3) with $R^2 = 0.97$, and illustrate the fitted results in Figure 4.4.

$$\frac{t_\infty}{\sqrt{h_0/g}} = \frac{t_\infty}{\tau_c} = \frac{3.712}{a^{0.14}} \tag{4.3}$$

Lajeunesse et al. (2005) claimed that the propagation evolution can be differentiated into three sections. In the first section ($t < 0.8\tau_c$), the collapse process accelerates, resulting in the spreading of the deposit tip in a positive horizontal direction. Subsequently, the foot of the material propagates at nearly constant velocity for about $2\tau_c$. In the final section, the material propagation decreases until it reaches the final deposit position after approximately $0.6\tau_c$. They defined approximately $3\tau_c$ as a guide value for the total duration of the collapse. However, our results

show that the non-dimensional collapse time (t_∞/τ_c) is not a constant value, but it is also affected by the initial aspect ratio. The experimental data of Lube et al. (2004) supports this conclusion. Specifically, at lower aspect ratios ($a < 5.0$), the non-dimensional collapse time tends to decrease rapidly, and this trend diminishes as the aspect ratio increases. Based on Equation (4.3), we conclude that the ratio of the collapse time to the free-fall time ($t_\infty/\sqrt{2\,h_0/g}$) of a single particle decreases as the aspect ratio increases (see the black dashed line in Figure 4.4). This finding complements the results of Lube et al. (2004), who reported that the collapse time of granular materials in columns is approximately twice the free fall time (see the green dashed line in Figure 4.4). The discrepancy may lie in the higher columns, whose collapse mechanism is predominantly influenced by pressure gradients, resulting in a short collapse time that tends to a free-fall state. Furthermore, we find that the fit between the scaling free-fall time (see the black dashed line in Figure 4.4) and the theoretical free-fall time (see the red dashed line in Figure 4.4) is also affected by the initial aspect ratio. As the aspect ratio increases, the fit improves and eventually stabilizes.

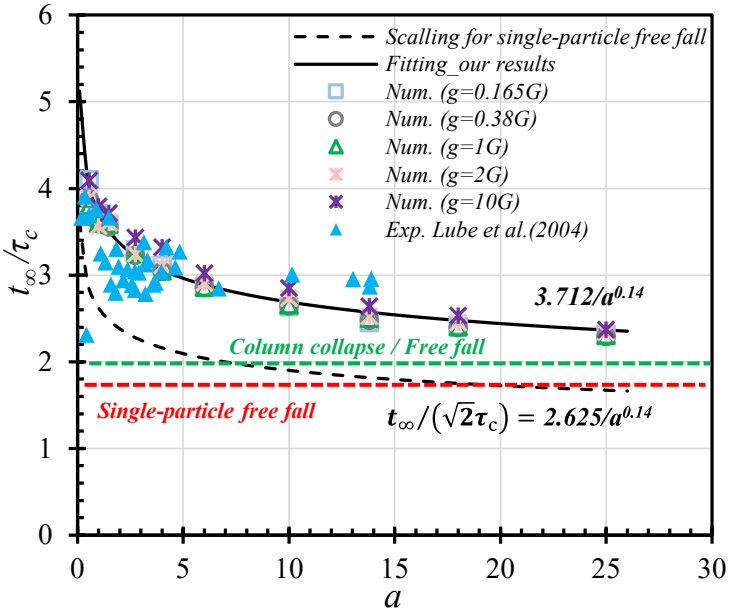

Figure 4.4 Influence of gravity level on the collapse time normalized by the characteristic time. The black dashed line is the scaling line for single-particle free fall condition ($t_\infty/(\sqrt{2}\,\tau_c)$) derived from the regression analysis of simulation results (black line).

Empirically, Equation (4.2) or Equation (4.3) can be easily compared, as both are derived from dimensional analysis and can be converted into each other, demonstrating consistency and validity. In both equations, the collapse time is positively correlated with $1/\sqrt{g}$, represented as $n^{-1/2}$, agreeing with previous studies that assumed scaling factors in Table 4-2. This suggests that we can use Equations (4.2) or (4.3) to estimate the collapse time at different gravity levels, once knowing the necessary parameters.

4.2.3. Angle of repose

The hollow cylinder method is a common method for determining the static angle of repose of cohesionless materials. The advantage of the final deposit morphology in the lower aspect ratio model is that it maintains a flat surface at the top, while the sliding surface is nearly flat, as depicted in Figure 4.5(a), which facilitates accurate measurement of the angle of repose. Consequently, we selected a value of a = 0.55 to examine the effect of gravity level on the angle of repose. We symmetrically averaging four points α_{repose}, denoted as the angle of repose. The calculated angle of repose is approximately 26.5° across different gravity levels, indicating that the angle of repose is not dependent on gravity levels, as shown in Figure 4.5(b). This finding is consistent with previous experimental studies (Nakashima et al., 2011, Marshall et al., 2018).

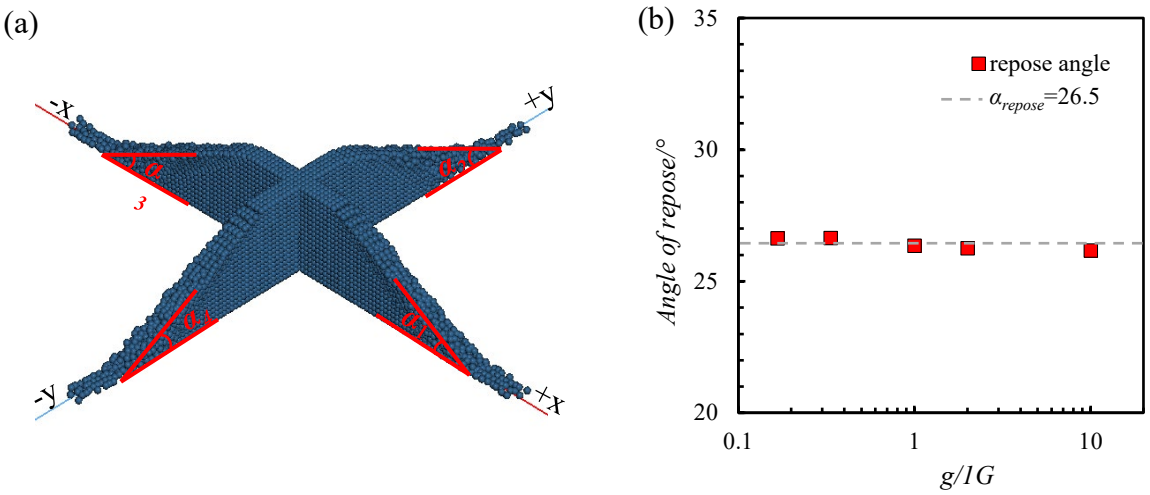

Figure 4.5 (a) Measurement of angle of repose at a = 0.55, $\alpha_{repose} = (\alpha_1 + \alpha_2 + \alpha_3 + \alpha_4)/4$. (b) Angle of repose at different gravity levels (1G = 9.81m/s²).

4.2.4. Run-out distance

Figure 4.6 presents the correlation between run-out distance and aspect ratio at different gravity levels. The expected scaling of 1.0 is clearly shown, indicating that the gravity level does not impact the normalized run-out distance. Moreover, the gravity level does not alter the critical aspect ratio at which the shift occurs in the piecewise power-law relationship shown in Figure 4.6. It remains a constant value of 1.7, as noted in Table 3-3.

Additionally, large-scale results, such as the natural landslides in the Solar System (Lucas et al., 2014), present a regression line with a slope of 12.64 and an R^2 vale of 0.87. Notably, the landslides on Mars and Iapetus also align well with this regression line, supporting our conclusion about the consistent effect of gravity on run-out distance across different celestial bodies. This finding is consistent with the work of Roche et al. (2011), who normalized the run-out distance of the Valles Marineras (Lajeunesse et al., 2006, Lucas et al., 2011), delimited by blue dashed lines with slopes of 3.3 and 11.5 (see blue arbitrary lines in Figure 4.6). While their results indicate a larger value compared to both our simulations and experimental findings, this can be explained by the fact that

natural landslides travel unexpectedly long distances, indicating lower dissipation. However, the precise physical processes underlying energy dissipation during natural granular flows remain uncertain (Lucas et al., 2014).

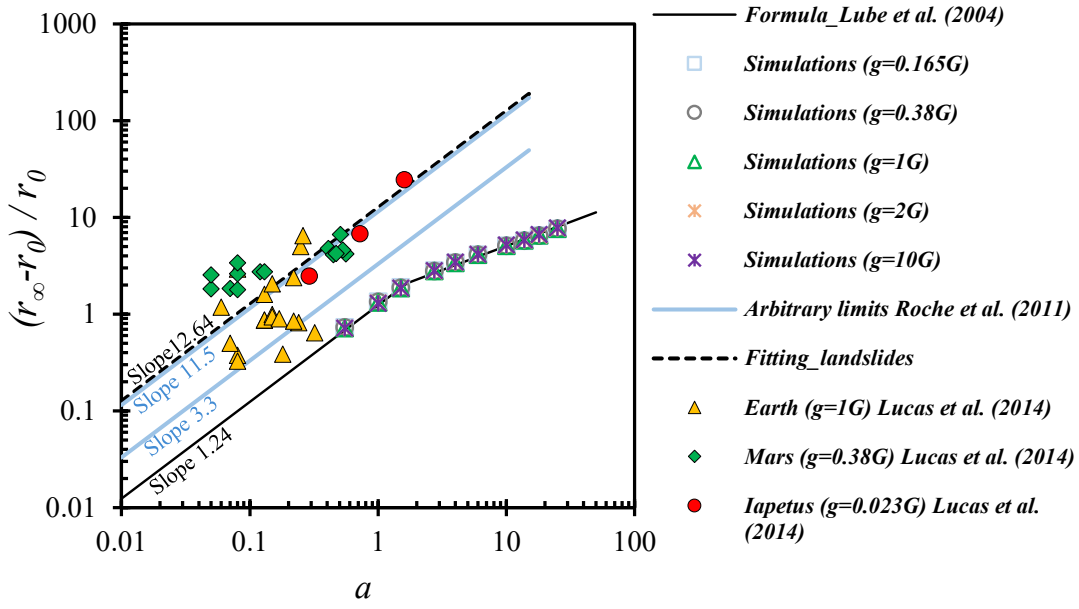

Figure 4.6 Influence of gravity level on the normalized run-out distance. The natural data of landslides in Earth, Mars, and Iapetus are referenced from Lucas et al. (2014).

4.2.5. Final height

Figure 4.7(a) presents the rescaled final height at various aspect ratios. Again, the expected scaling of 1.0 is consistently observed across different aspect ratio ranges. The results also align well with our proposed formula for final height when $a > 10$ (as indicated by the blue and red lines in the inset of Figure 4.7(a)). However, some minor differences appear in this region and therefore, we have investigated the effects of gravity for $a = 25$ to understand their extent (see Figure 4.7(b)). The deposit morphology appears very similar, as depicted in the inset of Figure 4.7(b). Notably, we observed a slightly lower final height under high gravity condition (e.g., g = 10G), although the effect was negligible.

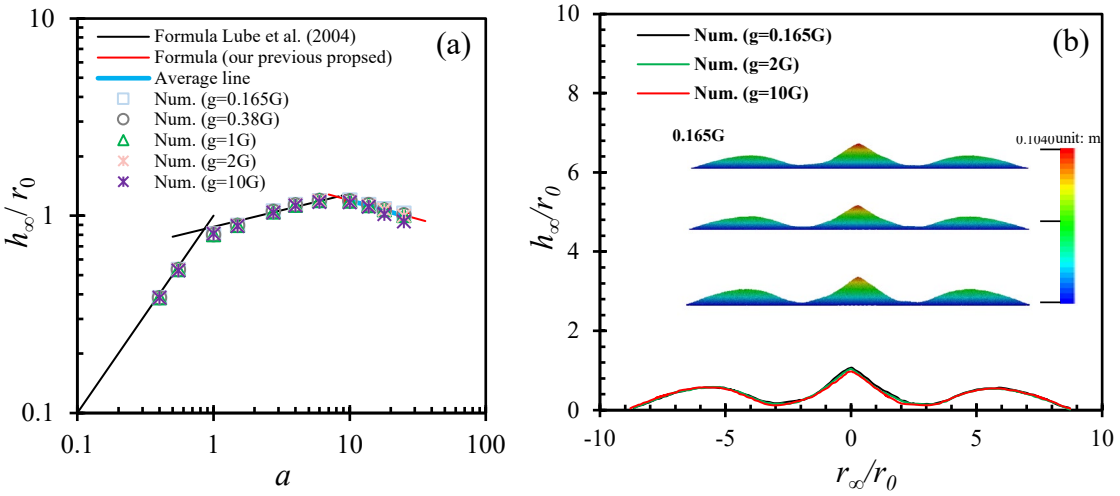

Figure 4.7 (a) The rescaled final height versus aspect ratio under different gravity conditions. (b) Deposit profiles $f(r,h)$ normalized to the column radius. The deposit cross-section profiles of a = 25 (height coordinates) at different gravity levels (0.165G, 2G, and 10G) are presented in the inset.

4.2.6. Flow mobility

The particles in dry granular flow under the driving force of gravity. It is very important to quantitatively analyse the effect of gravity levels on the flow mobility. Our current objective is to employ a quantitative method to evaluate how the level of gravity affects the overall flow mobility. The reciprocal of granular flow mobility is measured by the ratio of h_∞ and r_∞ (Cagnoli and Piersanti, 2015, Lai et al., 2017) in Equation (4.4). The angle θ is referred to as the flow mobility angle (see Figure 4.8). The higher the flow mobility of the avalanche, the smaller the angle. To evaluate the flow mobility of materials flowing out of the initial geometry, we introduced another mobility angle, θ', in Equation (4.5). This angle is referred to as the modified flow mobility angle (see Figure 4.8(a)).

$$tan\theta = h_\infty/r_\infty \tag{4.4}$$

$$tan\theta' = h_\infty/(r_\infty - r_0) = h^*/r^* \tag{4.5}$$

It is observed that both θ and θ' decreases as the aspect ratio increases, following the expected scaling with the gravity level. θ exhibits a small peak point at $a \approx 1$, which is attributed to the effect of initial geometry. A straightforward validation, as depicted in the inset of Figure 4.8, illustrates that when $a < 0.8$, the model, dominated by friction, maintains the initial height h_0. As a increases, h_0 increases more rapidly than r_∞, leading to an increasing trend for θ. Only when $a \geq 0.8$, h_∞ decreases with r_∞, resulting in a lower θ. Conversely, θ' eliminates the effect of the initial geometry (r_0), and the curve undergoes continuous variation. As the aspect ratio increases, the initial geometry effect diminishes, eventually causing θ' to approach θ.

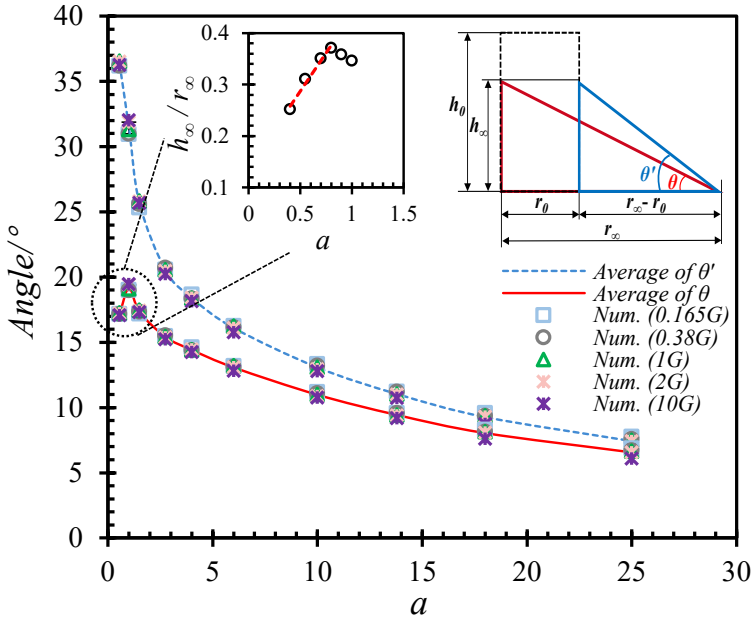

Figure 4.8 The effect of gravity levels on the flow mobility. The sketch of mobility angle θ and θ' are shown in the inset. The inset also shows the validation results for model at μ = 0.4 and g = 1G.

4.3. Discussion

Comparing experimental or simulation results with actual engineering data is essential for validating and refining the model, as well as for understanding its applicability in real-word scenarios. As depicted in Figure 4.6, the aspect ratio of natural landslides typically falls well below 1.0 and in a much narrower range compared to experiments. Consequently, using aspect ratio as a criterion for analysing the large-scale landslides may not be suitable. Motivated by this, we investigated the effect of gravity level on the relationship between the length travelled (ΔL) and landslide initial volume, as shown in Figure 4.9. We use the initial volume because it is the most widely available landslide descriptor in the literature for real landslides. The results suggest that the run-out distance is independent of gravity level, which is consistent for small-scale and large-scale slides. Through regression analysis, a critical point in volume was identified, corresponding to $1.5 \leqslant a \leqslant 2.75$. This critical point closely corresponding to the transition point of 1.7 identified by Lube et al. (2004). For volumes less than this critical point, our simulation results, along with experimental findings (Warnett et al., 2014), exhibit a linear increasing trend as volume increases. Conversely, for volumes greater than this critical point, our small-scale results fit well with large-scale landslide data, showing a power increase trend. This finding is consistent with previous research by Lajeunesse et al. (2005), who suggested that in lower columns, collapse is primarily influenced by friction, while in higher columns, it is governed by pressure gradients. The existence of this critical point also reflects the transition phase between the influence of slide volume effects on the spreading distance at small and large scales.

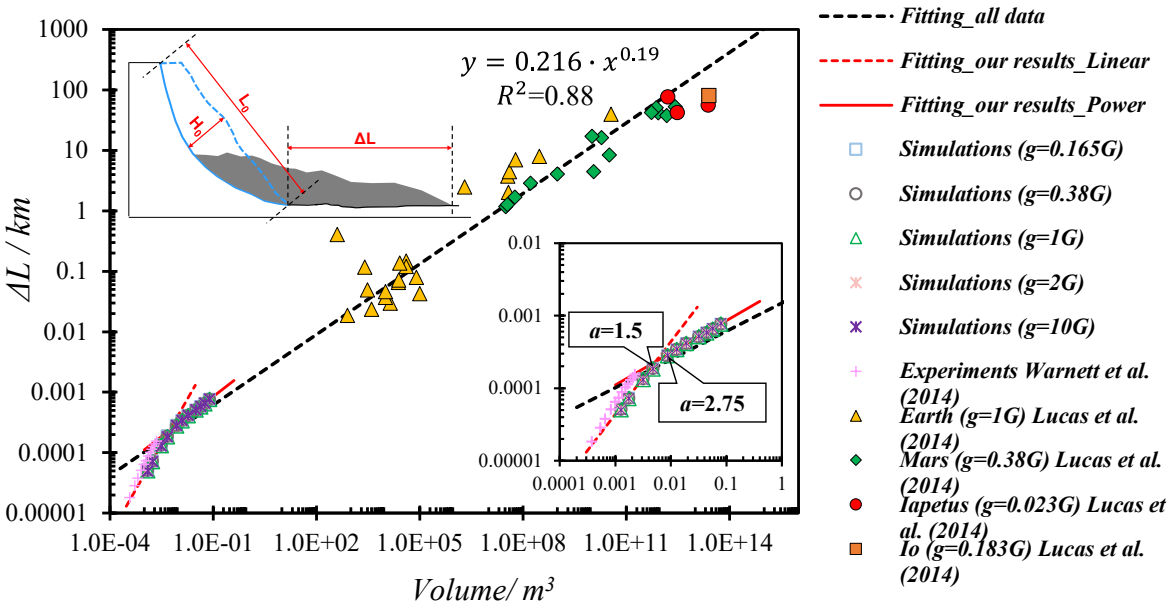

Figure 4.9 The travel length (Δ*L*) as a function of volume. H_0 is the maximum initial thickness, L_0 is the initial length, and Δ*L* is the travel length by the front landslide. The inset figure illustrates the most frequent geometry for natural landslides, where the dashed blue region represents the initial geometry, and the grey region represents the deposit geometry. The volume corresponding to the aspect ratio point is depicted in the inset figure. The fitting formula for landslide data (Lucas et al., 2014) is also shown in the inset.

The maximum kinetic energy (E_K) under different gravity levels also scales well with a scaling factor of n, as shown in Figure 4.10. That further supports that the gravity level does not influence the deposit run-out distance.

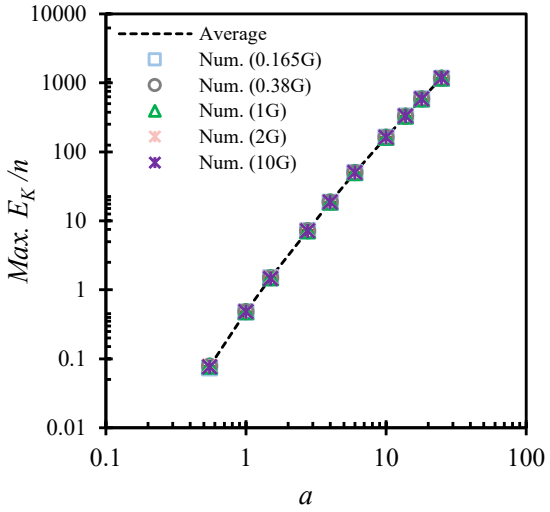

Figure 4.10 The maximum of kinetic energy E_K scaled by a factor of n at different aspect ratios.

Strom et al. (2019) also analysed the dependency of run-out distance or affected area on the product of $V \times H_{max}$, which is a proxy to initial potential energy. We compared our small-scale simulation results and the experimental findings of Warnett et al. (2014) with large-scale landslide data from the Solar System (Lucas et al., 2014), as shown in Figure 4.11. We constructed a best-fit regression line (depicted as a black dashed line in Figure 4.11), achieving an R^2 value of 0.87. This highlights the consistency of small-scale results with large-scale landslide data, emphasizing the significance of potential energy as a crucial factor influencing deposit run-out distance. Moreover, the obtained regression line validates that the gravity level scales according to our proposed model scaling. Additionally, the total potential energy of our simulations aligns well with a scaling factor n across different aspect ratios, as illustrated in the inset of Figure 4.11.

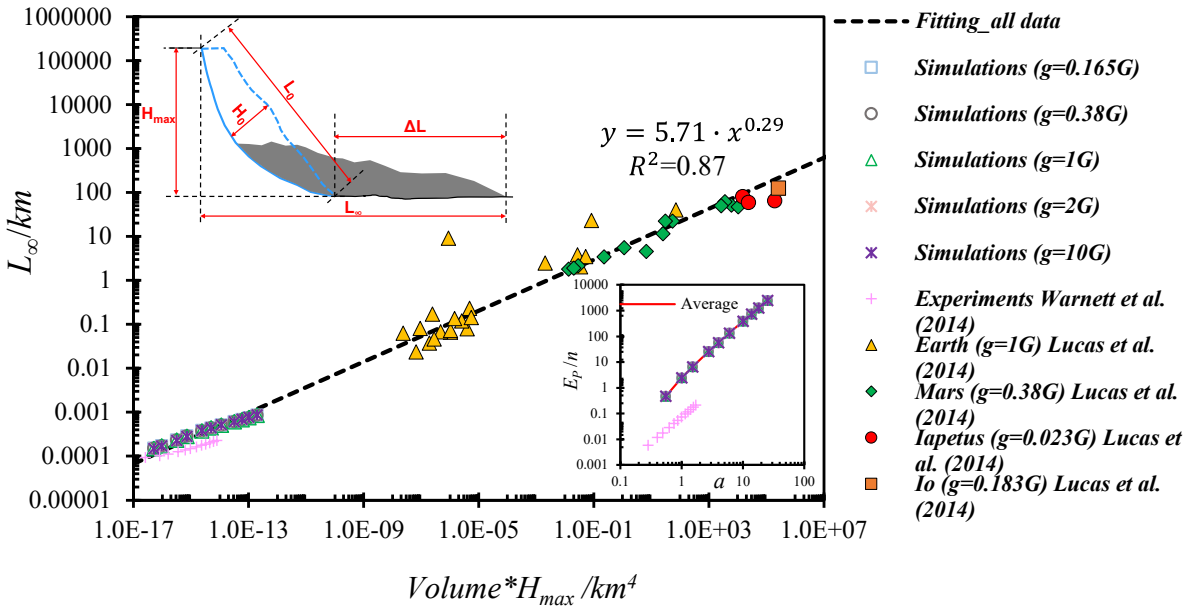

Figure 4.11 The relationship between run-out distance and product of landslide volume and maximal height at various gravity conditions. Here, H_{max} is the maximum elevation of the initial mass, H_0 is the maximum initial thickness, and L_∞ is the total travel length of the landslide.

4.4. Conclusion

In this study, we use the Smoothed Particle Hydrodynamics (SPH) model and literature results to investigate the effects of gravity conditions on gravity-driven particle column collapse. Specifically, we explore how varying gravity levels influence collapse behaviour through a scaling analysis of non-dimensional collapse time, deposit geometry, and energy analysis. The findings are summarized as follows:

(1) Higher gravity levels significantly shorten the collapse time of granular columns while maintaining similar deposit morphologies. This suggests that gravity levels play a significant role in the dynamics of collapse but have no impact on the deposit morphology.

(2) To accurately predict the collapse time of granular columns, two models were proposed, each accounting for different gravity levels. Both models demonstrate a positive correlation with $1/\sqrt{g}$, represented as $n^{-1/2}$. We found that the non-dimensional collapse time (t_∞/τ_c) is not a constant but influenced by the initial aspect ratio. We also found that the ratio of the collapse time to the free-fall time ($t_\infty/\sqrt{2\,h_0/g}$) of a single particle decreases as the aspect ratio increases, eventually tends to a free-fall state.

(3) Gravity levels appear to have minimal effect on deposit run-out distance and final height. The expected scaling of 1.0 is clearly observed, suggesting that gravity level does not affect the normalized run-out distance. This conclusion aligns with observations of natural landslides in the Solar System. Moreover, the gravity level does not alter the critical aspect ratio (a = 1.7), where a shift occurs in the piecewise power-law relationship. The rescaled final height remains consistent across various aspect ratio ranges, supported by cross-sectional analysis of deposit profiles for a = 25. Notably, only under high gravity condition (e.g., 10G) was a slight decrease in final height observed, although the effect was negligible and may be due to small numerical issues.

(4) Flow mobility was used to quantitatively describe the effect of gravity levels on deposit results. A modified mobility angle (θ') was proposed to eliminate the effect of the initial geometry (r_0). It was observed that both θ and θ' decreases as the aspect ratio increases, following the expected scaling of the gravity level. θ exhibits a small peak point at $a \approx 1$, which is attributed to the effect of initial geometry. Conversely, the curve of θ' undergoes continuous variation. As aspect ratio increases, the initial geometry effect diminishes, eventually causing θ' to approach θ.

(5) Through multiscale studies exploring the genesis of collapse geometry in terms of volume or height drop, we observed that small scale results (e.g., experiments) are in good agreement with large scale results (e.g., landslide). Notably, under identical scaling conditions (e.g., identical density, length, etc.), the extent of collapse appears to be independent of gravity level. Instead, it is found to depend on sample volume and initial potential energy. The sample volume factor exhibits a clear scale effect, with the critical point occurring at around a = 1.7. Furthermore, both gravitational potential and kinetic energies demonstrate a good scaling relationship with n, providing additional support for the conclusions drawn from an energy perspective.

5 Experimental Study of the Effects of Particle Shape on Granular Materials Collapse

As evidenced by the literature reviewed in Section 2.5, numerous researchers have investigated the influence of particle shape on collapse behaviour using both experimental and numerical approaches. In these studies, particle shape was often coupled with other particle properties, including density, size, and stiffness. While some numerical studies employed idealised particle shapes in order to eliminate the influence of other mechanical parameters, these shapes may not fully represent those observed in real-world scenarios. Consequently, the impact of particle geometric parameters - such as convexity, particle aspect ratio, and roundness - on flow dynamics and deposit morphology remains insufficiently understood.

This research, therefore, aims to address this gap by conducting a systematic and comprehensive investigation of the effects of a wide range of particle shapes on key features of granular flow responses. To achieve this objective, spherical harmonics (SH) functions are used to represent and reconstruct three-dimensional grains, which are then input into a high-precision 3D printing device, enabling the production of more realistic particles. The advantages of this approach include: (1) the capability to analyse particles with realistic geometries, incorporating both concave and convex features. This enhances the resemblance of the results to real-world disaster scenarios compared to those obtained using idealised shapes; (2) full control over shape parameters such as sphericity and roundness while maintaining a constant equivalent-sphere diameter. This ensures that particle shape is the only variable, whereas other mechanical properties (e.g., Young's modulus, density, and tensile strength) remain unchanged. Following this, we design an experimental platform to conduct granular column collapse experiments.

The content of Chapters 5 and 6 will be submitted to the following paper:

Yucheng Li, Deheng Wei*, Chongpu Zhai, Raul Fuentes. The Role of Particle Shape in Granular Materials Collapse. *Journal of Geophysical Research: Solid Earth* (on preparation).

5.1. Fundamentals of spherical harmonic functions

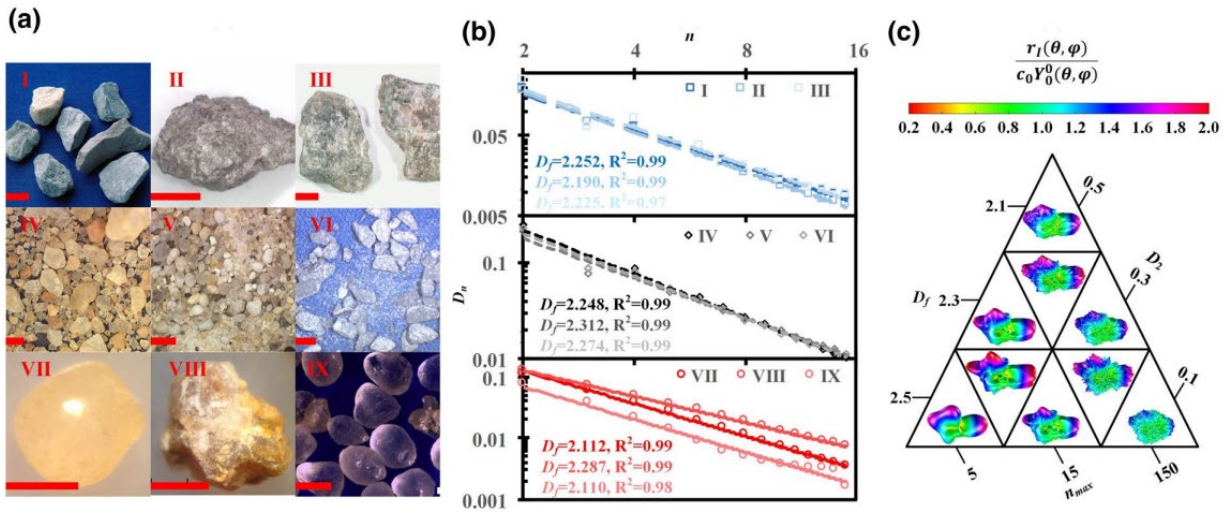

Figure 5.1 The framework for generating virtual particle shapes from experimentally scanned grains. (a) Nine types of real particles with scale bar being 1cm. (b) The Relationship between D_n and n in log-log scales for grains in (a). (c) Virtual representation of generated particle shapes using various maximum SH degree, n_{max}, D_f and D_2. The colour bar represents the ratio of normalized radial distance to radius of its c_0-determined sphere. Pictures represented from Wei et al. (2021)

For spherical surfaces, through 3D Fourier Transformation, any function set on the surface can be represented as a sum of Spherical harmonic (SH) function, $Y_n^m(\theta,\varphi)$. Here, we use spherical harmonic functions to reconstruct the particles (Wei et al., 2018). The SH method expands the polar radius of the particle surface from a unit sphere and calculates the coefficients of the SH fraction, as shown in Equation (5.1).

$$r(\theta,\varphi) = \sum_{n=0}^{\infty}\sum_{m=-n}^{n} c_n^m Y_n^m(\theta,\varphi), \tag{5.1}$$

where $r(\theta,\varphi)$ is the polar radius from the particle centre with the corresponding spherical coordinates $\theta \in [0, \pi]$ and $\varphi \in [0, 2\pi]$ in polar coordinate system. c_n^m is the associated SH coefficients to be determined, and the calculation of c_n^m is shown in Appendix E. $Y_n^m(\theta,\varphi)$ is the SH function given by Equation (5.2):

$$Y_n^m(\theta,\varphi) = \sqrt{\frac{(2n+1)(n-m)!}{4\pi(n+m)!}}\, P_n^m(\cos\theta) e^{im\varphi}, \tag{5.2}$$

where n and m are the degree and order of the associated Legendre function $P_n^m(x)$ which can be expressed by Rodrigues's formula (Askey, 2005):

$$P_n^m(x) = (1-x^2)^{|m|/2} \cdot \frac{d^{|m|}}{dx^{|m|}}\left[\frac{1}{2^n n!}\cdot \frac{d^n}{dx^n}(x^2-1)^n\right]. \tag{5.3}$$

Figure 5.1(a) shows nine types of real granular materials of wide-scoped sizes, and the scaling exponential relations in Figure 5.1(b) indicate

$$D_n \propto n^{\beta}, \tag{5.4}$$

where D_n is the SH descriptor, normalised L_2 norm ($D_n = \sqrt{\sum_{m=-n}^{n} \|c_n^m\|^2}\,/c_0$), β is the slope of the regression plot of log (D_n) versus log (n). Consequently, following Russ (2013) and Quevedo et al. (2008), D_n can be expressed in terms of SH fractal dimension (D_f):

$$D_n = D_2 \cdot \left(\frac{n}{2}\right)^{2D_f-6}, \tag{5.5}$$

The detailed derivation of fractal dimension D_f, the random SH coefficients of virtual grains, and the calculation of particle volume are presented in Appendix. E. The SH functions were used to generate stereolithography (STL) files for both experimental applications (3D-printed grains) and DEM simulations (implementation of polyhedral particles). Different particle shapes were obtained by adjusting the fractal dimension (D_f) and D_2.

5.2. 3D printed grains

3D printing offers the unique capability to produce particles with independent control over morphology and material properties, which are intrinsically coupled in naturally occurring geomaterials. However, recent studies in geotechnical engineering primarily focused on whether 3D-printed grains can reproduce the characteristics of natural particles. From a topological morphology perspective, the answer appears negative, owing to limitations in printing resolution and the effectively unbounded complexity of real particle surfaces. For instance, Hanaor et al. (2014) argued that the surface area of real granular materials is theoretically infinite. Hence, the successful generation of realistic virtual particle geometries is a prerequisite for meaningful 3D printing of grains. Most irregular shapes are produced as one-to-one replicas of CT data to assess their ability to capture real granular behaviour. As highlighted in pioneering work on 3D printable geomaterials (Hanaor et al., 2016), besides printing resolution and materials, emphasis should be placed on the geometrical model of printed grains. The key advantages of this approach include: i) extracting morphological and statistical parameters from real particles; ii) depicting a wide range of realistic particle morphology features, including smoothed faces, angularity, and branching; iii) facilitating the study of effects induced by varying morphology.

In recent years, owing to its ability to generate particles with controlled morphology and material properties, 3D printing has gained popularity in studies of granular collapse (Zhang et al., 2021a, Wang et al., 2024). Various printing techniques are available for 3D printing, as outlined in Table 5-1. To reduce costs, grain assemblies are often printed as a unit rather than as individual particle, as depicted in Figure 5.2(c). In this study, we used the MJP 3600 (see Figure 5.2(a)), a poly-jet layer-printing 3D printer, and the build material was a UV-curable plastic (VisiJet M3 Crystal)

with a tensile strength of 42.4Mpa. The SH functions were used to generate stereolithography (STL) files for 3D printing. Different particle geometries were obtained by adjusting the fractal dimension (D_f) while keeping D_2 fixed at 0.1. The input particles exhibited uniform grading with the diameter of approximately 2mm, as shown in Figure 5.3(a). Additional shape parameters are presented in Figure 5.3(b)-(d).

Table 5-1 Summary of investigated 3D printing techniques (Adamidis et al., 2020)

Technique	Material	Resolution	Support Removal	Time and Cost
Stereolithography (SLA)	Photopolymer	~ 24 μm(z) ~ 140 μm(x/y)	Manual removal	Quick affordable
PolyJet	Photopolymer	~ 16 μm(z) ~ 40 μm(x/y)	Solution bath	Quick affordable
Selective laser sintering (SLS)	Metal, glass, ceramic, plastic powder	~ 50-150 μm(z) ~ 200-300 μm(x/y)	No support	Material-dependent
Selective laser melting (SLM)	Metal powder	~ 50-100 μm	No support	Quick, expensive
Nanoscribe photonic professional GT	Photopolymer	< 1μm	…	Slow, expensive

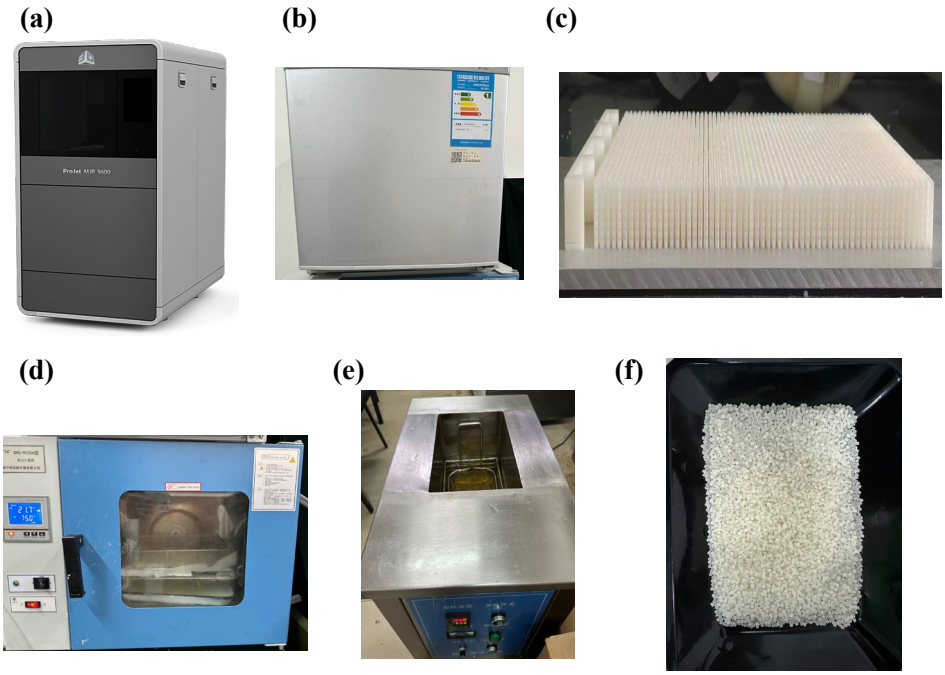

Figure 5.2 PolyJet 3D-printing process: (a) printing platform of MJP 3600. (b) cooling treatment of printed particles. (c) printed particles before support material removal. (d) hot blower box for melting and dewaxing. (e) acoustic oil bath. (f) 3D-printed grains.

After printing, to facilitate particle removal from the build plate and to improve their mechanical stability, the printed grains were subjected to a 30-minute cooling treatment in freezers, as illustrated in Figure 5.2(b). To reduce material consumption, grain assemblies rather than individual particles were printed. Each batch comprised of seven layers of particles, arranged in 60 rows and 60 columns per layer, as shown in Figure 5.2(c). Subsequently, a hot-air blower was used to melt and remove surface wax, eliminating approximately 95% of the wax. An acoustic oil bath was then used to further remove residual wax (see Figure 5.2(e)). After manual cleaning of oil residues using detergent, the final 3D-printed grains were obtained (see Figure 5.2(f) and Figure 5.3(e)). The printing precision was within 5% of the input geometries, as proven by X-Ray CT images.

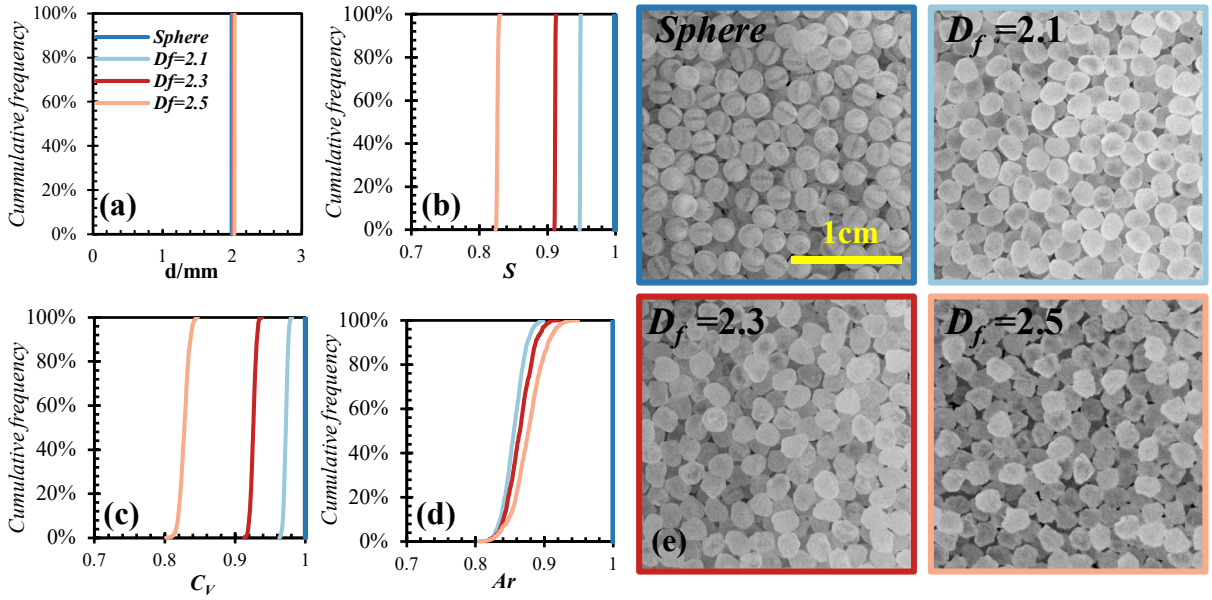

Figure 5.3 Cumulative distributions of classical shape indices of printed particles. (a) Equivalent-sphere diameter (d ≈ 2mm). (b) Sphericity (*S*). This parameter describes how close the particle is to a sphere, with $S_p = \sqrt[3]{36\pi V^2}/S$ reflecting the deviation of surface area from its volume-equivalent sphere. (c) Convexity (C_v). This parameter quantifies the relative volume of concave features, calculated as $C_V = \frac{V_a}{V_c}$, where V_a and V_c are the volumes of the aggregate and its perfect convex hull. (d) Particle aspect ratio (A_r). This parameter compares three principal dimensions, defined as $A_r = E_i \times F_i$, with mean elongation and flatness $E_i = p_2/p_1$ and $F_i = p_3/p_2$, respectively, where p_1, p_2, and p_3 are the particle's principal dimensions calculated by principal component analysis. (e) Snapshots of printed grains.

5.3. Rectangular channel collapse experiments

5.3.1. Experimental platform

Figure 5.4 illustrates the platform designed for granular materials collapses experiments, comprising four main components: a glass tank, fixed frames with a basal surface, a lifting system, and recording system.

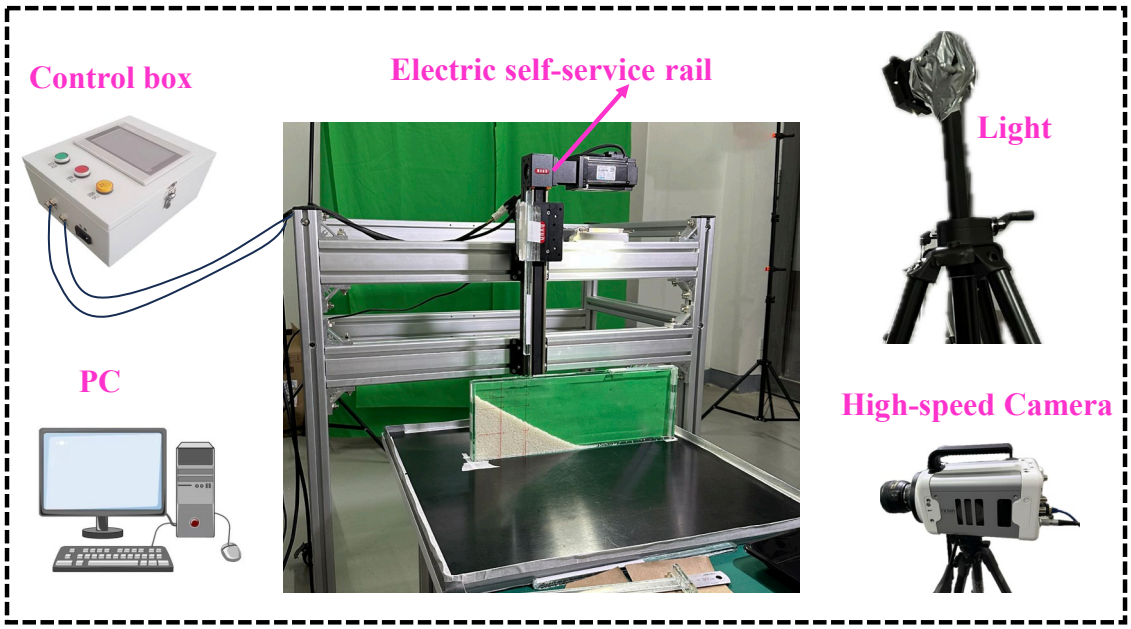

Figure 5.4 Picture of the experimental platform. This picture represents a basic overview of the experimental platform, including the lifting system, recording system, fixed frames with the basal surface, and the high-speed camera used for data capture.

The basal surface consisted of an insulated Bakelite board, which is characterised by electrical insulation, low static charge, and high wear resistance, making it well suited for our experiments. To minimize experimental uncertainty, the basal surface was levelled to within a horizontal deviation of less than 0.1°, as validated using an electronic inclinometer before each test.

For the lifting system, an electric self-service rail was employed. It offers two key advantages: a programmable, servo-motor-controlled lifting speed, allowing precise calibration of the lifting speed, and strictly vertical motion of the confining walls (see Figure 5.4). The slider mounted on the rail platform enabled different assemblies to be fixed, allowing multiple experimental configurations, such as a glass gate for rectangular channel collapse tests and a cylinder column for granular column collapse tests. Lai et al. (2017) demonstrated that longer wall-removal times reduce the run-out distance. To avoid this effect, previous studies used high lifting velocities: for example 1.6m/s (Lajeunesse et al., 2004) and 1.8m/s (Warnett et al., 2014). In this study, a constant gate-lifting velocity of 1.6m/s was adopted, which was sufficient for our experiments.

The electric self-service rail was mounted on the glass tank, measuring 500mm in length, 200mm in height, and 12mm in width. The 12mm channel width was selected based on the criterion that

the width should be at least six times the mean particle diameter to eliminate width effects, as recommended by Owen et al. (2009) and Lai et al. (2023). This minimal-width criterion helps optimise the number of particles required in both experiments or simulations.

For the record system, a high-speed camera (Photron S9) with a resolution of 1024×1024 pixels and a fame rate of 2000 frames per second was positioned in front of the flume to capture the flow kinematics. The experiments were conducted at the State Key Laboratory for Strength and Vibration of Mechanical Structures, Xi'an Jiaotong University, China.

5.3.2. Experimental set-up

In this work, we utilized four types of printed particles to perform rectangular channel collapse experiments. Some key influencing factors are briefly introduced as follows:

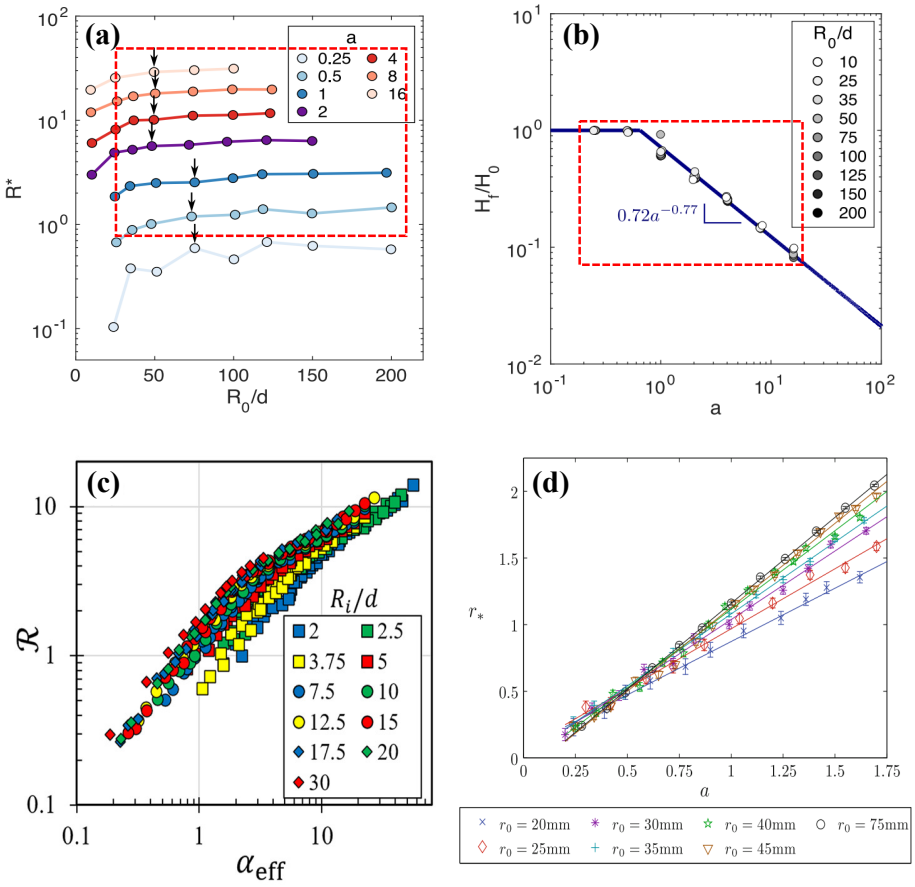

Figure 5.5 Grain size effects were investigated extensively in previous studies: (a) and (b) findings from the 2D DEM study conducted by Cabrera and Estrada (2019); (c) 3D DEM study of Man et al. (2021b); (d) Examination of the relationship between r^* and a for varying cylinder radii r_0 by Warnett et al. (2014), where corresponding r_0/d ranged from 28-107.

Cabrera and Estrada (2019) highlighted grain-size effects in two-dimensional (2D) DEM simulations of granular materials collapse. As illustrated in Figure 5.5(a) and (b), the run-out distance and final height become insensitive to grain size when $r_0/d \geqslant 25$ and $a \geqslant 0.5$. They recommend that r_0/d should exceed 75 for short columns and 50 for tall columns to avoid size

effects. However, their conclusions were based on 2D simulations, and their applicability to three-dimensional systems remains uncertain.

In a related three-dimensional (3D) DEM study, Man et al. (2021b) examined grain-size effects over the range r_0/d = 2-30 in granular column collapse using Voronoi-based spheropolyhedron particles (Galindo-Torres and Pedroso, 2010). Their results indicate that the run-out distance becomes effectively independent of grain size when $r_0/d > 15$ (Figure 5.5(c)). Furthermore, in the experimental study by Warnett et al. (2014), the initial conditions involved sieved grains with diameters between 0.6mm and 0.8mm, resulting in r_0/d values ranging from 28 to 107. Their results revealed a linear relationship between r_0/d and deposit run-out distance (Figure 5.5(d)). Taken together, these findings collectively emphasize the significance of accounting for grain-size effects in granular materials collapse studies, particularly when DEM simulations or laboratory experiments are employed.

It's worth noting that, although grain size can influence collapse outcomes, the present study primarily focusses on particle shape effects, especially when particles with equal volume are used. The influence of grain size can therefore be minimised by selecting an appropriate grain size threshold. To balance result accuracy with the cost of 3D printing (which also related to computational cost in DEM simulations), a uniform value of $r_0/d = 25$ was adopted in the numerical simulations. In the laboratory setting, the ratio r_0/d was set to 50 for low columns and 25 for high columns. This approach ensures consistency across the experimental configurations while accommodating practical constraints associated with 3D printing and laboratory testing.

The filling procedure was standardized for all experiments. The packing density of the grains was estimated by

$$\theta = \frac{M}{\rho \cdot w \cdot L_0 \cdot H_0}, \tag{5.6}$$

where, M is the total mass of the granular materials, ρ is the material density, w is the width of the rectangular channel, L_0 is the length of the initial sample, and H_0 is the initial height of the initial sample.

Although Kermani et al. (2015) demonstrated that the deposit run-out distance is insensitive to solid fraction, all filling procedures were carefully controlled in the present experiments to ensure consistency. The measured packing densities ranged from 0.62 to 0.65, closely matching those reported in quasi-2D tests (0.61 - 0.63) reported by Lajeunesse et al. (2005) and in axisymmetric experiments (0.62-0.65) by Lajeunesse et al. (2004). Furthermore, no signs of electrostatic charge transfer, such as unusual dust accumulation on the particles and glass walls, or humidity effects, such as the formation of particle aggregates, were observed.

The collapse experiments were performed using particles of each shape at two typical column aspect ratios, namely a = 1.24 (low aspect ratio) and a = 2.45 (high aspect ratio). To improve the statistical reliability of the results, eight independent tests were conducted for each configuration, and two tests exhibiting the largest deviations were excluded. Subsequently, the remaining six datasets were then averaged to obtain more robust and reproducible results.

5.4. Results and discussion

5.4.1. Flow and deposit morphology

Figure 5.6 presents the evolution of flows composed of particles with different shapes. It is observed that the fractal dimension (D_f) exerts a significant influence on flow patterns. As fractal dimension increases, the flow pattern undergoes changes, accompanied by a delay in collapse time.

The flow and deposit patterns are observed to be almost trapezoidal or triangular in shape. These patterns, as observed in two-dimensional projections, correspond to the simi-geometrical shapes described in Section 3.5.3 for three-dimensional systems. For consistency and clarity, the trapezoidal pattern is referred to as 'Regime I', and the triangular pattern as 'Regime II'. For low columns (a = 1.24), both Regime I and Regime II are observed, and as D_f increases, the deposit morphology transitions from Regime II to Regime I. For high columns (a = 2.45), only Regime II is observed.

The initial collapse disturbance region is also influenced by D_f. During the early stage ($1\tau_c$), the collapse slips line propagates inwards (see the dashed blue lines in Figure 5.6). As D_f decreases, the particles disperse more readily and collapse more uniformly as a bulk. Specimens with higher D_f exhibit greater overall stability, consistent with the initial velocity field results (see Section 6.4.3), which is attributed to enhanced inter-particle interlocking.

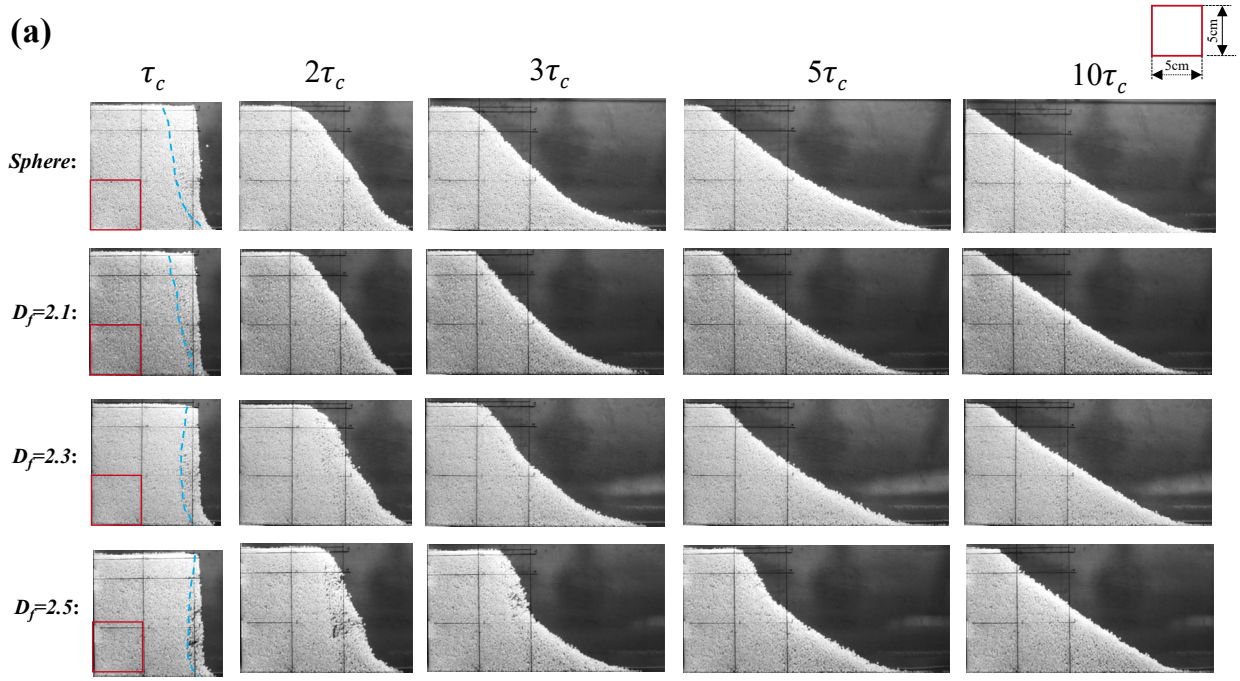

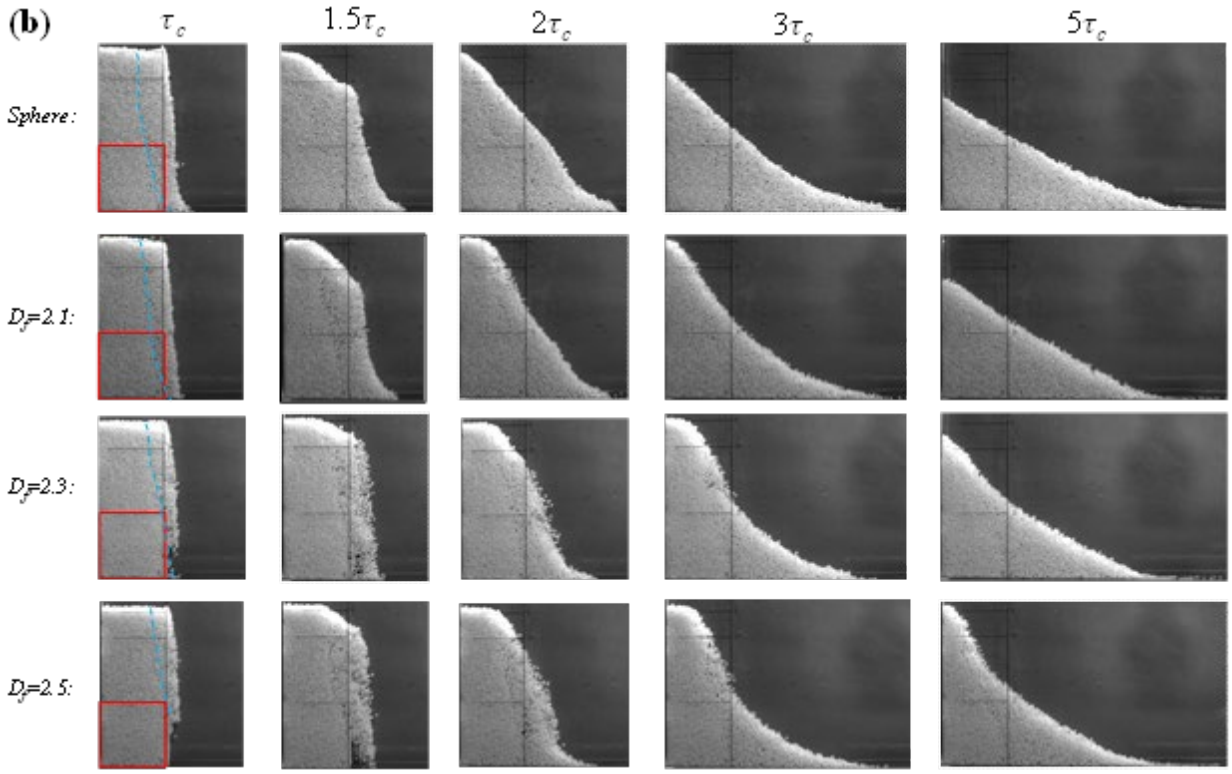

Figure 5.6 The effect of particle shape on the evolution of flow patterns for both a = 1.24 and a = 2.45. Each image is calibrated with the red square serving as a reference point. The dashed blue line separates the initial disturbance region and static region.

5.4.2. SAM model

According to the literature, most studies have traditionally analysed collapse behaviour primarily in terms of depositional results, such as run-out distance. However, this approach captures only the final extent of the collapse and does not provide a comprehensive description of the overall behaviour of the flow dynamics. In this study, we therefore focus on how particle shape influences the dynamic evolution of the collapse process.

Segment Anything Model (SAM) is a new AI model from Meta AI (Alexander Kirillov et al., 2023) that can “cut out” any object, in any image. (see Figure 5.7(a)). SAM is a promotable segmentation system with zero-shot generalization to unfamiliar objects and images, without the need for additional training. The model is designed and trained to be promotable, so it can transfer zero-shot to new image distributions and tasks. Evaluations conducted across various tasks demonstrate SAM’s impressive zero-shot performance, often matching or surpassing previous fully supervised results. Moreover, the model has been utilized to build the largest segmentation dataset to date (by far), with over 1 billion masks on 11M licensed and privacy respecting images. In this study, the SAM model was used to determine the centre of mass of the sample. The simplified steps for determined the centre of mass of the sample is shown in Figure 5.7(b) - (d).

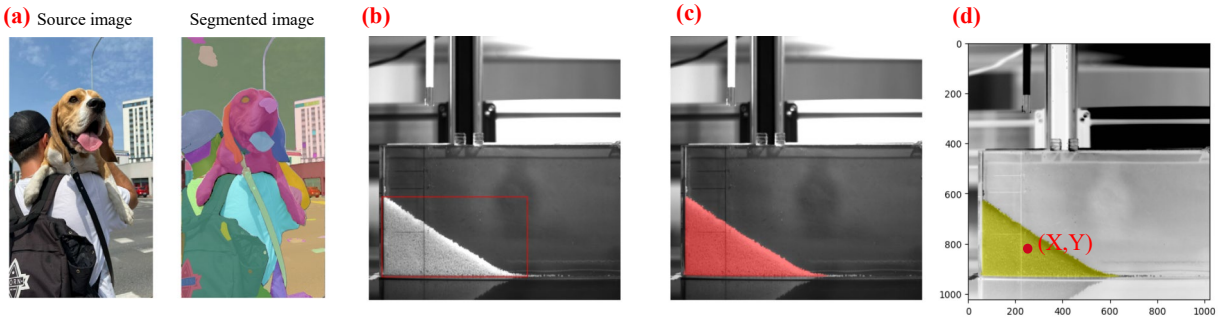

Figure 5.7 The steps for determining the centre of mass of a sample with the SAM model. (a) Sketch for the segment results. (b) Defining the scope of identification. (c) Mask generation. (d) Determination of centre of mass.

The evolution of the centre of mass coordinates for a = 2.45, is depicted in Figure 5.8. The centre of mass is influenced by the particle fractal dimension. Consistent with the observed flow patterns, sphere particles exhibit the largest horizontal (x) displacement and the smallest vertical (y) displacement. As D_f increases, the x-coordinate converges towards a same value, indicating a similar final deposit position, but at different rates, reflecting distinct flow dynamics. In contrast, the y-coordinate increases with increasing D_f throughout the entire collapse process, confirming that the system becomes progressively less mobile as particle irregularity increases.

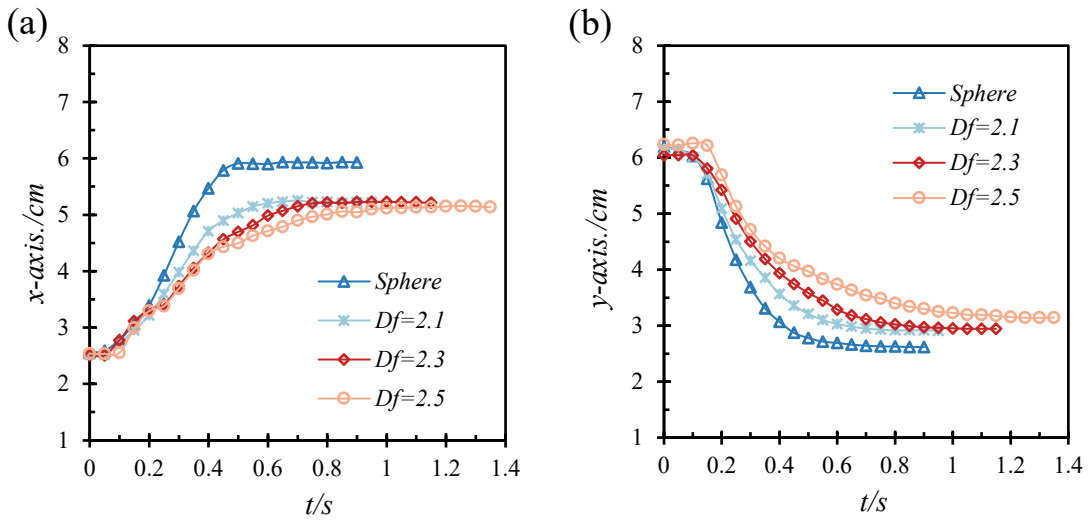

Figure 5.8 The evolution of the centre of mass coordinates of the sample with a = 2.45: (a) x-coordinate. (b) y-coordinate.

5.4.3. Deposit run-out distance and final height

Figure 5.9 illustrates the deposit geometries for different fractal dimensions. It is observed that the normalized run-out distance decreases as the fractal dimension increases for both a = 1.24 and a = 2.45, as shown in Figure 5.9(a). For a = 2.45, the final height increases as fractal dimension increases, resulting in a triangular deposit regime, as shown in Figure 5.9(b). In contrast, for a = 1.24, the final height nearly unchanged (except for the spherical particles, which show only a very

small difference and can therefore be classified as Regime II), which is attributed to the system's tendency to preserve the initial height after collapse, characteristic of a trapezoidal regime at such small aspect ratios.

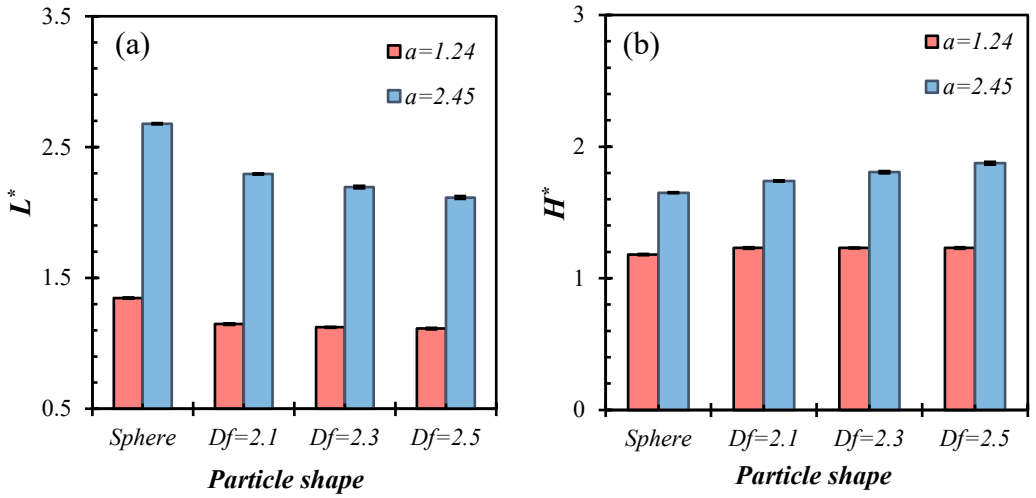

Figure 5.9 Deposit geometry (run-out distance & final height) of different fractal dimensions. (a) Normalized run-out distance. (b) Rescaled final height.

5.4.4. Angle of repose

Figure 5.10 presents the angle of repose of the different 3D-printed materials. The measurement procedure for the natural angle of repose is described in Appendix. D. As anticipated, spherical particles exhibit a substantially smaller angle of repose (27.36°) than particles with fractal dimensions D_f = 2.1(36.28°), 2.3(36.10°), and 2.5(37.88°). Except for spherical particles, which are classified as "Very free-flowing", all other shaped particles fall into the category of "Free flowing", according to the flowability classification given in Table 5-2.

Interestingly, no clear monotonic relationship is observed between the particle fractal dimension (D_f) and the angle of repose. The angle of repose is controlled by multiple factors, including geometrical descriptors of particle shape (e.g. sphericity and roundness), particle size, frictional properties (sliding, rolling, and internal friction), moisture content, airflow, and the measurement method. In this study, the absence of a clear trend is attributed to the complex interaction of these factors. One potential contributing factor is the packing density, which reaches a maximum when $0.6 < Ar < 1$ (Meng et al., 2012). Particles with higher packing densities may yield larger angles of repose, further highlighting the multifaceted nature of particle behaviour.

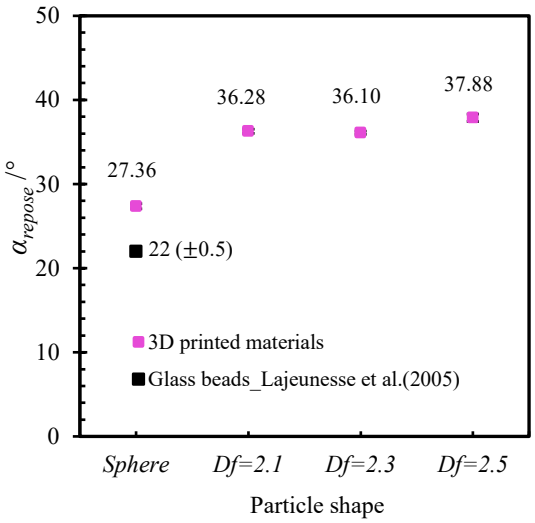

Figure 5.10 Angle of repose of different shaped particles.

Table 5-2 Classification of flowability of powder based on repose angle (Beakawi Al-Hashemi and Baghabra Al-Amoudi, 2018).

Description	Repose angle/°
Very free-flowing	< 30
Free flowing	30 - 38
Fair to passable flow	38 - 45
Cohesive	45 - 55
Very cohesive (non-flowing)	> 55

5.5. Conclusion

In this chapter, spherical harmonic (SH) functions were used to reconstruct three-dimensional particles with prescribed shape parameters, which were then employed in experiments to investigate the effect of particle shape on collapse behaviour. The findings are summarised as follows:

(1) The particle shape exerts a significant influence on flow patterns and deposit morphologies. As particle irregularity increases (e.g., D_f), the flow pattern undergoes changes, resulting in a delay in collapse time. At a = 1.24, the deposit pattern shifts from Regime II to Regime I as D_f increases. At a = 2.45, only Regime II is observed across all tested shapes. Specimens with higher D_f demonstrate greater overall stability, which is attributed to enhanced particle interlocking associated with higher fractal dimension.

(2) Tracking the centre of mass further reveals the influence of particle shape on the global stability of the column. The centre of mass is influenced by the fractal dimension. With increasing D_f, the horizontal (x-) coordinate converges to nearly the same value, indicating a similar final run-out distance, but at different rates or speeds, reflecting distinct flow dynamics. In contrast, the vertical (y-) coordinate increases with increasing D_f throughout the entire collapse process, confirming a reduction in mobility for more irregular particles.

(3) The normalized run-out distance decreases with increasing fractal dimension for both $a = 1.24$ and $a = 2.45$. For $a = 2.45$, the final height increases with increasing fractal dimension, consistent with Regime II. However, for $a = 1.24$, the final height remains unchanged (except for the spherical particles, which show only a very small difference and can therefore be classified as Regime II), which is attributed to the system's tendency to preserve the initial height after collapse, characteristic of a trapezoidal regime at such small aspect ratios.

(4) No systematic relationship is observed between the particle fractal dimension (D_f) and the angle of repose.

6 DEM Simulations of the Effects of Particle Shape on Granular Materials Collapse

To further investigate the effect of particle shape on collapse behaviour across a range of aspect ratios, including flow regime, deposit morphology, critical column aspect ratios a_{CL} and a_{CH}, and scaling constants, we encounter practical limitations when conducting experiments on tall columns. This is primarily due to the high cost associated with precision 3D printing of granular materials. In addition, laboratory experiments cannot capture microscale contact behaviour, such as the evolution of inter-particle contact forces during collapse. This research addresses these limitations by importing the particle STL files generated using SH functions into a DEM framework. By employing the SH function, we generate DEM polyhedral particles with prescribed shape parameters. The key advantage of this approach lies in full control over shape descriptors, such as sphericity and aspect ratio, while preserving constant particle volume. This enables a wide range of particle geometries to be represented accurately and allows the influence of each shape parameter to be quantitatively isolated.

The results demonstrate that particle shape exerts a strong control on flow behaviour, deposit geometry, and energy dissipation, although these effects weaken as the aspect ratio increases. As particles depart from spherical geometry, deposit morphologies transition from triangular to trapezoidal, the run-out distance decreases, and energy dissipation is reduced. To elucidate the underlying mechanisms, we introduce a friction mobilization index (I_{AM}) to quantify particle interlocking at the microscale. The analysis reveals that interlocking ability increases with particle irregularity but decreases for taller columns. We further examine the influence of geometric characteristics (i.e., sphericity, convexity, and roundness) on flow mobility. Finally, we propose a predictive model that incorporates particle shape parameters and provides accurate estimates of run-out distance. These findings advance the understanding of granular collapse mechanics and provide a quantitative basis for predicting collapse behaviour across a wide spectrum of particle geometries, with potential applications in natural hazard assessment and planetary surface processes.

6.1. DEM theory

Rocky DEM (Rocky, 2022) software was used in this study. In contrast to many standard DEM codes (e.g., PFC), which use glued spheres (clumps or clusters) to represent angular particles, Rocky DEM uses polyhedral shapes to describe real particles, which can accurately represent shape including sharp corners and edges. Although contact detection using this approach takes more time, Rocky increases computer efficiency due to its GPU parallel solver.

The DEM method is based on discrete particles and defines a contact model between the particles, making it suitable for analysing the granular column collapse behaviour at the particle scale. In the DEM model, granular materials are modelled as rigid particles. The translational and rotational motions of each particle are governed by the Newton's second law of motion as:

$$F_i = m_i \frac{d^2}{dt^2} r_i, \tag{6.1}$$

$$M_i = I_i \frac{d^2}{dt^2} \omega_i, \tag{6.2}$$

where F_i is the resultant force acting on particle i; r_i is the position of its centroid; m_i is the particle mass; M_i is the resultant moment acting on the particle; ω_i is the angular velocity and I_i is the moment of the inertia.

The contact force comprises two parts: forces normal-to-contact plane and forces tangent-to-contact plane. The contact plane is defined as the plane perpendicular to the line connecting the closest points of contact between particles. In our numerical model, the linear spring-dashpot model (Cundall and Strack, 1979) and linear spring Coulomb limit model were employed for all simulations. These models describe the calculations for normal and tangential force in Rocky DEM.

In the linear spring-dashpot model, the normal contact force is composed of a linear elastic repulsive force and a damping force, that is:

$$F_n = K_{nl}\, S_n + \, C_n\, \dot{s}_n, \tag{6.3}$$

where S_n is the contact normal overlap; C_n is the normal damping coefficient; $\dot{s}_n$ is the time derivative of the contact normal overlap. K_{nl} is the normal contact stiffness, defined as

$$\frac{1}{K_{nl}} = \begin{cases} \frac{1}{K_{nl,p1}} + \frac{1}{K_{nl,p2}} & \text{for particle} - \text{particle contact} \\ \frac{1}{K_{nl,p}} + \frac{1}{K_{nl,b}} & \text{for particle} - \text{boundary contact} \end{cases}, \tag{6.4}$$

where subscripts 1 and 2 identify the two contacting particles. The individual stiffnesses associated to a particle and to a boundary are computed, respectively as:

$$K_{nl,p} = E_p L, \tag{6.5}$$

$$K_{nl,b} = E_b L, \tag{6.6}$$

where, E_p is the particle material's bulk Young's modulus, E_b is the boundary material's Young's modulus. L is the particle size.

The energy dissipation in the linear spring-dashpot model is viscous and due exclusively to the damping force term in Equation (6.3). The normal damping coefficient is defined in Rocky as follows:

$$C_n = 2\eta\sqrt{m^* K_{nl}}, \tag{6.7}$$

where η is the damping ratio; m^* is the effective or equivalent mass for the contact, defined as:

$$\frac{1}{m^*} = \begin{cases} \frac{1}{m_1} + \frac{1}{m_2} & \text{for particle} - \text{particle contact} \\ \frac{1}{m} & \text{for particle} - \text{boundary contact} \end{cases}, \tag{6.8}$$

where $m_1$and m_2 are the masses of the contacting particles; m is the mass of the particle in contact with a boundary.

The functional relationship between the damping ratio η and the coefficient of restitution ε, derived from that condition, is:

$$\varepsilon = \begin{cases} exp\left[-\frac{\eta}{\sqrt{1-\eta^2}}\left(\pi - arctan\frac{2\eta\sqrt{1-\eta^2}}{1-2\eta^2}\right)\right], & if\ 0 \ll \eta < \frac{1}{\sqrt{2}} \\ exp\left[-\frac{\eta}{\sqrt{1-\eta^2}} arctan\frac{2\eta\sqrt{1-\eta^2}}{2\eta^2-1}\right], & if\ \frac{1}{\sqrt{2}} \ll \eta \leq 1\,, \\ exp\left(-\frac{\eta}{\sqrt{\eta^2-1}} ln\frac{\eta+\sqrt{\eta^2-1}}{\eta-\sqrt{\eta^2-1}}\right), & if\ \eta > 1 \end{cases} \tag{6.9}$$

The tangential force in linear spring Coulomb limit model is elastic-frictional. If the tangential force were considered purely elastic, its value at time t would be given by:

$$F_{\tau,e}^{t} = F_{\tau}^{t-\Delta t} - K_{\tau}\Delta s_{\tau}, \tag{6.10}$$

where $F_{\tau}^{t-\Delta t}$ is the value of the tangential force at the previous time; Δs_{τ} is the tangential relative displacement of the particles during the timestep; K_{τ} is the tangential stiffness defined as:

$$K_{\tau} = r_K - K_{nl}, \tag{6.11}$$

where r_K is the tangential stiffness ratio, which defines the ratio of tangential contact stiffness to normal contact stiffness. This parameter controls the bulk Poisson's ratio of the granular materials. Here, we used the recommended value of 1.0.

However, the tangential force cannot exceed the Coulomb's limit. Thus, the complete expression for the tangential force is:

$$F_\tau^t = \min\left(\left|F_{\tau,e}^t\right|, \mu F_n^t\right) \frac{F_{\tau,e}^t}{\left|F_{\tau,e}^t\right|}, \tag{6.12}$$

where F_n^t is the normal contact force at time t, μ is the friction coefficient, defined as:

$$\mu = \begin{cases} \mu_s & \text{if no sliding taking palce at the contact} \\ \mu_d & \text{if sliding does take place at the contact'} \end{cases} \tag{6.13}$$

In which μ_s and μ_d are, respectively, the static and the dynamic friction coefficients.

Further, for the particle shape study, we have used the exact polyhedral shape in Rocky DEM. Hence, one does not need to input any rolling resistance parameter as the particle shape accurately accounts for the rolling behaviour making the calibration straightforward.

6.2. DEM model setup and validation

The irregular geometries of the grains were created from a practical method for generating irregularly shaped particles using a fractal dimension as a descriptor parameter of the grain morphology. It uses spherical harmonics that allow us to define and control the morphology of the particle from its fractal properties – its shape, roundness and texture– based on the model presented by Wei et al. (2018). The Spherical harmonic (SH) functions were used to generate stereolithography (STL) files for DEM simulations and experiments (3D printing grains). Different particle shapes were achieved by adjusting the fractal dimension (D_f) and D_2. The typical irregularly shaped particles used in this paper are shown in Figure 6.1.

The relative roughness (R_r) (Wei et al., 2021) serves as a particle shape descriptor, integrating D_f and D_2 to describe the effect of particle morphology on the deposit responses. Using the Parseval formula, the mean square distance (M_{SD}) between two SH surfaces with SH coefficients $c_{1,n}^m$ and $c_{2,n}^m$ can be computed (Gerig et al., 2001) as: $M_{SD} = \frac{1}{4\pi}\sum_{n=0}^{\infty}\sum_{m=-n}^{n}\left\|c_{1,n}^m - c_{2,n}^m\right\|^2$. Subsequently, the relative roughness (R_r), which quantifies how the irregular particle surface deviates globally from its c_0-determined sphere, can be defined based on $\sqrt{M_{SD}}$:

$$R_r = \frac{\sqrt{\frac{1}{4\pi}\sum_{n=1}^{n_{max}}\sum_{m=-n}^{n}\|c_n^m\|^2}}{c_0^0 \cdot Y_0^0(\theta,\varphi)} = \sqrt{\sum_{n=1}^{n_{max}}\left(D_2 \cdot \left(\frac{n}{2}\right)^{2D_f-6}\right)^2}. \tag{6.14}$$

The detailed determination of R_r is provided in Appendix. F. It has been confirmed that virtual and real particle shapes can exhibit nearly identical shape parameters (e.g., the difference between their mean values are all within 2%), as long as their corresponding D_2 and D_f are the same (Wei et al., 2018). Moreover, Figure F.5 illustrates the relationship between R_r and a wide range of D_2 and D_f

values, while Figure 5.1 shows the common granular materials characterized by R_r values less than 0.3. The relative roughness and traditional geometric characteristic parameters of the particles used for the simulation are summarized in Table 6-1.

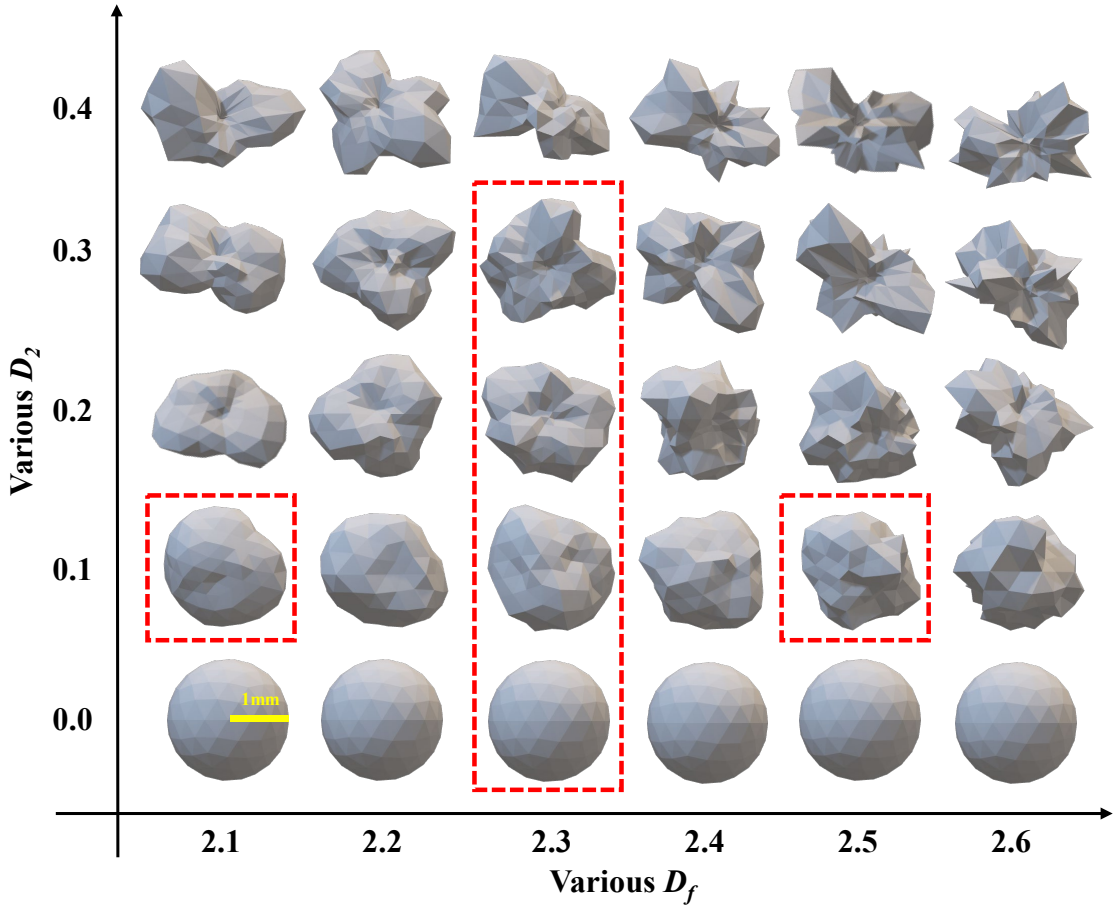

Figure 6.1 Typical particle shapes with varying D_f & D_2 (d ≈ 2mm). Each particle consists of 320 faces. Particles enclosed in the red dashed box are selected for numerical simulations.

Table 6-1 Values of particle geometric characteristic parameters

Type	R_r	Sphericity (S)	Particle aspect ratio (A_r)	Convexity (C_V)	Roundness (R)
Sphere	0	0.9961	1.0000	1.0000	0.9721
D_f=2.1, D_2=0.1	0.117	0.9498	0.8566	0.9781	0.8209
D_f=2.3, D_2=0.1	0.126	0.9222	0.8643	0.9423	0.7965
D_f=2.5, D_2=0.1	0.140	0.8587	0.8726	0.8621	0.7797
D_f=2.3, D_2=0.2	0.252	0.7966	0.7973	0.8072	0.7461
D_f=2.3, D_2=0.3	0.378	0.7004	0.7632	0.6998	0.7432

The DEM model configuration (see Figure 6.2) maintained a 1:1 ratio with the experimental box (see Figure 5.4). Particles enclosed in the red dashed box are selected for numerical simulations (see Figure 6.1). Particles were randomly generated using SH functions, and assemblies were achieved through a rainfall-style inlet with a uniform bulk density distribution. The packing density (0.62 - 0.67) closely matches the experimental measurements presented in Section 5.3. Notably, this approach also minimised local ordering and effectively prevented crystallization effects in the granular system. The initial length (L_0) of all column aspect ratios was set to 50mm. Different aspect ratios are achieved by adjusting the sample fill height. To eliminate the impact of other parameters besides particle shape, we ensured consistent material properties, filling processes, and sample geometry across all simulations. Based on the above setup, the effects of particle shape parameters on the deposit behaviour can be determined.

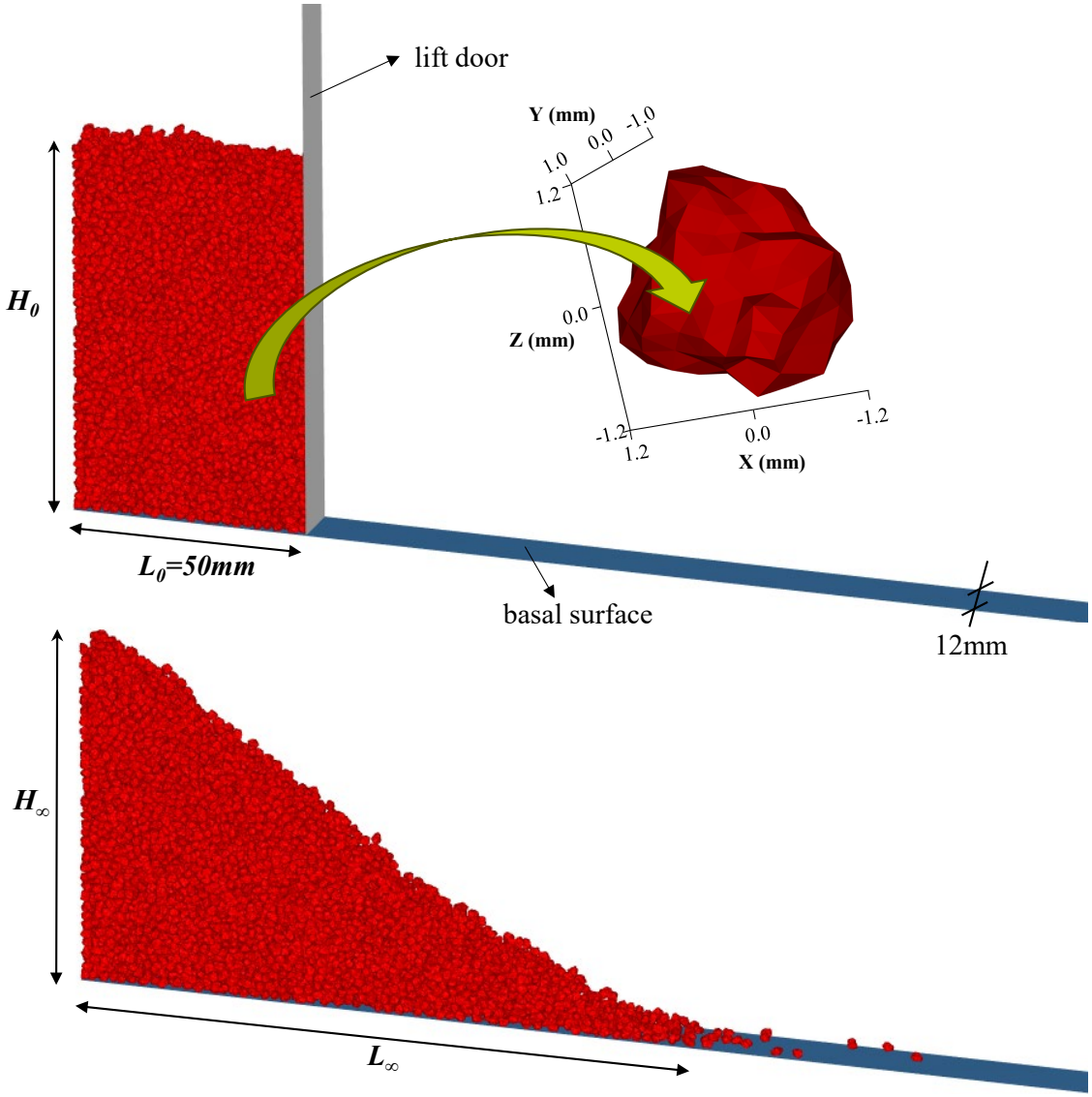

Figure 6.2 Sketch of the quasi-2D DEM collapse model (e.g., a = 1.6, D_f = 2.5 & D_2 = 0.1).

In the experiments, 1280 faces per particle were used. However, in DEM simulations, we employed an optimization strategy, reducing the number of faces per particle to 320. Before

implementing this optimization, we compared the effects of face number on particle shape parameters, as shown in Appendix. G. Reducing the number of faces per particle slightly modifies local contact geometry and roundness, but has little effect on other particle geometric parameters. However, since all DEM simulations employ the same discretization strategy, the comparative trends between particle shapes remain internally consistent. Hence, this reduction strategy preserved the fundamental phase characteristics of the particles while significantly improving computational efficiency.

As this study does not focus on any specific material, general values of the contact model parameters were found by trial and error using the run-out distance as calibration objective (Man et al., 2021a, Hoang and Nguyen, 2023) and are given in Table 6-2. Notably, since we used polyhedral shapes, no rolling resistance parameter was necessary. These experimental results were compared with the scaling relationship derived from DEM simulations (see Table 6-3). The deposit run-out distance exhibits an initial linear trend for lower aspect ratios. Our numerical models, considering different D_f while maintaining the same D_2, were compared to the experimental results (see Figure 6.3), with the corresponding slope values (C_α) provided in Table 6-3. It is evident that the run-out distance and final height of our numerical simulations are in good agreement with the experimental data. The deposit morphology further validates this consistency: the positional distribution of experimental points relative to the 45° line in the H^*- a parameter space conforms to the deposit regimes (see the inset of Figure 6.3b). Since the objective of the calibration was not to reproduce a specific material but to establish a self-consistent reference configuration, the calibrated parameters should be regarded as phenomenological. Internal fields (e.g., velocity, interlocking, and energy dissipation) are therefore interpreted comparatively, focusing on relative trends across different particle shapes under identical contact parameters.

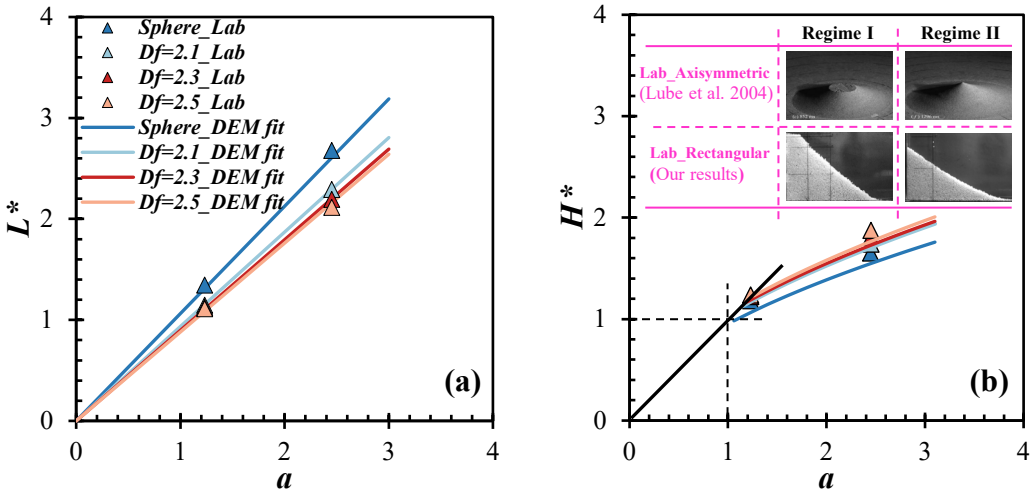

Figure 6.3 Validation of the DEM model with experimental results. (a) Run-out distance. The validation of numerical models with experimental results (see Figure 5.9(a)); (b) Final height. The inset illustrates the deposit regimes classified based on deposit morphology (see Section 3.5.3).

For each particle shape in Table 6-1, the collapses of two column aspect ratios 1.24 and 6 are simulated, which correspond to low and high columns, respectively. These simulations serve a dual purpose: to compare the effects of particle shape parameters on the two distinct flow regimes, and to facilitate detailed analyses of velocity fields, particle interlocking, and energy conversion. Additional simulations spanning a wider range of aspect ratios are conducted to establish scaling relationships.

Table 6-2 Values of contact model parameters used in the numerical investigations.

Parameter	Value
Timestep	1.44×10^{-6}
Bulk density (kg/m^3)	700
Young's modulus (N/m^2)	1×10^8
Coefficient of restitution ε	0.3
Static friction coefficient (particle-particle)	0.9
Dynamic friction coefficient (particle-particle)	0.9
Coefficient of friction (particle-wall)	0.4
Coefficient of rolling friction	None

6.3. Results and discussion

6.3.1. Deposit morphology

Figure 6.4(a) presents the deposit morphologies for particles of different shapes with a = 1.24. In accordance with the experimental findings in Section 5.4.1, deposits formed by particles exhibit two distinct regimes: Regime I and Regime II. The control group, consisting of spherical particles, exhibits characteristics of Regime II. For non-spherical particles, a transition from Regime II to Regime I is observed as D_f increases from 2.1 to 2.5 (with D_2 = 0.1) or as D_2 increases from 0.1 to 0.3 (with D_f = 2.3). This indicates that particle shape also affects the deposit regime. This transition corresponds to changes in the critical aspect ratio of final height (a_{CH}), which will be discussed in more detail in Table 6-3.

Figure 6.4(b) presents the deposit morphologies for different particle shapes with a = 6. The deposit morphology for all particle shapes exhibits the same morphology, identified as Regime II. The consistency is attributable to the different collapse mechanisms associated with varying aspect ratios, as discussed earlier. The inset of Figure 6.4 illustrates a reduction in the number of particles ejected and moving separately from the bulk flow as D_f or D_2 increases, which is corresponding to

higher R_r values. This observation indicates that particles with larger R_r values demonstrate higher rolling resistance, contributing to the overall stability of the sample.

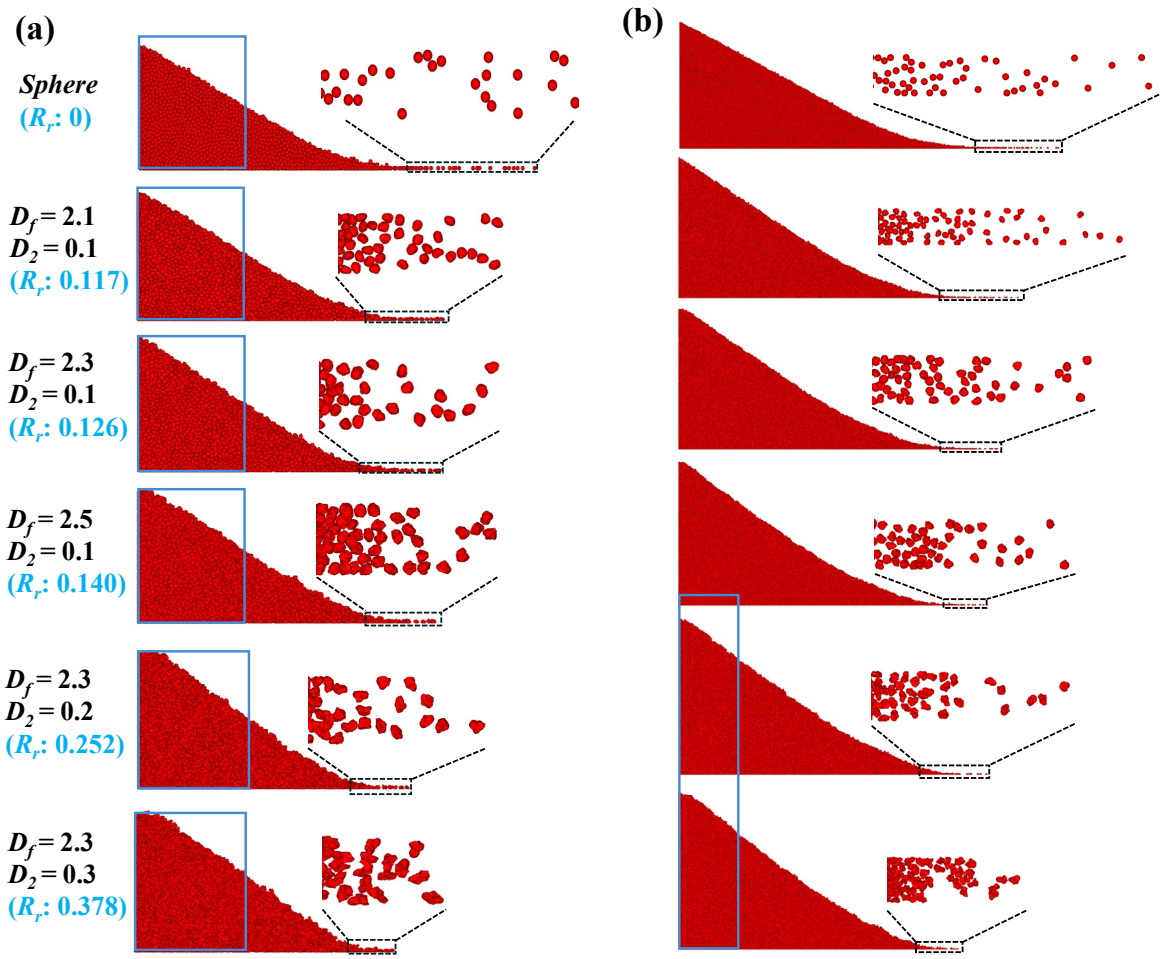

Figure 6.4 Final deposit morphology in a rectangular channel for typical aspect ratios under different particle shapes: (*a*) a = 1.24, (*b*) a = 6. The blue box represents the initial geometry. The main figure depicts the front view, while the inset shows the top view.

6.3.2. Generalizations of deposit run-out distance and final height

Figure 6.5(a) presents the relationship between the normalized run-out distance and aspect ratio for different particle shapes. Essentially, L^* decreases with increasing D_f, D_2, and R_r. The relationship can be divided into two stages: a linear increase stage for the lower columns (purple lines) and a power-law increase stage for higher columns (orange lines). Figure 6.5(b) illustrates the influence of particle shape on the relationship between the rescaled final height and aspect ratio. The final height increases with increasing D_f, D_2, and R_r, and similarly exhibits two distinct stages. Initially, a linear relationship with a slope of 1.0 is observed, regardless of particle shape, corresponding to the trapezoidal regime. However, when a exceeds approximately 1.0, the model can no longer maintain its initial height, and the deposit morphology transitions into the triangular regime. In this stage, the final height of spherical particles is lower than that of non-spherical

particles. Moreover, the final height tends to converge as aspect ratio increases, reflecting the competing effects of particle shape and aspect ratio.

To capture these trends, a quantitative analysis was conducted based on the Equations (2.1), (2.2), and (2.3). The critical aspect ratio and scaling constants for different particle shapes were derived from regression analysis (see Table 6-3). The effects of D_f, D_2, and R_r on these scaling constants were further examined through simple linear regression. Figure 6.5(c) shows that D_f has a limited influence on the scaling constants. In contrast, Figure 6.5(d) indicates that the critical aspect ratio a_{CL} increases with increasing D_2. The coefficients C_α and C_β, corresponding to the linear and power-law stages, respectively, decrease as D_2 increases. The coefficient C_γ exhibits a strong linear increase with D_2 ($R^2 = 0.96$). Similarly, R_r shows trends comparable to those of D_2 but with higher R^2 values (see Figure 6.5(e)). As R_r increases, both a_{CL} and C_γ increase, whereas C_α and C_β decrease. Additionally, the power coefficient c_{EL} increases slightly with D_f and more pronouncedly with D_2. The critical aspect ratio a_{CH} increases with increasing D_f, D_2 or R_r. The coefficient c_{EH} shows no clear relationship with D_f but decreases with increasing D_2, as reflected by the slope of the coloured triangles in Figure 6.5(b). Overall, the results suggest that the scaling constants are only weakly affected by D_f but are strongly influenced by D_2 and R_r. In general, the deposit geometry is significantly affected by particle shape.

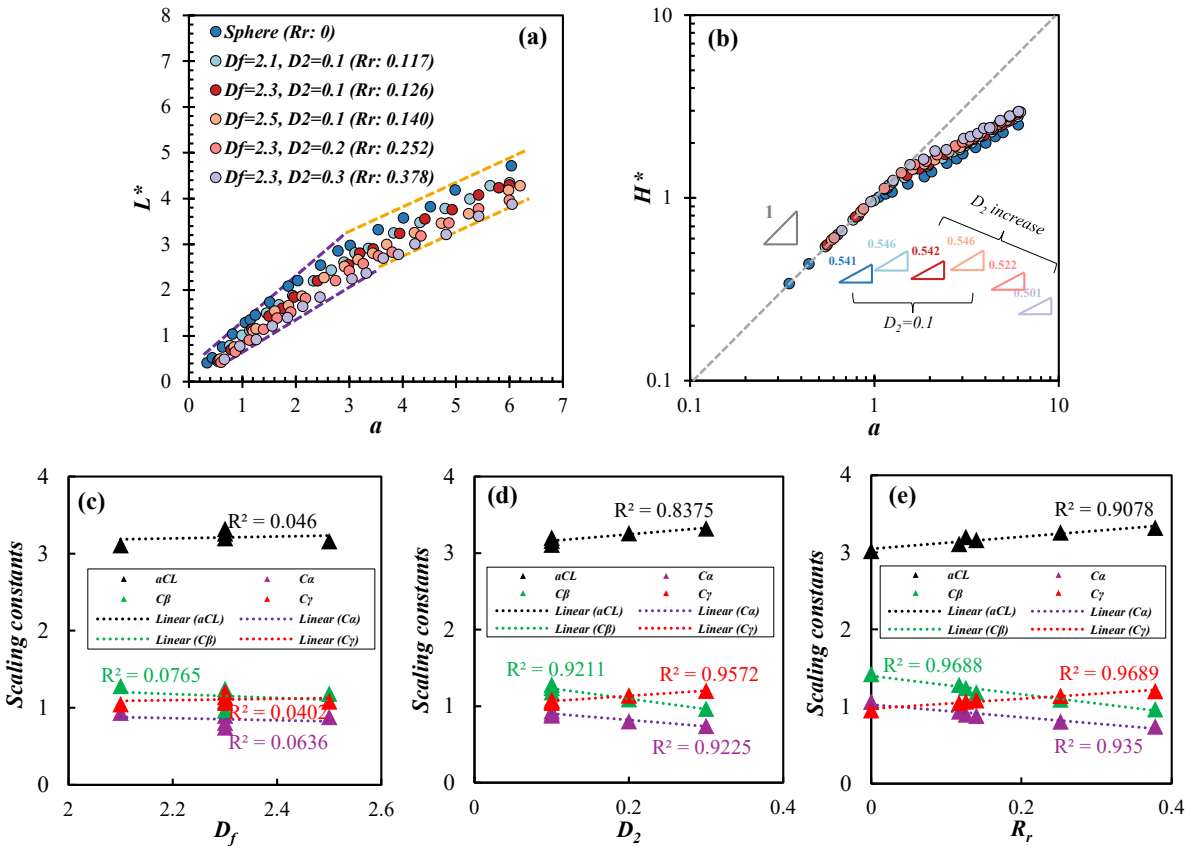

Figure 6.5 The effect of different particle shapes on the deposit geometry under various aspect ratios. (a) The normalized run-out distance L^*. The purple line represents a harmonized correction for the linear stage (approx. a < 3), while the orange line depicts the power-

law description (approx. $a \geq 3$). (b) The rescaled final height H^*. The grey triangle symbolizes the slope for all particle shapes at $a < 1$, and the other coloured triangles symbols represent the slope of the line for all particle shapes at $a \geq 1$. (c) Relationship between D_f and scaling constants. (d) Relationship between D_2 and scaling constants. (e) Relationship between R_r and scaling constants.

Table 6-3 Summary of critical column aspect ratio and scaling constants ($R^2 > 0.99$)

Type	R_r	a_{CL}	C_α	C_β	c_{EL}	a_{CH}	C_γ	c_{EH}
Sphere	0	3.02	1.063	1.421	0.667	1.06	0.953	0.541
D_f=2.1, D_2=0.1	0.117	3.11	0.935	1.281	0.688	1.14	1.046	0.546
D_f=2.3, D_2=0.1	0.126	3.20	0.897	1.242	0.698	1.18	1.064	0.542
D_f=2.5, D_2=0.1	0.140	3.16	0.880	1.182	0.700	1.26	1.082	0.546
D_f=2.3, D_2=0.2	0.252	3.26	0.805	1.090	0.728	1.40	1.140	0.522
D_f=2.3, D_2=0.3	0.378	3.32	0.743	0.966	0.776	1.56	1.201	0.501

6.3.3. Spatial velocity field

The particle velocity fields at the start of the collapse clarifies how particle shape affects initial movement and reflects the sample stability. Figure 6.6(a) illustrates the effect of varying shaped particles on the spatial distribution of translational velocity at lower columns (e.g., $a = 1.24$). The collapse process is shown using a normalized time t^*, which is defined as the ratio of the time t divided by $\sqrt{H_0/g}$. The influence region of the translational velocity field occurs at the same location and exhibits a consistent pattern. As particle shape becomes more irregular (ie., with increasing D_f or D_2), the influence region size decreases notably. Moreover, the influence region shows a continuous decrease with increasing R_r, indicating that samples with higher R_r values correspond to greater overall stability. Figure 6.6(b) shows a similar trend for the rotational velocity profiles: as D_f, D_2 or R_r increase, the rotational velocity of particles is constrained. The maximum rotational velocity occurs at the lowest point of the lift door surface, where the flow front experiences the earliest forward displacement. Analysis of the translational and rotational velocity profiles reveals that column failure initiates through a diagonal failure surface. This observation aligns with the Coulomb-type failure angle reported by Lai et al. (2023) and highlights the influence of particle shape.

For higher columns (e.g., $a = 6.0$), the translational velocity distribution shows limited dependence on D_f but remains sensitive to D_2, as shown in Figure 6.6(c). Compared with cases of lower aspect ratios, the failure pattern changes notably: the failure surface includes a sloping segment near the column base that transitions into a quasi-vertical surface above, and a larger proportion of the total material participates in the failure process. This shift in the velocity distribution reflects a change in the collapse mechanism: friction dominates in lower columns, while the pressure gradient

governs the collapse in higher cases. Furthermore, in the case of spherical particles, the affected region of rotational velocity spans nearly the entire specimen. However, as D_2 increases, the influence region decreases significantly, as shown in Figure 6.6(d), indicating that higher D_2 values enhance the stability of the sample. In contrast, D_f exerts only a minor influence on the rotational velocity profiles. Moreover, consistent with the flow patterns of lower columns presented in Figure 5.6, specimens with higher D_f exhibit greater overall stability, and the influence region continuously increases as R_r decreases.

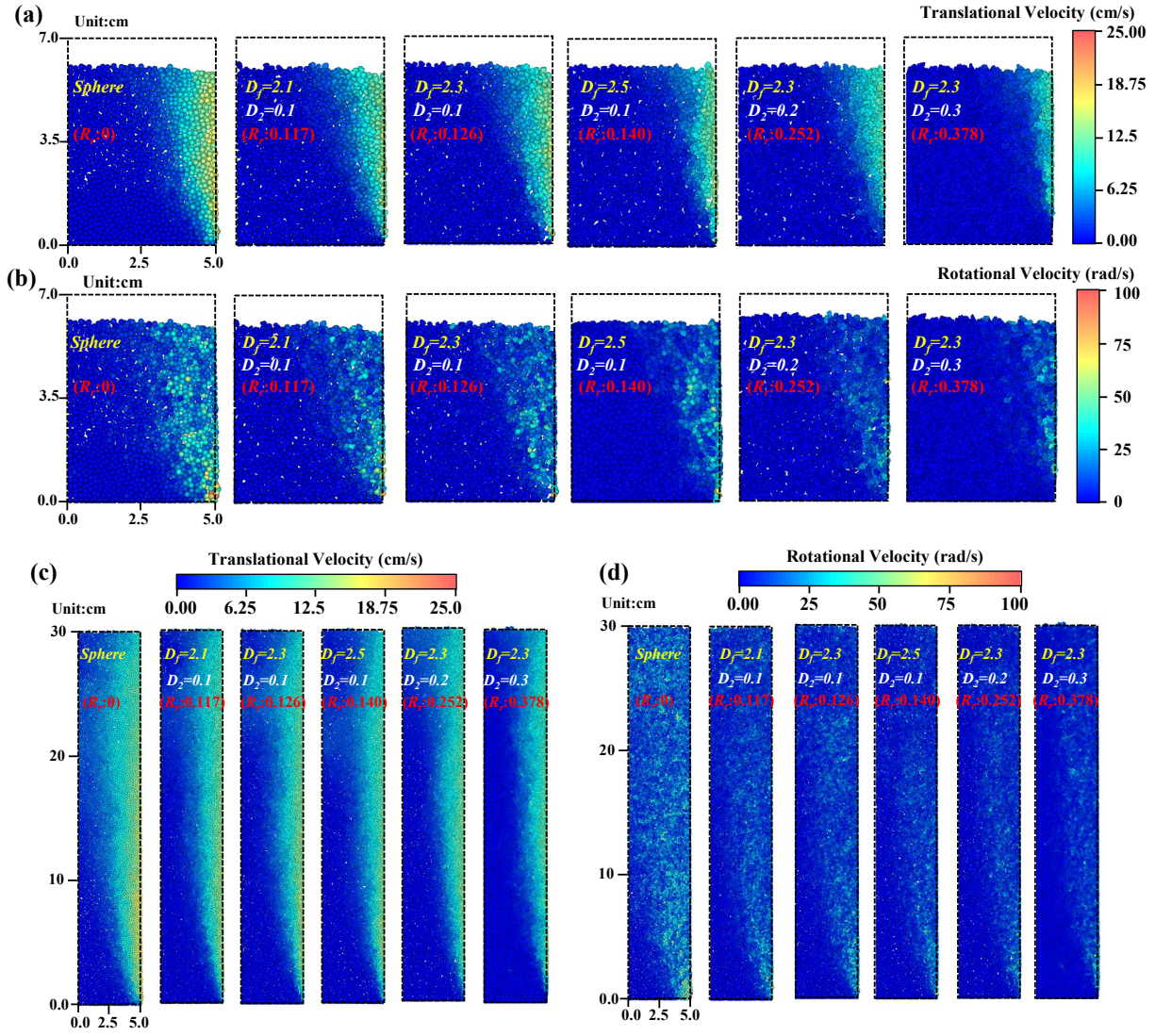

Figure 6.6 Spatial distribution of the velocity of rectangular channel collapse under different particle shapes. (a) Translational velocity and (b) Rotational velocity for a = 1.24 at t^* = 0.252. (c) Translational velocity and (d) Rotational velocity for a = 6 at t^* = 0.114. The pictures display an internal cross-section.

6.3.4. Evaluation of the interlocking effects

The interlocking effect between particles has been extensively studied to analyse the influence of particle shape on collapse, particularly in terms of particle surface contact characteristics. Azema

and Radjai (2012) proposed a friction mobilisation index, denoted as $I_M = |F_T|/\mu F_N$, which represents the ratio of tangential forces F_T to the anti-sliding force μF_N, to investigate the properties of friction mobilization. In this study, we propose a new average index (I_{AM}) that allows us to evaluate the interlocking effect at any given moment by comparing the forces to the reference case of spherical particles where no interlocking occurs. The formulation of I_{AM}, is hence normalized with respect to spherical shape and presented in Equation (6.15). This index is calculated based on the average tangential and normal forces across all inter-particle contacts at each moment. A larger value of I_{AM} corresponds to a higher interlocking effect. It should be though noted that I_{AM} quantifies friction mobilization and interlocking rather than frictional energy dissipation, as high mobilization does not necessarily imply sustained sliding.

$$I_{AM} = \frac{\frac{F_{T_{ave(i)}}}{\mu_p \cdot F_{N_{ave(i)}}} - \frac{F_{T_{ave(Sphere)}}}{\mu_p \cdot F_{N_{ave(Sphere)}}}}{\frac{F_{T_{ave(Sphere)}}}{\mu_p \cdot F_{N_{ave(Sphere)}}}}, \tag{6.15}$$

where $F_{T_{ave}}$ is the average tangential contact force and $F_{N_{ave}}$ is the average normal contact force of the whole sample at the same moment. μ_p is the inter-particle contact friction coefficient.

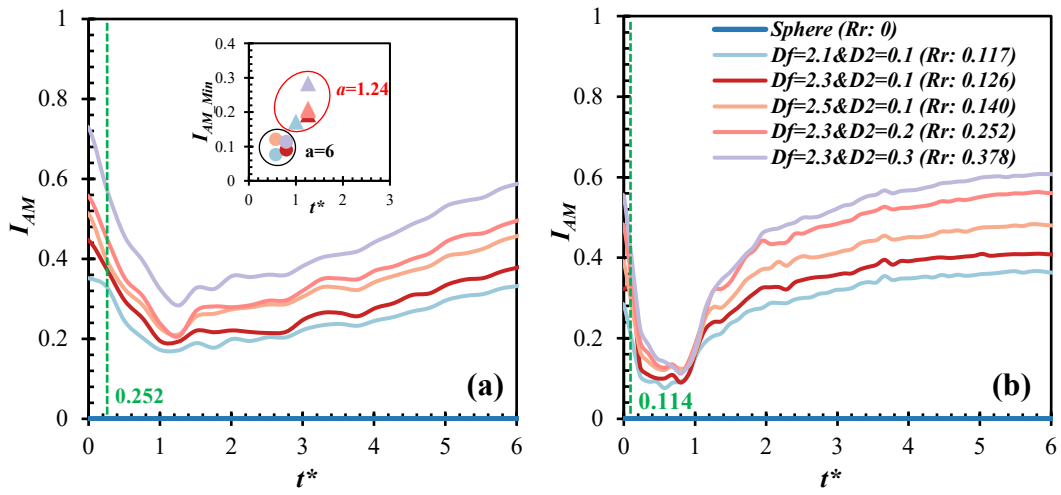

Figure 6.7 Evolution of average friction mobilization (I_{AM}) with different particle shapes. (a) a = 1.24. (b) a = 6. The inset shows the peak values of I_{AM}.

Figure 6.7 presents the evolution of I_{AM} under various particle shapes. During the collapse process, I_{AM} increases with increasing D_f or D_2, corresponding to higher R_r values and indicating a stronger interlocking capability. The evolution of I_{AM} also aligns well with the observed flow patterns (see Figure 5.6). Specifically, in the early stage of collapse (e.g., $t = \tau_c$), the rapid decrease of I_{AM} corresponds to the transition of particles from a compact state to a loose state during gravity-driven collapse. This transition reveals clearly visible voids within the sample, directly reflecting a significant reduction in interparticle contacts. We also find that the variation in the initial I_{AM} value (see green dashed lines in Figure 6.7) aligns with the spatial velocity field results (see Figure 6.6). After reaching its minimum, the subsequent gradual increase in I_{AM} reflects the completion of the

collapse process. This overall trend is also influenced by the aspect ratio: the rates of decrease and increase, as well as the minimum I_{AM} values in lower columns (e.g., a = 1.24, Figure 6.7(a)), are considerably smaller than those in higher columns (e.g., a = 6, Figure 6.7(b)). Furthermore, at a = 6, the minimum I_{AM} values for different particle shapes are similar and occur nearly simultaneously as D_f or D_2 increases (see inset of Figure 6.7(a)). These differences may be attributed to variations in the collapse mode: in lower columns, collapse occurs primarily through sliding, whereas in higher columns it proceeds via avalanching. Overall, these findings confirm that particle shape exerts a significant influence on the interlocking behaviour of granular flow.

6.3.5. Energy conversion analysis

We discuss the granular flow behaviour during collapse in terms of the energy balance of the granular system:

$$E_{DA} = E_0 - E_P - E_K \tag{6.16}$$

$$E_K = \sum_{i=1}^{N} m_i g h_i \tag{6.17}$$

$$E_{KT} = \sum_{i=1}^{N} \frac{1}{2} m_i {v_i}^2 \tag{6.18}$$

$$E_{KR} = \sum_{i=1}^{N} \frac{1}{2} I_i \omega_i^2 \tag{6.19}$$

where E_0 is the total work of the system, that equals the initial potential energy, E_P is the potential energy, with m being the mass of each particle, h denoting the height of the particle's centroid; g the acceleration of gravity, and N the total number of particles. E_{KT} denotes the translational kinetic energy, while E_{KR} represents the rotational kinetic energy. v_i and ω_i denote the translational and angular velocities of each particle, and I is polar moment of inertia of the particle. The dissipated energy E_{DA} includes both frictional dissipations induced by sliding contacts and viscous damping losses originating from the contact model. Due to the low restitution coefficient used in this study (ε = 0.3), viscous damping can account for a substantial fraction of the total dissipated energy, particularly during the early stages of collapse. Consequently, the magnitude of total dissipation primarily reflects the amount of kinetic energy generated during collapse rather than the intrinsic strength of dissipative contacts. This choice is intentional and provides a conservative setting for assessing particle-shape effects, as geometric interlocking and shape-induced constraints must persist even when velocity fluctuations are strongly damped. Accordingly, internal energy fields are interpreted comparatively across particle shapes under identical contact parameters rather than as absolute material properties.

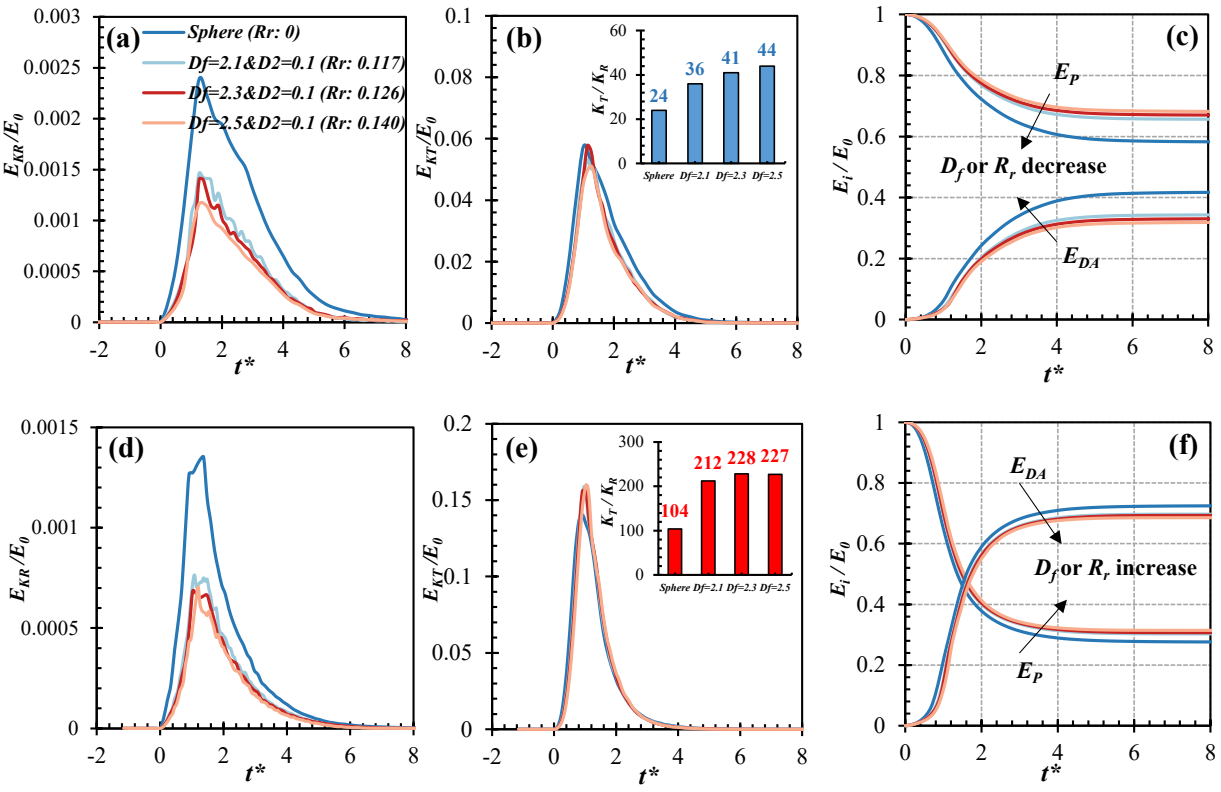

Figure 6.8 Effects of D_f on the evolution of normalized energy terms with respect to characteristic time for rectangular channel collapse with (a)-(c) a = 1.24 and (d)-(f) a = 6. The inset figures in (b) and (e) illustrate the ratio of maximum E_{KT} to maximum E_{KR}.

Figure 6.8 presents the typical evolution of the energy terms normalized with E_0, hereafter denoted by E_P^*, E_{DA}^*, and E_K^*, for both low (a = 1.24) and high (a = 6) columns under varying D_f values. Assuming particles are rigid bodies, translational and rotational components are orthogonal and separate as distinct terms of total kinetic energy. Spherical particles exhibit a maximum E_{KR}^* approximately twice that of non-spherical particles (see Figure 6.8(a) and Figure 6.8(d)). In terms of the evolution of kinetic energy during collapse, for a = 1.24, E_{KR}^* decreases with increasing D_f (see Figure 6.8(a)), consistent with the evolution of interlocking capacity (see Figure 6.7) and indicating that a larger D_f restricts particle rotation during collapse. However, this effect is weaker for a = 6 (see Figure 6.8(d)). To quantify the impact of D_f on kinetic energy, the ratio of maximum E_{KT}^* to maximum E_{KR}^* was calculated. For a = 1.24, this ratio rises from 36 to 44 as D_f increases from 2.1 to 2.5 (see inset of Figure 6.8(b)), whereas for a = 6, it exceeds 200 with no clear trend (see inset of Figure 6.8(e)). In both cases, E_{KT}^* consistently surpasses E_{KR}^*, suggesting that the contribution of rotational kinetic energy (E_{KR}^*) to the system dynamics is negligible relative to translational kinetic energy (E_{KT}^*), in agreement with the findings of Torres-Serra et al. (2021). This finding agrees with Kermani et al. (2015), who used a rotational resistance factor to represent particle shape effects and observed that higher rotational resistance reduces energy dissipation. In contrast, E_{DA}^* is strongly influenced by the aspect ratio. For a = 6, its value is almost twice that for a = 1.24 (see Figure 6.8(c) and Figure 6.8(f)), likely reflecting the dominant role of pressure

gradients in the collapse of higher columns – where more potential energy is converted into dissipative energy (corresponding to larger run-out distance and relative particle velocities), and particle shape effects become less significant. This is further supported by the observation that the final E_{DA}^* decreases only slightly (from 69.7% to 68.6%) as D_f increases from 2.1 to 2.5 (see Figure 6.8(f)). We also found that non-spherical particles dissipate less total energy, with the normalized dissipated energy showing only weak dependence on D_f. This reduction does not indicate weaker dissipative contacts. Instead, enhanced interlocking and geometric constraints reduce particle velocities and suppress kinetic energy generation during collapse. As a result, less energy is available to be dissipated overall, despite comparable or stronger contact-level resistance.

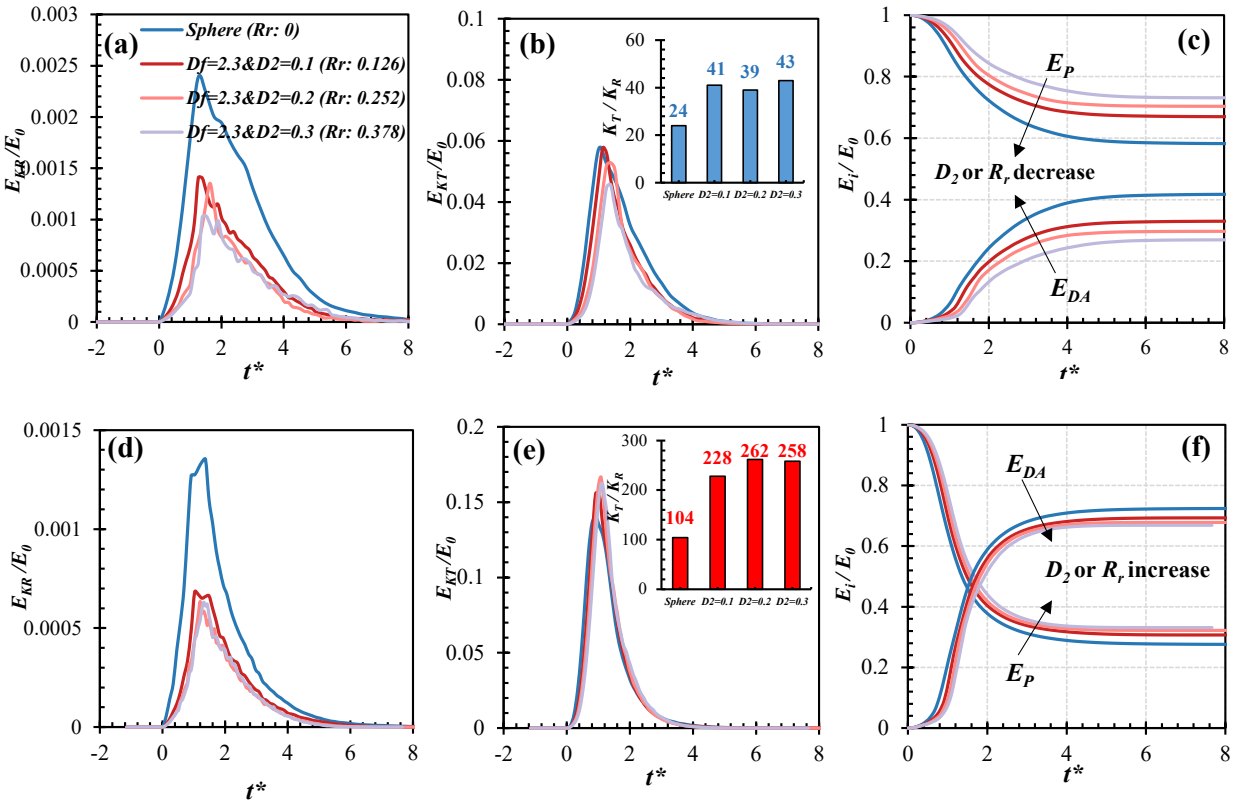

Figure 6.9 Effects of D_2 on the evolution of normalized energy terms with respect to characteristic time for rectangular channel collapse with (a)-(c) a = 1.24 and (d)-(f) a = 6. The inset figures in (b) and (e) present the ratio of maximum E_{KT} to maximum E_{KR}.

Figure 6.9 presents the evolution of normalized energy terms, denoted as E_P^*, E_{DA}^*, and E_K^*, for low (a = 1.24) and high (a = 6) columns under various D_2. For a = 1.24, the maximum E_{KR}^* or E_{KT}^* decrease as D_2 increases (see Figure 6.9(a)), indicating that larger D_2 restricts both particle rotational and transitional velocity during collapse. However, this influence is less pronounced for a = 6 (see Figure 6.9(d)) because the collapse mechanism is different, as already mentioned. Our results confirm that translational kinetic energy contributes more substantially to the system's dynamics than rotational kinetic energy (see the insets of Figure 6.9(b) and (e)). Figure 6.9(c) shows that the dissipated energy (E_{DA}^*) decreases significantly from 33.1% to 26.9% as D_2 increases from 0.1 to 0.3 – a reduction of 6.2%. In contrast, the corresponding decrease in E_{DA}^* due

to a change in D_f is only 2.5%. This suggests that D_2 has a more pronounced influence than D_f on energy dissipation in shorter columns. A similar trend is observed for $a = 6$: as D_2 increases from 0.1 to 0.3, E_{DA}^* decreases from 69.3% to 66.9%, a reduction of 2.4% (see Figure 6.9(f)), which remains greater than the 1.1% decrease associated with changes in D_f (see Figure 6.8(f)). We also find that D_2 drives particle shape changes more significantly than D_f (i.e., larger R_r variations), and these R_r variations subsequently lead to energy differences. These results highlight the competitive mechanisms of particle shape and aspect ratio on energy dissipation: larger aspect ratios lead to higher E_{DA}^* values and diminish the influence of particle shape on the overall energy conversion process. This may explain the observations in earlier works that did not observe an influence of shape.

Notably, particle-shape effects on collapse behaviour remain evident from the energy analysis despite the strongly inelastic regime, indicating that geometric interlocking and shape-induced constraints act independently of the specific dissipation mechanism.

6.3.6. Relation to traditional particle geometric characteristics

6.3.6.1. Deposit run-out distance

Hoang and Nguyen (2023) claimed that no clear relationship exists between sphericity and granular flow response. However, their two types of shape particles, elongated and flattened, did not have equivalent volumes. By controlling the particles volume, we were able to quantify the effect of particle geometric parameters on deposit geometry with a greater control. Our findings indicate that normalized run-out distance (L^*) increases with sphericity, ranging from 0.7 to 1.0, across varying aspect ratios (see Figure 6.10(a)). Excluding spherical particles, which exhibit the largest L^*, we observed that L^* increases with increasing particle aspect ratio (A_r) until reaching a peak at $A_r = 0.855$, corresponding to particles of $D_f = 0.1$ & $D_2 = 0.1$ (see Figure 6.10(b)). Beyond this peak, L^* decreases as A_r increases. Notably, particles of $D_f = 0.1$ & $D_2 = 0.1$ demonstrate the maximum packing density. Previous studies (e.g., Meng et al. (2012)) have reported that peak packing densities occur when A_r falls within the range of 0.5 to 1. While peaking density is often considered to influence the run-out distance, this relationship is complex and influenced by multiple factors, including the material characteristics (e.g., particle size, shape), the nature and intensity of external forces (e.g., gravity, stress history), as well as topographical and geomorphological conditions. Interestingly, our results reveal that even particles of $D_f = 0.1$ & $D_2 = 0.1$, which exhibit the highest packing density, result in the largest run-out distance. This finding suggests that collapse behaviour is not dominated by packing density, which is consistent with the findings of Kermani et al. (2015). On the contrary, particles with $D_f = 0.1$ & $D_2 = 0.1$ have a special particle shape with low interlocking ability, as shown in Figure 6.7. This observation suggests that the particle aspect ratio (A_r), as one of the particle geometric parameters, plays a significant role in the collapse mechanism. Moreover, L^* increases with increasing convexity and roundness as shown in Figure 6.10(c) & (d).

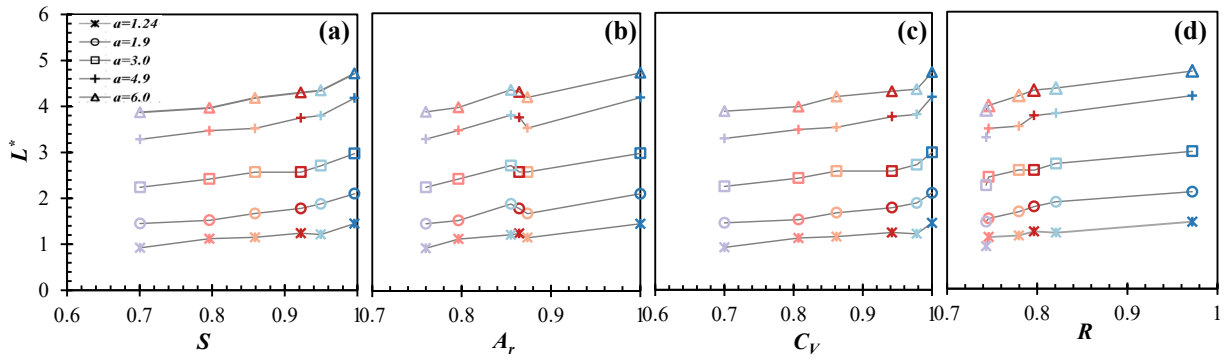

Figure 6.10 Particle geometric parameters effect on the normalized run-out distance. (a) Sphericity. (b) Particle aspect ratio. (c) Convexity. (d) Roundness.

6.3.6.2. Flow mobility

The modified mobility angle θ' (refer to Figure 4.8) was employed to investigate the effect of particle shape on flow mobility. A smaller θ' corresponds to greater flow mobility during an avalanche event. The results demonstrate that flow mobility improves with increasing sphericity, convexity, and roundness (see Figure 6.11(a), (c), and (d)). Among them, the influence of roundness on flow mobility is interpreted in a comparative sense, rather than as an absolute measure of rolling resistance. In contrast, the impact of particle aspect ratio (A_r) on flow mobility exhibits a more complex pattern (see Figure 6.11(b)). This complexity likely arises from the interplay between particle shape and particle movement mechanisms. Particles primarily move through translation accompanied by contact interactions involving sliding and interlocking, as inferred from the combined energy and interlocking analyses. For $A_r < 0.855$, corresponding to particles with D_2 decreases from 0.3 to 0.1 and $D_f = 2.3$, the reduced interlocking ability (see Figure 6.7) enhances flow mobility (θ' decreases). Additionally, the increase in transitional energy with decreasing D_f (see Figure 6.9(b)) further supports this trend. Notably, at $A_r = 0.855$, a local peak in θ' is observed, corresponding to particles of $D_f = 0.1$ & $D_2 = 0.1$, which exhibit lower interlocking ability (see Figure 6.7). This shape shows higher energy dissipation then the others, except for sphere (see Figure 6.8 and Figure 6.9), and may provide an optimal balance rolling and sliding modes, facilitating more effective collapse propagation. For $0.855 < A_r < 1$, corresponding to D_f increases from 2.1 to 2.5 with $D_2 = 0.1$, particles become more spherical but not yet perfect spheres. The interlocking effects may increase (see Figure 6.7), limiting rolling motion and flow mobility (θ' decreases). At $A_r = 1$, full spherical particles exhibit the highest rotational energy (see Figure 6.8(a) and Figure 6.9(a)) and transitional energy (see Figure 6.8(b) and Figure 6.9(b)) and exhibit the lowest interlocking ability (see Figure 6.7), resulting in the highest flow mobility.

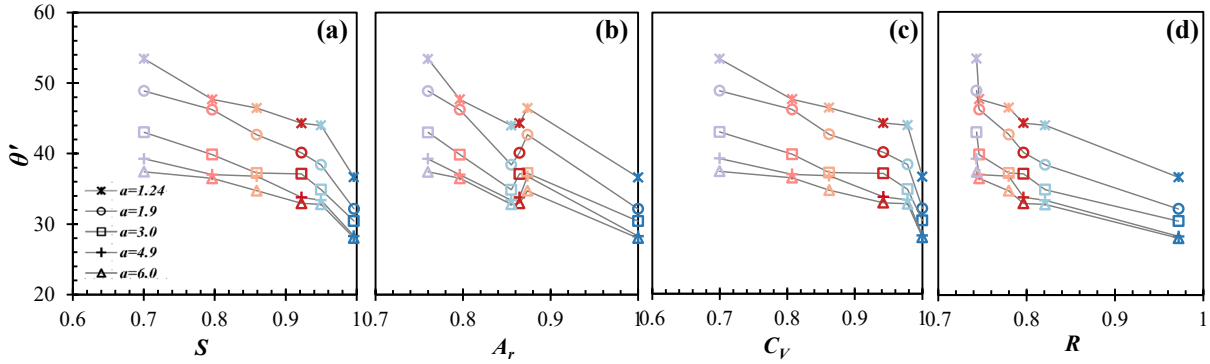

Figure 6.11 Particle geometric parameters effect on the flow mobility. (a) Sphericity. (b) Particle aspect ratio. (c) Convexity. (d) Roundness.

6.3.7. New normalized run-out distance (*L**) including particle shape

In previous studies, the prediction of run-out distance has mainly relied on the calibration of formula coefficients to match collapse results based on various material properties (e.g., repose angle, friction of angle, and elastic modulus, etc.). To the best of our knowledge, no study has used particle shape parameters to predict the run-out distance. Referring to the scaling law analysis in Section 6.3.2, we propose a simple model to predict the run-out distance that considers particle shape effects. The relative roughness (R_r) is introduced as a new shape parameter to quantify this influence and improve the interpretation of the results. The proposed model follows the expressions shown in Equations (2.1) and (2.2) and is expressed in Equation (6.20).

$$L^* = \begin{cases} c'_\alpha(R_r) \cdot a, & a < a_{CL} \\ c'_\beta(R_r) \cdot a^{c'_{EL}}, & a \geq a_{CL} \end{cases}. \tag{6.20}$$

Considering the numerical results and literature results (see Table 2-1), the index coefficient c'_{EL} should be a value close to 0.7. Our numerical simulations show a clear trend: as particle shape deviates from spherical and becomes more irregular (i.e., higher R_r), the run-out distance tends to decrease. The model must also ensure that when $R_r = 0$ (representing spherical shape), it corresponds to the maximum run-out distance. By applying dimensionless and regression analysis, we then derive Equation (6.21).

$$L^* = \begin{cases} \left(\frac{a_1}{e^{b_1 \cdot R_r}} + c_1\right) \cdot a, & a < a_{CL} \\ \left(\frac{a_2}{e^{b_2 \cdot R_r}} + c_2\right) \cdot a^{0.7}, & a \geq a_{CL} \end{cases}. \tag{6.21}$$

where, a_1, b_1, and c_1 are coefficients for the linear increase stage. a_2, b_2, and c_2 are coefficients for the power increase stage.

To guarantee the continuity of both sides of Equation (6-21), a_{CL} should satisfy the following form:

$$a_{CL} = \left(\frac{c'_\beta(R_r)}{c'_\alpha(R_r)}\right)^{10/3} = \left(\frac{\frac{a_2}{e^{b_2 \cdot R_r}} + c_2}{\frac{a_1}{e^{b_1 \cdot R_r}} + c_1}\right)^{10/3}. \quad (6.22)$$

By fitting the relationships between L^* and $c'_\alpha(R_r)$, and between L^* and $c'_\beta(R_r)$ in Equation (6.20), the values of c'_α, c'_β and R_r were quantified and are summarized in Tables 6-4 and 6-5, with R^2 = 0.99. Using these relationships, the coefficients in Equation (6.21) were subsequently derived. The fitting parameters are obtained as follows: we obtained the following fitting parameters: $a_1 = 0.3192, b_1 = 3.8581,$ and $c_1 = 0.6806$ for the linear increase stage, with R^2 = 0.98; and $a_2 = 1.3634, b_2 = 0.6707,$ and $c_2 = 0$ for the power increase stage, with R^2 = 0.94. The fitted coefficients $C_\alpha^{'}$ and $C_\beta^{'}$ show a good functional fit with R_r, as shown in Figure 6.12. Consequently, the final model was derived and presented in Equation (6.23). This model shows good agreement with numerical and experimental results, as shown in Figure 6.13. Specifically, for particles with lower R_r, the run-out distance is only slightly affected by particle shape. This also explains why Lube et al. (2004) concluded that particle shape has no influence on the collapse response, as the natural grains used in their experiments had similar or lower R_r. In contrast, for particles with higher R_r, the normalized run-out distance decreases markedly with increasing R_r.

Table 6-4 Fitting results for aspect ratio $a < a_{CL}$.

R_r	C'_α	R^2
0.00000	0.9981	0.946
0.11709	0.9038	0.981
0.12593	0.8782	0.988
0.13947	0.8473	0.983
0.25212	0.8003	0.996
0.37819	0.7564	0.991

Table 6-5 Fitting results for aspect ratio $a \geq a_{CL}$.

R_r	C'_β	C'_{EL}	R^2
0.00000	1.3905	0.7	0.956
0.11709	1.2704	0.7	0.985

0.12593	1.2449	0.7	0.993
0.13947	1.1971	0.7	0.984
0.25212	1.1411	0.7	0.992
0.37819	1.0842	0.7	0.987

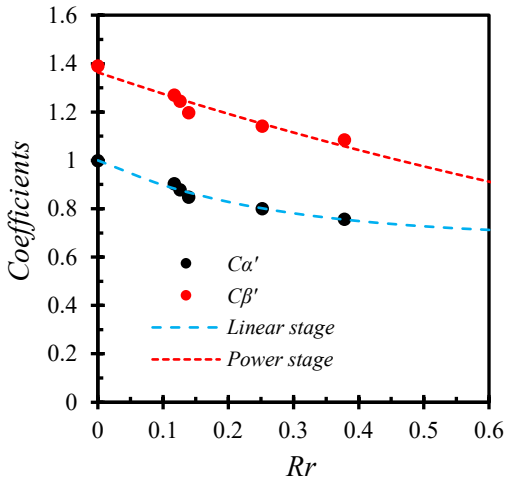

Figure 6.12 The fitted coefficients C'_α and C'_β as explicit functions of R_r.

$$L^* = \begin{cases} \left(\frac{0.3192}{e^{3.8581 \cdot R_r}} + 0.6806\right) \cdot a, & a < a_{CL} \\ \left(\frac{1.3634}{e^{0.6707 \cdot R_r}}\right) \cdot a^{0.7}, & a \geq a_{CL} \end{cases} . \tag{6.23}$$

$$a_{CL} = \left(\frac{\frac{1.3634}{e^{0.6707 \cdot R_r}}}{\frac{0.3192}{e^{3.8581 \cdot R_r}} + 0.6806} \right)^{10/3} .$$

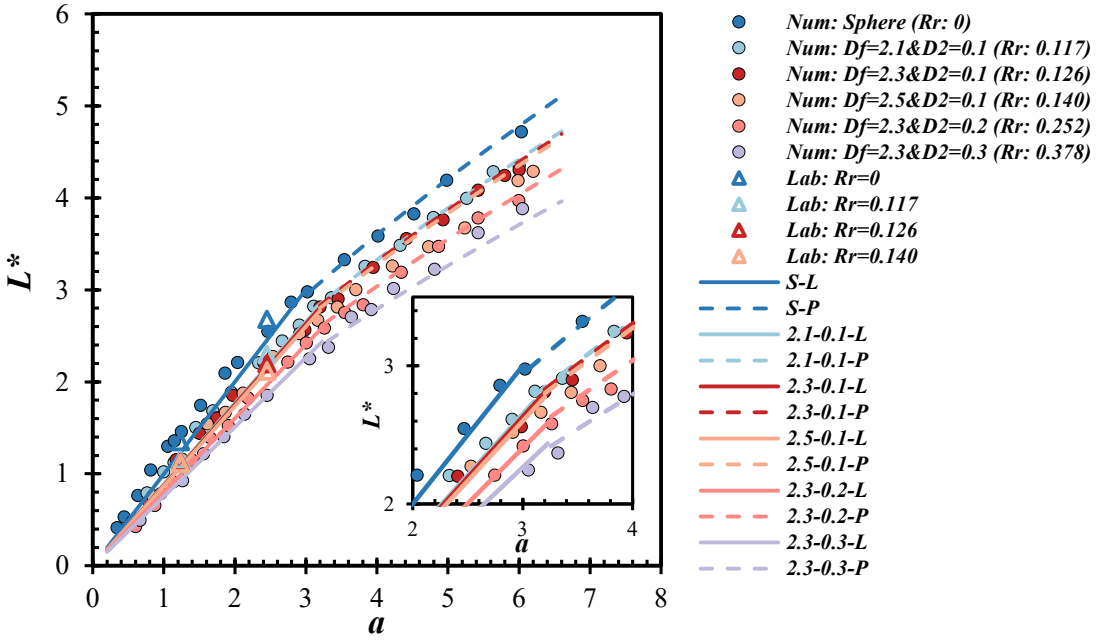

Figure 6.13 Comparison of prediction equations and numerical results of the normalized run-out distance L^* for various particle shapes. Coloured lines fitted according to Equation (6.23).

6.4. Conclusion

In this chapter, spherical harmonic (SH) functions were employed to reconstruct 3D particles with specific shape parameters, which were then integrated into DEM simulations to investigate the effect of particle shape on collapse behaviour. The main findings are summarized as follows:

(1) Particle shape plays a critical role in controlling the collapse behaviour of granular materials. It influences not only the deposit morphology - such as the transition from trapezoidal to the triangular deposit regimes (I to II) and the enhancement of overall sample stability (a reduction in the number of particles ejected and moving separately from the bulk flow) - but also key scaling relationships, including the run-out distance, final height, and the scaling constants (e.g., a_{CL}, a_{CH}, C_α C_β, and C_γ).

(2) The particle shape affects initial velocity fields during collapse. In lower columns, increasing R_r, D_f or D_2 reduces the spatial extent of particle velocity influence. However, in higher columns, the translational velocity field becomes less sensitive to D_f but remains responsive to variations in D_2.

(3) An average friction mobilisation index (I_{AM}) was proposed to evaluate the interlocking effect during collapse. I_{AM} is influenced by both particle shape and the aspect ratio, with the influence of particle shapes on the overall interlocking effect diminishes at larger aspect ratios.

(4) Energy analysis shows that rotational kinetic energy is much smaller than translational kinetic energy, but spherical particles have about twice rotational kinetic energy compared to irregular

ones. Non-spherical particles dissipate less energy compared to spherical ones in the absence of heat considerations. Additionally, larger aspect ratios lead to higher dissipated energy and diminish the influence of particle shape on the overall energy conversion process. The observed energy dissipation trends correspond to a strongly inelastic collapse regime in which viscous contact damping plays a major role alongside frictional effects. Nevertheless, relative differences between particle shapes remain robust under identical contact parameters, indicating that the reported shape effects are conservative and not artefacts of the chosen dissipation regime.

(5) The relationship between traditional particle geometric characteristics and deposit geometry was analysed. L^* increases with higher particle sphericity, convexity, and roundness. In contrast, as the particle aspect ratio increases, L^* initially increases - while flow mobility θ' decreases - until reaching a peak point at $A_r = 0.855$. Beyond this threshold, L^* continue to increase as A_r increases. The flow mobility exhibits a similar trend and this trend is associated with the interlocking ability of different particle shapes.

(6) We proposed a new model to predict run-out distance based on particle shape parameter, relative roughness (R_r). For particles with lower R_r, L^* is only slightly influenced. In contrast, for particles with higher R_r, L^* decreases significantly as R_r increases. These findings provide valuable insights for predicting collapse response in granular materials with varying particle shapes.

7 Discussion

7.1. Interrelation of the three factors mentioned above

The experimental studies conducted by the groups of Huppert and Lajeunesse constitute milestone contributions to the understanding of granular column collapse. Their work opened new avenues for exploring collapse behaviour and underlying mechanisms, with relevance to both natural processes and industrial applications.

In Huppert's experiments, sand flows were examined on three types of substrates: a smooth wooden plane, a smooth transparent Perspex plane, and a rough plane made of sandpaper. The roughness of the sandpaper was of the order of the mean particle size of the granular materials. Additional experiments were performed using couscous, rice, and sugar on both a smooth wooden plane and a smooth baize surface in order to explore the influence of interparticle friction across grains of different geometrical shapes (Figure 7.1 and Table 7-1). Huppert and co-workers claimed that all the results were independent of both the grain type and the surface over which the grains flowed. However, their study remained largely qualitative, and the influence of particle shape could not be isolated from other parameters (e.g., particle density, particle size). As shown in Figure 7.1 and Table 7-2, the different grains exhibit substantial variations in size and angle of repose, complicating the interpretation of interactions between particles and substrate surfaces.

Lajeunesse's group addressed some of these limitations by using glass beads of different sizes in granular column collapse experiments performed on different substrate surfaces and over a range of aspect ratios. Their approach isolated the effect of particle shape; however, basal friction was still not quantified. They observed that, at small aspect ratios, the deposit profiles obtained on rough and smooth substrates match relatively well as illustrated by the truncated cone geometries in Figure. 7-2(a). As the aspect ratio increased, the deposits formed on smooth substrates became progressively more distinct from those on rough substrates (Figures. 7-2(b) and 7-2(c)).

Despite these advances, a critical review of the literature reveals that several key issues remain unresolved. Previous experimental studies have provided valuable qualitative insights, yet they generally lack quantitative assessments of crucial factors such as substrate roughness, particle shape, and gravitational effects. Addressing these gaps is essential for achieving a more comprehensive understanding of granular collapse behaviour.

First, the absence of a quantitative treatment of substrate roughness motivated the work presented in Chapter 3 (Basal Friction), in which identical granular materials were used in combination with systematically varied basal friction in order to quantify this influence on deposit responses. Second, the lack of a rigorous analysis of particle shape led us to adopt SH functions to reconstruct three-dimensional particles with controlled shape parameters, which were then implemented in DEM

simulations to investigate shape effects on collapse behaviour in Chapters 5 and 6 (Particle Shape). While basal friction characterises the boundary conditions and particle shape represents an intrinsic grain property, comparing their respective roles in energy dissipation provides an integrated framework for understanding collapse dynamics. In particular, angular or elongated particles can effectively mimic increased basal friction through enhanced interlocking.

Furthermore, Lube and co-workers proposed a model to predict collapse time as a function of two key parameters: sample size (radius and height) and gravitational acceleration (g). Although the influence of sample size was experimentally validated, the role of gravity was not directly tested. Building on the findings of Chapter 3, we extended this framework in Chapter 4 (gravity level) by prescribing a fixed basal friction while varying gravitational acceleration, thereby enabling a quantitative assessment of gravity effects on deposit behaviour. This work offers potential applications for planetary and exoplanetary research.

In summary, by systematically addressing the limitations of previous studies, we have developed a more comprehensive and quantitative understanding of how these uncertainties influence the collapse behaviour of granular materials.

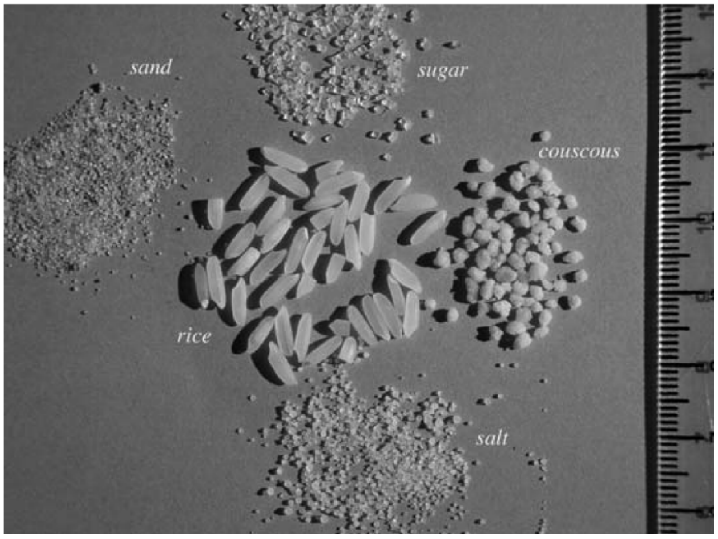

Figure 7.1 Photo of the five different grains used in the experiments (Lube et al., 2004).

Table 7-1 Properties of particles used in the experiments (Lube et al., 2004).

Particle	Mean density (g cm^{-3})	Mean grain size (mm)	Angle of repose (deg.)
Sand	2.6	0.32	30
Salt	2.16	0.30	30
Couscous	1.39	2	34
Rice	1.46	7×2	31
Sugar	1.58	1	35

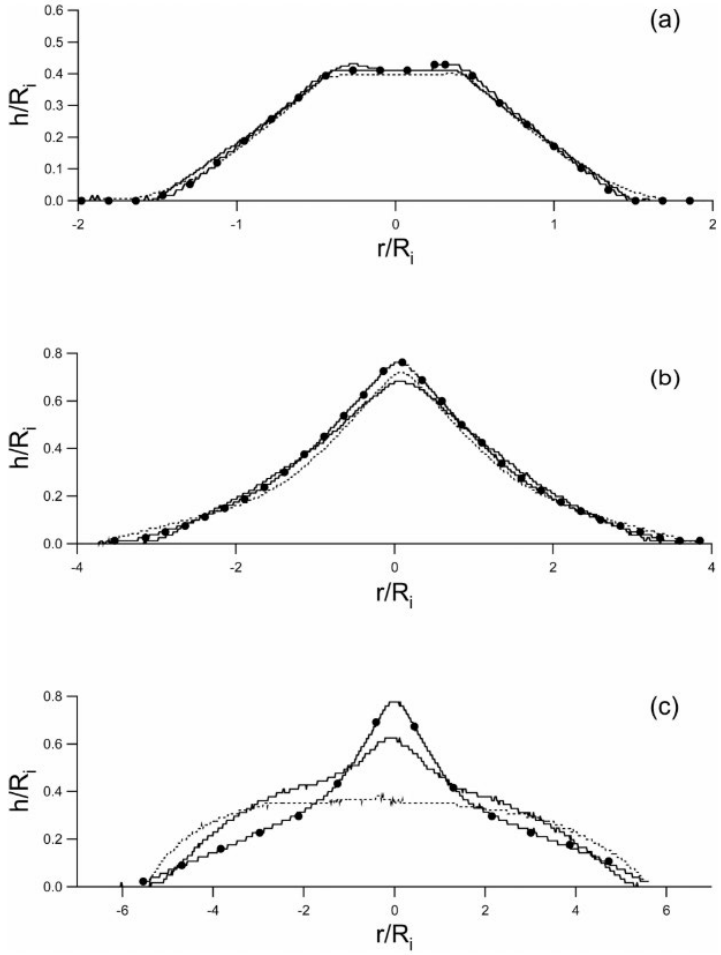

Figure 7.2 Deposit profiles normalized to the tube radius. (a) a=0.41. Plain line with circles: Series 1, M = 50g, Ri =28mm. Dotted line: Series 3, M = 700g, Ri =70.5mm. Plain line: Series 4, M = 700g, Ri =70.5mm. (b) a=1.95. Plain line with circles: Series 1, M = 600g, Ri =40mm. Dotted line: Series 3, M = 600g, Ri =40mm. Plain line: Series 4, M = 600g, Ri =40mm. (c) a=6.2. Plain line with circles: Series 1, M = 675g, Ri =28mm. Dotted line: Series 3, M = 675g, Ri =28mm. Plain line: Series 4, M = 675g, Ri =28mm. Series 1-4 are presented in Table 7-2.

Table 7-2 Characteristics of the different series of experiments (Lajeunesse et al., 2004).

Seriese	d (μm)	Substrate
1	350 ± 50	Sandpaper of roughness λ≈ 540μm
2	350 ± 50	Erodible bed (same granular material of thickness 4 or 12mm)
3	350 ± 50	Smooth wooden surface
4	1150 ± 150	Sandpaper of roughness λ≈ 540μm

7.2. Limitations

In this work, we conducted a systematic investigation of three fundamental factors — basal friction, gravity, and particle shape — in granular material collapse phenomenon. This study clarifies the relative importance of each factor, an aspect that has not been comprehensively addressed in previous studies. However, several limitations remain, as outlined below:

(1) Basal friction. Our simulations use simplified or idealized boundary conditions that may not fully represent the complexity of natural ground surfaces. Moreover, only a single material type was considered, and while a predictive relationship was proposed as a preliminary guideline, further improvement is required for engineering applications. For example, a comparative summary table would greatly enhance its practical utility.

(2) Gravity level. The role of gravity was systematically analysed; however, real planetary environments may involve additional processes, such as particle cohesion or atmospheric interactions, which were not considered in this study.

(3) Particle shape. The particle-shape analysis was restricted to a limited set of shape descriptors. Although this yielded meaningful insights, natural grains are often highly irregular and require more sophisticated characterization methods. Our study did not encompass a sufficiently broad range of shapes, particularly for particles with sphericity values below 0.7.

(4) Coupling effects. Each factor was investigated largely in isolation. In natural systems, however, basal friction, gravity, and particle shape act simultaneously and interactively. Developing a unified framework capable of capturing these coupled effects would substantially enhance both the predictive capability and the practical relevance of granular materials collapse models.

8 Conclusion and Outlook

8.1. Conclusion

8.1.1. The effect of basal friction on the granular column collapse

(1) To predict the run-out distance, we propose a modified formula ($R^* = \alpha \cdot a^{\beta}$) that incorporates the basal friction coefficient μ. This model accounts for two extreme conditions: $\mu = 0$ and $\mu \to \infty$.

(2) The basal friction influences the final height. Specifically, an increase in the friction coefficient shifts the separation point (maximum final height) between the growth and decline stages, resulting in an increase in the aspect ratio corresponding to the maximum final height. However, this effect converges when $\mu > 0.5$.

(3) The basal friction also affects the deposit regime. The competition mechanism between the initial column aspect ratio and basal friction coefficient reveals two transition zones that delimit the three main deposit regimes reported in the literature.

(4) The energy conversion analysis also confirms the critical aspect ratios at $a = 1.7$ as transition from a friction-dominated to pressure gradient dominated flow. Additionally, it confirms that for values $a \sim 10$ (affected by the friction coefficient, μ), a regime transition exists that explains the different deposit morphologies.

(5) The effect of basal friction on the front kinetic energy was investigated. Results show that R^* decreases with increasing E_K^U, further indicating that pressure gradients govern collapse in high columns.

8.1.2. The effect of gravity level on the granular column collapse

(1) Higher gravity levels significantly shorten the collapse time of granular columns while maintaining similar deposit morphologies. This indicates that gravity strongly influences collapse dynamics but has no impact on the deposit morphology.

(2) To accurately predict the collapse time of a granular column, two models were proposed, both exhibiting a positive correlation with $1/\sqrt{g}$, following a scaling of $n^{-1/2}$. The non-dimensional collapse time (t_∞/τ_c) was found to vary with the initial aspect ratio, rather than remaining constant.

(3) Gravity levels appear to have minimal effect on deposit run-out distance and final height. The expected scaling of 1.0 is clearly observed, suggesting that gravity level does not affect the

normalized run-out distance. This conclusion aligns with observations of natural landslides in the Solar System. Moreover, the gravity level does not alter the critical aspect ratio (a = 1.7), where a shift occurs in the bilinear relationship.

(4) Flow mobility was used to quantitatively describe the effect of gravity levels on deposit results. A modified mobility angle (θ') was proposed to eliminate the effect of the initial geometry (r_0).

(5) Multiscale studies show good agreement between small-scale results (e.g., experiments) and large-scale results (e.g., landslide). Under identical scaling conditions (e.g., identical density, length, etc.), collapse extent is independent of gravity but depends on sample volume and initial potential energy. The sample volume factor exhibits a clear scale effect, with a critical point near a = 1.7.

8.1.3. The effect of particle shape on the granular materials collapse

(1) Particle shape plays a critical role in controlling the collapse behaviour of granular materials. It influences not only the deposit morphology - such as the transition from trapezoidal to the triangular deposit regimes (I to II) and the enhancement of overall sample stability (a reduction in the number of particles ejected and moving separately from the bulk flow) - but also key scaling relationships, including the run-out distance, final height, and the scaling constants.

(2) The particle shape affects initial velocity fields during collapse. In lower columns, increasing R_r, D_f or D_2 reduces the spatial extent of particle velocity influence. However, in higher columns, the translational velocity field becomes less sensitive to D_f but remains responsive to variations in D_2.

(3) An average friction mobilisation index (I_{AM}) was proposed to evaluate the interlocking effect during collapse. I_{AM} is influenced by both particle shape and the aspect ratio, with the influence of particle shapes on the overall interlocking effect diminishes at larger aspect ratios.

(4) Energy analysis shows that non-spherical particles dissipate less energy compared to spherical ones in the absence of heat considerations. Additionally, the energy conversion is significantly affected by aspect ratio and R_r.

(5) We quantitively analyse the relationship between traditional particle geometric characteristics (Sphericity, Convexity, Roundness, and Particle aspect ratio) on the deposit run-out distance and flow mobility.

(6) We proposed a new model to predict run-out distance based on the particle shape parameter, relative roughness (R_r). For particles with lower R_r, L^* is only slightly influenced. In contrast, for particles with higher R_r, L^* decreases significantly as R_r increases.

8.2. Outlook

(1) This study has focused exclusively on the influence of particle shape in quasi-2D collapse scenarios. Future work should extend to fully three-dimensional samples and capture the complete dynamic processes.

(2) Potential practical applications include improved hazard prediction for landslides and debris flows, as well as more realistic modelling of regolith dynamics in extraterrestrial environments.

(3) A comprehensive understanding of collapse mechanisms requires the integration of multiple factors rather than the consideration of a single parameter. Future research should therefore address coupled processes (e.g., friction and shape under variable gravity), incorporate fluid phases, and include validation through large-scale laboratory or field experiments.

(4) To advance towards a more holistic understanding of collapse mechanisms, further investigations should examine the collapse behaviour of particle assemblies with mixed size and shapes. Such studies would clarify the relative importance of individual particle shape parameters and their combined effects on the collapse process. In addition, the introduction of an overarching irregularity parameter could provide a robust framework for simulating and predicting real-world landslide scenarios with enhanced fidelity and accuracy.

Bibliography

ADAMIDIS, O., ALBER, S. & ANASTASOPOULOS, I. 2020. Assessment of Three-Dimensional Printing of Granular Media for Geotechnical Applications. *Geotechnical Testing Journal,* 43**,** 641-659.

ALBABA, A., LAMBERT, S., NICOT, F. & CHAREYRE, B. 2015. Relation between microstructure and loading applied by a granular flow to a rigid wall using DEM modeling. *Granular Matter,* 17**,** 603-616.

ALEXANDER KIRILLOV, ERIC MINTUN, NIKHILA RAVI, HANZI MAO, CHLOE ROLLAND, LAURA GUSTAFSON, TETE XIAO, SPENCER WHITEHEAD, ALEXANDER C. BERG, WAN-YEN LO, PIOTR DOLLAR & GIRSHICK, R. 2023. Segment Anything. *Proceedings of the IEEE/CVF International Conference on Computer Vision (ICCV)***,** 4015-4026.

ARNDT, T., BRUCKS, A., OTTINO, J. M. & LUEPTOW, R. M. 2006. Creeping granular motion under variable gravity levels. *Phys Rev E Stat Nonlin Soft Matter Phys,* 74**,** 031307.

ASKEY, R. 2005. The 1839 paper on permutations: its relation to the Rodrigues formula and further developments. *Mathematics and Social Utopias in France: Olinde Rodrigues and His Times,* 28**,** 105-118.

ATWOOD‐STONE, C. & MCEWEN, A. S. 2013. Avalanche slope angles in low‐gravity environments from active Martian sand dunes. *Geophysical Research Letters,* 40**,** 2929-2934.

AZEMA, E. & RADJAI, F. 2012. Force chains and contact network topology in sheared packings of elongated particles. *Phys Rev E Stat Nonlin Soft Matter Phys,* 85**,** 031303.

BALMFORTH, N. J. & KERSWELL, R. R. 2005. Granular collapse in two dimensions. *Journal of Fluid Mechanics,* 538.

BEAKAWI AL-HASHEMI, H. M. & BAGHABRA AL-AMOUDI, O. S. 2018. A review on the angle of repose of granular materials. *Powder Technology,* 330**,** 397-417.

BOWMAN, E. T., LAUE, J., IMRE, B. & SPRINGMAN, S. M. 2010. Experimental modelling of debris flow behaviour using a geotechnical centrifuge. *Canadian Geotechnical Journal,* 47**,** 742-762.

BUI, H. H. & NGUYEN, G. D. 2021. Smoothed particle hydrodynamics (SPH) and its applications in geomechanics: From solid fracture to granular behaviour and multiphase flows in porous media. *Computers and Geotechnics,* 138.

BUI, H. H., SAKO, K. & FUKAGAWA, R. 2007. Numerical simulation of soil–water interaction using smoothed particle hydrodynamics (SPH) method. *Journal of Terramechanics,* 44**,** 339-346.

CABRERA, M. & ESTRADA, N. 2019. Granular column collapse: Analysis of grain-size effects. *Phys Rev E,* 99**,** 012905.

CABRERA, M. & ESTRADA, N. 2021. Is the Grain Size Distribution a Key Parameter for Explaining the Long Runout of Granular Avalanches? *Journal of Geophysical Research: Solid Earth,* 126.

CABRERA, M. A., LEONARDI, A. & PENG, C. 2020. Granular flow simulation in a centrifugal acceleration field. *Géotechnique,* 70**,** 894-905.

CABRERA, M. A. & WU, W. 2017. Experimental modelling of free-surface dry granular flows under a centrifugal acceleration field. *Granular Matter,* 19.

CAGNOLI, B. & PIERSANTI, A. 2015. Grain size and flow volume effects on granular flow mobility in numerical simulations: 3‐D discrete element modeling of flows of angular rock fragments. *Journal of Geophysical Research: Solid Earth,* 120**,** 2350-2366.

CHEN, W. & QIU, T. 2012. Numerical Simulations for Large Deformation of Granular Materials Using Smoothed Particle Hydrodynamics Method. *International Journal of Geomechanics,* 12**,** 127-135.

CLEARY & FRANK 2006a. Thee-Dimensional Discrete Element Simulation of Axi-symmetric Collapses of Granular Columns. *Teachnical report***,** 44710.

CLEARY, P. W. & FRANK, M. 2006b. Three-Dimensional Discrete Element Simulation of Axi-symmetric Collapses of Granular Columns. *Engineering Computations*.

CROSTA, G. B., IMPOSIMATO, S. & RODDEMAN, D. 2009. Numerical modeling of 2-D granular step collapse on erodible and nonerodible surface. *Journal of Geophysical Research,* 114.

CUNDALL, P. A. & STRACK, O. D. L. 1979. A discrete numerical model for granular assemblies. *Géotechnique,* 29**,** 47-65.

DONG, L. 2023. Energy consumption analysis of the granular run-out process: effect of particle shape and slope angle. *Natural Hazards,* 117**,** 1673-1687.

DORBOLO, S., MAQUET, L., BRANDENBOURGER, M., LUDEWIG, F., LUMAY, G., CAPS, H., VANDEWALLE, N., RONDIA, S., MÉLARD, M., VAN LOON, J., DOWSON, A. & VINCENT-BONNIEU, S. 2013. Influence of the gravity on the discharge of a silo. *Granular Matter,* 15**,** 263-273.

FÁVERO, N., ALOMIR H. & BORJA, R. I. 2018. Continuum hydrodynamics of dry granular flows employing multiplicative elastoplasticity. *Acta Geotechnica,* 13**,** 1027-1040.

FERN, E. J. & SOGA, K. 2016. The role of constitutive models in MPM simulations of granular column collapses. *Acta Geotechnica,* 11**,** 659-678.

FRANK, C. 2006. Three-Dimensional Discrete Element Simulation of Axi-symmetric Collapses of Granular Columns. *Engineering Computations*.

GALINDO-TORRES, S. A. & PEDROSO, D. M. 2010. Molecular dynamics simulations of complex-shaped particles using Voronoi-based spheropolyhedra. *Phys Rev E Stat Nonlin Soft Matter Phys,* 81**,** 061303.

GERIG, G., STYNER, M., JONES, D., WEINBERGER, D. & LIEBERMAN, J. Shape analysis of brain ventricles using spharm. Proceedings IEEE workshop on mathematical methods in biomedical image analysis (MMBIA 2001), 2001. IEEE, 171-178.

GOUJON, C., THOMAS, N. & DALLOZ-DUBRUJEAUD, B. 2003. Monodisperse dry granular flows on inclined planes: role of roughness. *Eur Phys J E Soft Matter,* 11**,** 147-57.

GUE., C. S., BOLTON., K. S. M. & THUSYANTHAN., N. I. 2010. Centrifuge modelling of submarine landslide flows. *In: Physical Modelling in Geotechnics-Proceedings of the 7th International Conference on Physical Modelling in Geotechnics, ICPMG 2010,* 2**,** 1113-1118.

HALLQUIST, J. O. 2006. LS-DYNA® Theory Manual. Livermore Software Technology Corporation, Livermore, California.

HANAOR, D. A., GHADIRI, M., CHRZANOWSKI, W. & GAN, Y. 2014. Scalable surface area characterization by electrokinetic analysis of complex anion adsorption. *Langmuir,* 30**,** 15143-52.

HANAOR, D. A. H., GAN, Y., REVAY, M., AIREY, D. W. & EINAV, I. 2016. 3D printable geomaterials. *Géotechnique,* 66**,** 323-332.

HOANG, U. T. & NGUYEN, N. H. T. 2023. Particle shape effects on granular column collapse using superquadric DEM. *Powder Technology,* 424.

HOFMEISTER, P. G., BLUM, J. & HEIELMANN, D. 2009. The flow of granular matter under reduced-gravity conditions. *American Institute of Physics,* 1145**,** 71-74.

J.J.MONAGHAN 1994. Simulating Free Surface Flows with SPH. *Journal of Computational Physics,* 110**,** 399-406.

JING, L., KWOK, C. Y., LEUNG, Y. F., ZHANG, Z. & DAI, L. 2018a. Runout Scaling and Deposit Morphology of Rapid Mudflows. *Journal of Geophysical Research: Earth Surface,* 123**,** 2004-2023.

JING, L., YANG, G. C., KWOK, C. Y. & SOBRAL, Y. D. 2018b. Dynamics and scaling laws of underwater granular collapse with varying aspect ratios. *Physical Review E,* 98.

KERMANI, E. & QIU, T. 2018a. Simulation of Quasi-Static and Dynamic Collapses of Rectangular Granular Columns Using Smoothed Particle Hydrodynamics Method. *International Journal of Geomechanics,* 18.

KERMANI, E. & QIU, T. 2018b. Simulation of quasi-static axisymmetric collapse of granular columns using smoothed particle hydrodynamics and discrete element methods. *Acta Geotechnica,* 15**,** 423-437.

KERMANI, E., QIU, T. & LI, T. 2015. Simulation of Collapse of Granular Columns Using the Discrete Element Method. *International Journal of Geomechanics,* 15.

KLEINHANS, M. G., MARKIES, H., DE VET, S. J., IN 'T VELD, A. C. & POSTEMA, F. N. 2011. Static and dynamic angles of repose in loose granular materials under reduced gravity. *Journal of Geophysical Research,* 116.

LACAZE., L., JEREMY C, P. & RICH R, K. 2008. Planar collapse of a granular column: Experiments and discrete element simulations. *Physics of Fluids,* 20.

LAI, Z., JIANG, E., ZHAO, L., WANG, Z., WANG, Y. & LI, J. 2023. Granular column collapse: Analysis of inter-particle friction effects. *Powder Technology,* 415.

LAI, Z., VALLEJO, L. E., ZHOU, W., MA, G., ESPITIA, J. M., CAICEDO, B. & CHANG, X. 2017. Collapse of Granular Columns With Fractal Particle Size Distribution: Implications for Understanding the Role of Small Particles in Granular Flows. *Geophysical Research Letters,* 44.

LAJEUNESSE, E., MANGENEY-CASTELNAU, A. & VILOTTE, J. P. 2004. Spreading of a granular mass on a horizontal plane. *Physics of Fluids,* 16**,** 2371-2381.

LAJEUNESSE, E., MONNIER, J. B. & HOMSY, G. M. 2005. Granular slumping on a horizontal surface. *Physics of Fluids,* 17**,** 103302.

LAJEUNESSE, E., QUANTIN, C., ALLEMAND, P. & DELACOURT, C. 2006. New insights on the runout of large landslides in the Valles‐Marineris canyons, Mars. *Geophysical Research Letters,* 33.

LI, Y., WEI, D., ZHANG, N. & FUENTES, R. 2024. Effect of basal friction on granular column collapse. *Granular Matter,* 26.

LINERO, S., FITYUS, S., SIMMONS, J., LIZCANO, A. & CASSIDY, J. 2017. Trends in the evolution of particle morphology with size in colluvial deposits overlying channel iron deposits. *EPJ Web of Conferences,* 140.

LO, C. Y., BOLTON, M., CHENG, Y. P., NAKAGAWA, M. & LUDING, S. 2009. Discrete Element Simulation of Granular Column Collapse. *AIP Conference Proceedings.*

LUBE, G., HUPPERT, H. E., SPARKS, R. S. & FREUNDT, A. 2005. Collapses of two-dimensional granular columns. *Phys Rev E,* 72**,** 041301.

LUBE, G., HUPPERT, H. E., SPARKS, R. S. J. & HALLWORTH, M. A. 2004. Axisymmetric collapses of granular columns. *Journal of Fluid Mechanics,* 508**,** 175-199.

LUCAS, A., MANGENEY, A. & AMPUERO, J. P. 2014. Frictional velocity-weakening in landslides on Earth and on other planetary bodies. *Nat Commun,* 5**,** 3417.

LUCAS, A., MANGENEY, A., MÈGE, D. & BOUCHUT, F. 2011. Influence of the scar geometry on landslide dynamics and deposits: Application to Martian landslides. *Journal of Geophysical Research,* 116.

MAN, T., HUPPERT, H. E., LI, L. & GALINDO-TORRES, S. A. 2021a. Deposition morphology of granular column collapses. *Granular Matter,* 23.

MAN, T., HUPPERT, H. E., LI, L. & GALINDO‐TORRES, S. A. 2021b. Finite‐Size Analysis of the Collapse of Dry Granular Columns. *Geophysical Research Letters,* 48.

MANGENEY, A., ROCHE, O., HUNGR, O., MANGOLD, N., FACCANONI, G. & LUCAS, A. 2010. Erosion and mobility in granular collapse over sloping beds. *Journal of Geophysical Research,* 115.

MARSHALL, J. P., HURLEY, R. C., ARTHUR, D., VLAHINIC, I., SENATORE, C., IAGNEMMA, K., TREASE, B. & ANDRADE, J. E. 2018. Failures in sand in reduced gravity environments. *Journal of the Mechanics and Physics of Solids,* 113**,** 1-12.

MAST, C. M., ARDUINO, P., MACKENZIE-HELNWEIN, P. & MILLER, G. R. 2015. Simulating granular column collapse using the Material Point Method. *Acta Geotechnica,* 10**,** 101-116.

MENG, L., LU, P., LI, S., ZHAO, J. & LI, T. 2012. Shape and size effects on the packing density of binary spherocylinders. *Powder Technology,* 228**,** 284-294.

MERUANE, C., TAMBURRINO, A. & ROCHE, O. 2010. On the role of the ambient fluid on gravitational granular flow dynamics. *Journal of Fluid Mechanics,* 648**,** 381-404.

MOLLON, G. & ZHAO, J. 2012. Fourier–Voronoi-based generation of realistic samples for discrete modelling of granular materials. *Granular Matter,* 14**,** 621-638.

MONAGHAN & GINGOLD, R. A. 1983. Shock Simulation by the Particle Method of SPH. *Journal of Computational Physics,* 52**,** 374-389.

NAKASHIMA, H., SHIOJI, Y., KOBAYASHI, T., AOKI, S., SHIMIZU, H., MIYASAKA, J. & OHDOI, K. 2011. Determining the angle of repose of sand under low-gravity conditions using discrete element method. *Journal of Terramechanics,* 48**,** 17-26.

NGUYEN, N. H. T., BUI, H. H. & NGUYEN, G. D. 2020. Effects of material properties on the mobility of granular flow. *Granular Matter,* 22.

NIE, J.-Y., CUI, Y., WU, Z., ZHANG, L. & FANG, J. 2024. DEM study on role of fines in mobility of dry granular flows considering particle size-shape correlation. *Computers and Geotechnics,* 166.

OWEN, P. J., CLEARY, P. W. & MÉRIAUX, C. 2009. Quasi-static fall of planar granular columns: comparison of 2D and 3D discrete element modelling with laboratory experiments. *Geomechanics and Geoengineering,* 4**,** 55-77.

P. G. HOFMEISTER, J. B. A. D. H. 2009. The Flow Of Granular Matter Under Reduced - Gravity Conditions. *AIP Conference Proceedings,* 1145.

PENG, C., WANG, S., WU, W., YU, H.-S., WANG, C. & CHEN, J.-Y. 2019. LOQUAT: an open-source GPU-accelerated SPH solver for geotechnical modeling. *Acta Geotechnica,* 14**,** 1269-1287.

PENG, C., WU, W., YU, H.-S. & WANG, C. 2015. A SPH approach for large deformation analysis with hypoplastic constitutive model. *Acta Geotechnica,* 10**,** 703-717.

POLANÍA, O., CABRERA, M., RENOUF, M. & AZÉMA, E. 2022. Collapse of dry and immersed polydisperse granular columns: A unified runout description. *Physical Review Fluids,* 7**,** 084304.

QUEVEDO, R., MENDOZA, F., AGUILERA, J. M., CHANONA, J. & GUTIÉRREZ-LÓPEZ, G. 2008. Determination of senescent spotting in banana (Musa cavendish) using fractal texture Fourier image. *Journal of Food Engineering,* 84**,** 509-515.

ROCHE, O., ATTALI, M., MANGENEY, A. & LUCAS, A. 2011. On the run-out distance of geophysical gravitational flows: Insight from fluidized granular collapse experiments. *Earth and Planetary Science Letters,* 311**,** 375-385.

ROCKY, E. 2022. ESSS Rocky, Release 2022 R2, DEM Technical Manual, ESSS Rocky DEM, S.R.L.

RUSS, J. C. 2013. *Fractal surfaces*, Springer Science & Business Media.

SHEIKH, B., QIU, T. & AHMADIPUR, A. 2021. Comparison of SPH boundary approaches in simulating frictional soil–structure interaction. *Acta Geotechnica,* 16**,** 2389-2408.

STARON & HINCH 2007. The spreading of a granular mass: role of grain properties and initial conditions. *Granular Matter,* 9**,** 205-217.

STARON, L. & HINCH, E. J. 2005. Study of the collapse of granular columns using two-dimensional discrete-grain simulation. *Journal of Fluid Mechanics,* 545.

STROM, A., LI, L. & LAN, H. 2019. Rock avalanche mobility: optimal characterization and the effects of confinement. *Landslides,* 16**,** 1437-1452.

SU, D., ZHANG, R., LEI, G. & LI, Q. 2022. Experimental and numerical study on collapse of quasi-two-dimensional bilayer granular column. *Advanced Powder Technology,* 33.

SZEWC, K. 2017. Smoothed particle hydrodynamics modeling of granular column collapse. *Granular Matter,* 19.

TAPIA-MCCLUNG, H. & ZENIT, R. 2012. Computer simulations of the collapse of columns formed by elongated grains. *Phys Rev E Stat Nonlin Soft Matter Phys,* 85**,** 061304.

TENG MAN, H. E. H. 2022. Man Teng Influence of Cross-section Shape on Granular Column. *Powder Technology*.

THOMPSON, E. L. & HUPPERT, H. E. 2007. Granular column collapses: further experimental results. *Journal of Fluid Mechanics,* 575**,** 177-186.

TORRES-SERRA, J., RODRÍGUEZ-FERRAN, A. & ROMERO, E. 2021. Study of grain-scale effects in bulk handling using discrete element simulations. *Powder Technology,* 382**,** 284-299.

TREPANIER, M. & FRANKLIN, S. V. 2010. Column collapse of granular rods. *Phys Rev E Stat Nonlin Soft Matter Phys,* 82**,** 011308.

VONNEUMANN, J. & RICHTMYER, R. D. 1950. A Method for the Numerical Calculation of Hydrodynamic Shocks. *Journal of Applied Physics,* 21**,** 232-237.

WANG, C., CUI, Y., NIE, J., HU, B., FANG, J. & CAO, Z. 2024. 3D printing-aided numerical study of particle shape effect on behaviours of dry granular flows interacting with rigid barriers. *Computers and Geotechnics,* 167.

WARNETT, J. M., DENISSENKO, P., THOMAS, P. J., KIRACI, E. & WILLIAMS, M. A. 2014. Scalings of axisymmetric granular column collapse. *Granular Matter,* 16**,** 115-124.

WEI, D., WANG, J., NIE, J. & ZHOU, B. 2018. Generation of realistic sand particles with fractal nature using an improved spherical harmonic analysis. *Computers and Geotechnics,* 104**,** 1-12.

WEI, D., WANG, Z., PEREIRA, J. M. & GAN, Y. 2021. Permeability of Uniformly Graded 3D Printed Granular Media. *Geophysical Research Letters,* 48.

YANG, E., BUI, H. H., DE STERCK, H., NGUYEN, G. D. & BOUAZZA, A. 2020. A scalable parallel computing SPH framework for predictions of geophysical granular flows. *Computers and Geotechnics,* 121.

YANG, S., CHENG, X. & HOU, M. 2024. Numerical and Constitutive Analysis of Granular Column Collapse Experiments Under Reduced-Gravity Conditions. *Microgravity Science and Technology,* 36.

ZENIT, R. 2005. Computer simulations of the collapse of a granular column. *Physics of Fluids,* 17**,** 031703.

ZHANG, B., BI, Y. & HUANG, Y. 2024. Centrifuge modelling of dry granular run-out processes under deflective Coriolis condition. *Journal of Rock Mechanics and Geotechnical Engineering*.

ZHANG, P., DONG, Y., GALINDO-TORRES, S. A., SCHEUERMANN, A. & LI, L. 2021a. Metaball based discrete element method for general shaped particles with round features. *Computational Mechanics,* 67**,** 1243-1254.

ZHANG, R., SU, D., LEI, G. & CHEN, X. 2021b. Three-dimensional granular column collapse: Impact of column thickness. *Powder Technology,* 389**,** 328-338.

ZHANG, X., DING, Y., SHENG, D., SLOAN, S. W. & HUANG, W. 2016. Quasi-static collapse of two-dimensional granular columns: insight from continuum modelling. *Granular Matter,* 18.

ZHAO, J., ZHAO, S. & LUDING, S. 2023. The role of particle shape in computational modelling of granular matter. *Nature Reviews Physics,* 5**,** 505-525.

ZHENG, H., NIU, W., MAO, W. & HUANG, Y. 2024. Effect of gravity on granular material flows. *Computers and Geotechnics,* 170.

ZHOU, B. & WANG, J. 2017. Generation of a realistic 3D sand assembly using X‐ray micro‐computed tomography and spherical harmonic‐based principal component analysis. *International Journal for Numerical and Analytical Methods in Geomechanics,* 41**,** 93-109.

ZHU, R., HE, Z., ZHAO, K., VOWINCKEL, B. & MEIBURG, E. 2022. Grain-resolving simulations of submerged cohesive granular collapse. *Journal of Fluid Mechanics,* 942.

ZOU, Y., MA, G., MEI, J., ZHAO, J. & ZHOU, W. 2022. Microscopic origin of shape-dependent shear strength of granular materials: a granular dynamics perspective. *Acta Geotechnica,* 17**,** 2697-2710.

Publications

Partial results from this dissertation have been published in the following scientific journals and conference proceedings:

Yucheng Li* and Raul Fuentes (2025). Granular column collapse: Analysing the effects of gravity levels. *Computers and Geotechnics,* volume 183, 107207.

Yucheng Li*, Deheng Wei, Ningning Zhang, Raul Fuentes (2024). Effect of basal friction on granular column collapse. *Granular Matters,* 26-62.

Yucheng Li*, Ningning Zhang, Raul Fuentes (2021). Smoothed Particle Hydrodynamics Modelling of Granular Column Collapse. 13th European LS-DYNA Conference 2021, 2021-10-05 - 2021-10-07, Ulm, Germany.

On preparing:

Yucheng Li, Deheng Wei*, Chongpu Zhai, Raul Fuentes. The Role of Particle Shape in Granular Materials Collapse. *Journal of Geophysical Research: Solid Earth*.

Appendix

A. Generalized form of elastic-perfectly plastic model

Here, the general form of the elastic-perfectly plastic model is derived. The definition of total strain rate tensor, which can be divided into elastic and plastic parts, as follows:

$$\dot{\varepsilon}^{\alpha\beta} = \dot{\varepsilon}_{\mathrm{e}}^{\alpha\beta} + \dot{\varepsilon}_{\mathrm{p}}^{\alpha\beta}, \tag{A.1}$$

where the subscripts *e* and *p* present for elastic and plastic components, respectively.

The elastic strain rate tensor can be calculated by generalised Hooke's law:

$$\dot{\varepsilon}_e^{\alpha\beta} = \frac{\dot{s}^{\alpha\beta}}{2G} + \frac{1}{9K}\dot{\sigma}^{rr}\delta^{\alpha\beta}, \tag{A.2}$$

where $\dot{\varepsilon}^{\alpha\beta}$ is the deviatoric stress rate tensor; G and K are the material shear and bulk modulus; $\delta^{\alpha\beta}$ is the Kronecker's delta.

The plastic strain rate tensor can be derived from the plastic flow rule according to:

$$\dot{\varepsilon}_p^{\alpha\beta} = \dot{\lambda}\frac{\partial g}{\partial \sigma^{\alpha\beta}}, \tag{A.3}$$

where $\dot{\lambda}$ is the time rate of the plastic multiplier; g is the plastic potential function.

Substituting Equations (A.2) and (A.3) into Equation (A.1), and rearranging the obtained equation, the generic form of the elastic-perfectly plastic is given by:

$$\dot{\sigma}^{\alpha\beta} = 2G\dot{e}^{\alpha\beta} + K\dot{\varepsilon}^{\gamma\gamma}\delta^{\alpha\beta} - \dot{\lambda}\left[\left(K - \frac{2G}{3}\right)\frac{\partial g}{\partial \sigma^{mm}}\delta^{mn}\delta^{\alpha\beta} + 2G\frac{\partial g}{\partial \sigma^{\alpha\beta}}\right], \tag{A.4}$$

where $\dot{e}^{\alpha\beta} = \dot{\varepsilon}^{\alpha\beta} - \frac{1}{3}\dot{\varepsilon}^{\gamma\gamma}\delta^{\alpha\beta}$ is the deviatoric strain rate tensor; m and n are free indexes, which are independent from α and β.

The plastic multiplier for the elastic-perfectly plastic model can be derived from the consistency condition, which requires the following:

$$df = \frac{\partial f}{\partial \sigma^{\alpha\beta}}d\sigma^{\alpha\beta} = 0. \tag{A.5}$$

where f is the yield function that defines the onset of plastic deformation.

Substituting Equation (A.4) into (A.5), the general form of the time rate of the plastic multiplier can be obtained as,

$$\dot{\lambda} = \frac{\frac{\partial f}{\partial \sigma^{\alpha\beta}}\left[2G\dot{\varepsilon}^{\alpha\beta} + \left(K - \frac{2G}{3}\right)\dot{\varepsilon}^{\gamma\gamma}\delta^{\alpha\beta}\right]}{2G\frac{\partial f}{\partial \sigma^{mn}}\frac{\partial g}{\partial \sigma^{mn}} + \left(K - \frac{2G}{3}\right)\frac{\partial f}{\partial \sigma^{mn}}\delta^{mn}\frac{\partial g}{\partial \sigma^{mn}}\delta^{mn}}. \tag{A.6}$$

Substituting the Mohr-Coulomb yield function *f* and its plastic potential function g into Equation (A.6), the general form of the plastic multiplier reads the following:

$$\dot{\lambda} = \frac{1}{H}\left[3K\frac{\partial f}{\partial I_1}\dot{\varepsilon}^{\gamma\gamma} + 2G\left(\frac{\partial f}{\partial J_2}s^{\alpha\beta} + \frac{\partial f}{\partial J_3}t^{\alpha\beta}\right)\dot{\varepsilon}^{\alpha\beta}\right], \tag{A.7}$$

where *H* and $t^{\alpha\beta}$ are defined as follows:

$$H = 9K\frac{\partial f}{\partial I_1}\frac{\partial g}{\partial I_1} + 4GJ_2\frac{\partial f}{\partial J_2}\frac{\partial g}{\partial J_2} + 6GJ_3\left(\frac{\partial f}{\partial J_2}\frac{\partial g}{\partial J_3} + \frac{\partial g}{\partial J_2}\frac{\partial f}{\partial J_3}\right) + 2G\left(s^{\alpha m}s^{m\beta}s^{\alpha n}s^{n\beta} - \frac{4}{3}J_2^2\right)\frac{\partial f}{\partial J_3}\frac{\partial g}{\partial J_3}, \tag{A.8}$$

$$t^{\alpha\beta} = s^{\alpha m}s^{m\beta} - \frac{2}{3}J_2\delta^{\alpha\beta}. \tag{A.9}$$

B. SPH artificial viscosity

The concept of artificial viscosity was first proposed in one spatial dimension by VonNeumann and Richtmyer (1950) to model flows with shocks, which is nowadays widely used in wave propagation programs. The role of the artificial viscosity is to smooth the shock over several particles. The artificial viscosity term Π_{ij} (Monaghan and Gingold, 1983) is included in the SPH momentum equation. Monaghan type artificial viscosity is used:

$$\Pi_{ij} = \begin{cases} \dfrac{-\alpha c_{ij}\phi_{ij} + \beta\phi_{ij}^2}{\rho_{ij}}, & u_{ij}\cdot x_{ij} < 0 \\ 0, & u_{ij}\cdot x_{ij} \gg 0 \end{cases} \tag{B.1}$$

$$\phi_{ij} = \frac{h_{ij}\boldsymbol{v}_{ij}\cdot\boldsymbol{x}_{ij}}{\left|\boldsymbol{x}_{ij}^2\right| + 0.01h_{ij}^2}, c_{ij} = \frac{c_i + c_j}{2}, \rho_{ij} = \frac{\rho_i + \rho_j}{2}, \tag{B.2}$$

$$h_{ij} = \frac{h_i + h_j}{2}, x_{ij} = x_i - x_j, v_{ij} = v_i - v_j, \tag{B.3}$$

where α and β are the problem dependent tuning parameters. J.J.Monaghan (1994) chose $\alpha = 0.01$, $\beta = 0$ to simulate the free surface flow. Bui et al. (2007) chose $\alpha = 0.01$, $\beta = 1$ for water and $\alpha = 1$, $\beta = 1$ for soil. Here, $\alpha = 0.06$ and $\beta = 1.5$ are chosen based on numerical validation against the experimental study and direct comparison to J.J.Monaghan (1994) and Bui et al. (2007). The speed of sound *c* of the material is calculated according to $c_i = \sqrt{E_i/\rho_i}$. *E* is the Young's modulus of the material.

To make sure that the artificial viscosity parameters are appropriate, we have done a simple simulation ($a = 1$ and $\mu = 0.4$) to validate it also against literature results. We have compared the

effect of different values (α and β) of artificial viscosity on simulation results. The results were compared using deposit morphology and run-out distance (see Figure B.1 and Figure B.2). Our selected values (α=0.06, β=1.5) in our simulations show that the results are similar to those obtained in the literature. Additionally, our model was also validated against experimental results to ensure that the SPH model accurately represent the physical behaviour of the granular column collapse.

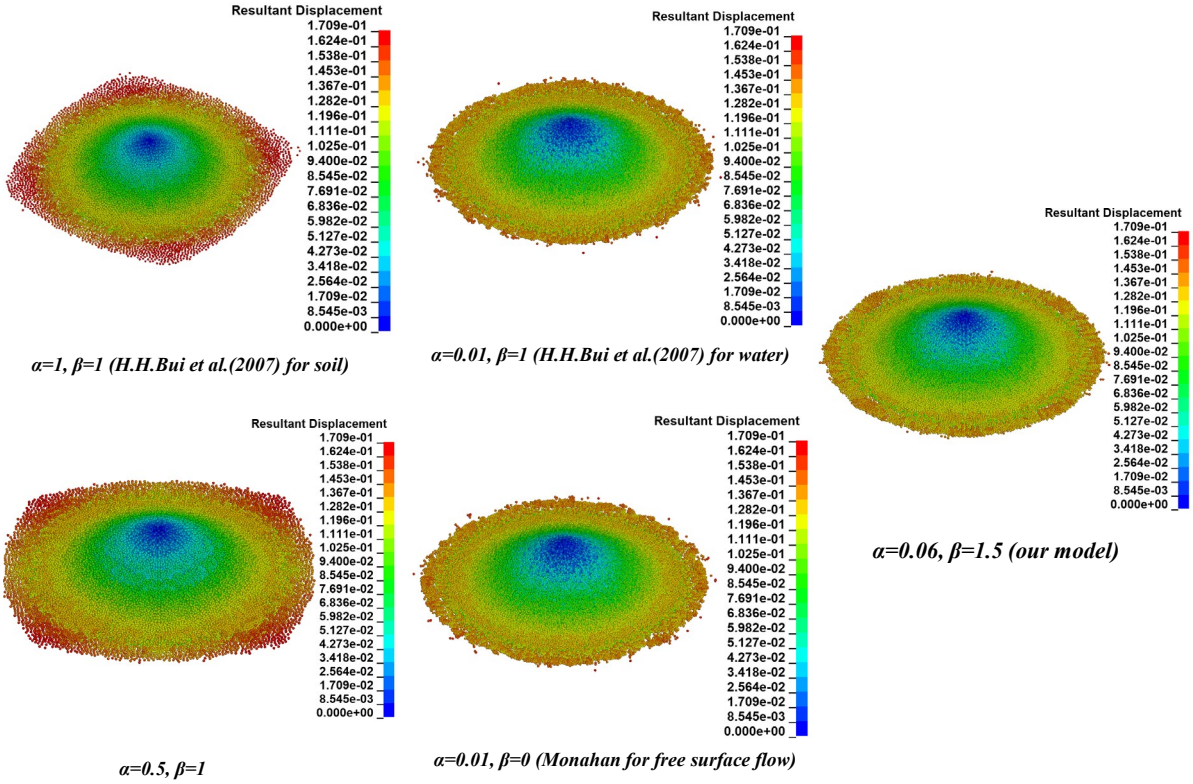

Figure B.1 Comparison of deposit morphology under different α and β.

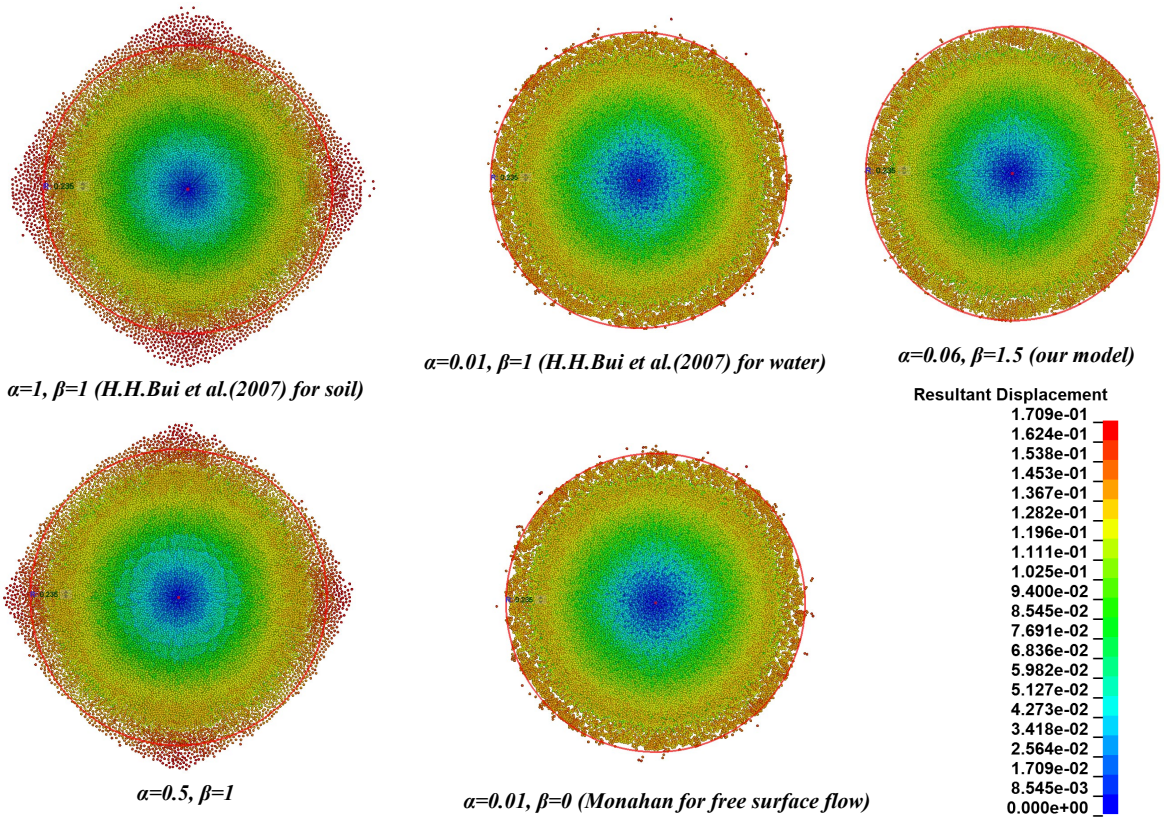

Figure B.2 Comparison of run-out distance under different α and β (same size red circle R=0.235m).

C. Morphology detection method

Figure C.3 shows the method we followed to determine the morphology or deposit regime from our numerical results. For cases where the deposit morphology remains at the initial height with a flat surface at the top, the regime is classified as regime I (e.g., red area in Figure C.3, a = 0.55, μ =0.4). However, if the deposit final height deviates from the initial height, it is classified as either regime II or regime III. For the distinction between regime II and regime III, we inspect the presence of a “double peak”. If the morphological image exhibits a continuous colour transition from warm to cold colours, it is categorized as regime II (e.g., a = 9, μ = 0.35, shown in Figure C.3) as only one peak at the centre occurs. Conversely, if there is a discontinuous colour transition with the presence of a ring area (second peak), it is classified as regime III (e.g., a = 9, μ = 0.3, shown in Figure C.3). This method is highly sensitive, allowing even small differences between regime II and regime III to be detected.

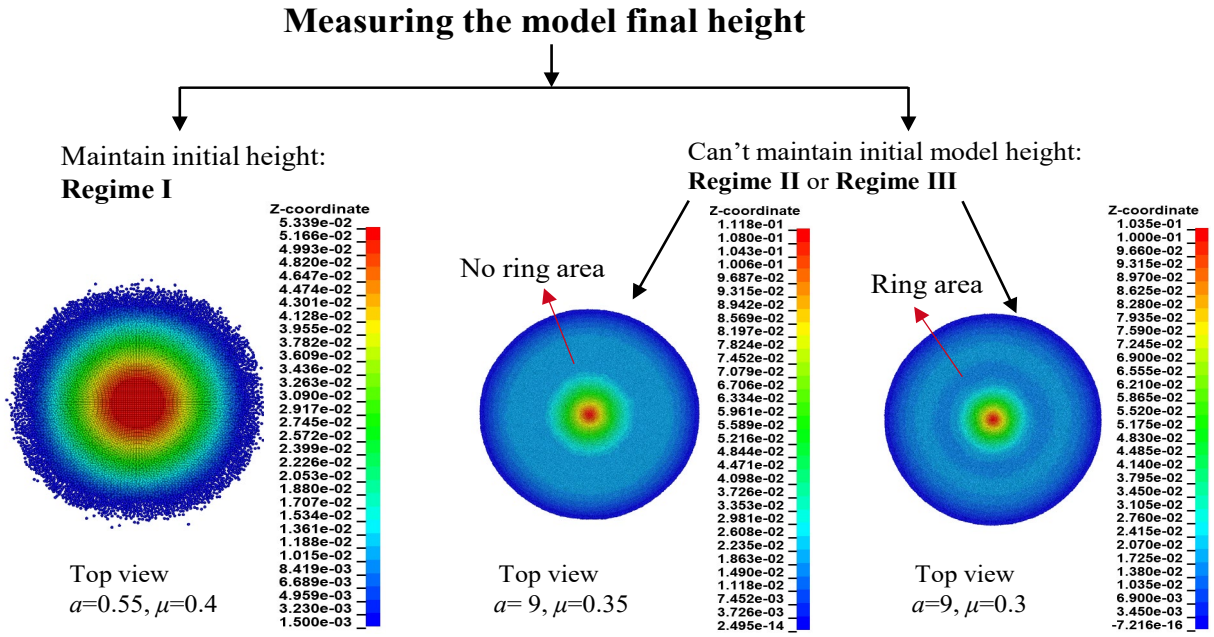

Figure C.3 Methodology for determining the deposit regime in LS-DYNA.

D. Measurement of natural angle of repose

The natural angle of repose was measured as shown in Figure D.4. A funnel is installed on iron support with a fixed height. The deposit disk whose diameter is 10cm is installed on the steel plate and keeps vertical aligned with the axis of the funnel, as shown in Figure D.4(a). Before the test, the fixed top plate should keep horizontal, which was calibrated by a digital level. Final deposit and the angle's measurement was shown in Figure D.4(b). In order to reduce the operational errors, each test was repeated 6 times and obtained the average as the final value.

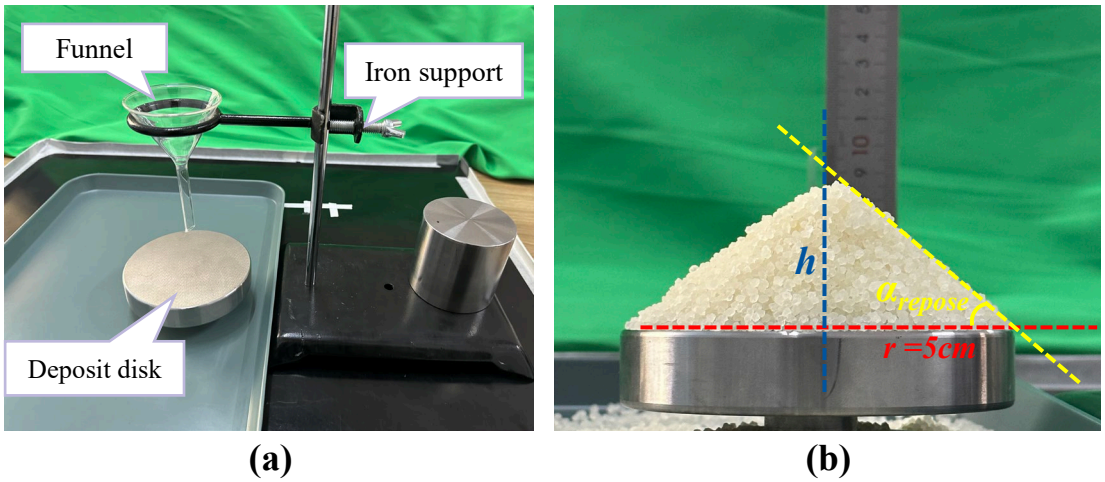

Figure D.4 Measurement procedure of natural angle of repose. (a) Measuring device. (b) final deposit and measurement ($\alpha_{repose}=tan^{-1}\ h/r$).

E. Derivations of SH-based fractal dimension

The SH-based fractal dimension (D_f) to characterise particle morphology.

For one specific degree n, there are 2n+1 complex numbers of SH coefficients to be determined according to Equation (5.1). As a consequence, for the maximum degree n_{max}, there are total number $(n_{max} + 1)^2$ for representing a 3D closed stat-shaped surface. Due to the orthonormal properties of the SH function, the more general calculation of c_n^m to reconstruct or smooth target particle shapes follows the integral

$$c_n^m = \int_0^{2\pi}\int_0^{\pi} \sin\theta \cdot r(\theta,\varphi) \cdot [Y_n^m(\theta,\varphi)]^* d\theta d\varphi. \tag{E.1}$$

Generally, the higher the n_{max} is, the finer morphology features would be represented. Notably, as shown in Figure 5.1(c), the applied n_{max} scales for depicting rougher grain morphology. Zhou and Wang (2017) had proved that SH reconstruction is sufficient to represent the multi-scale morphological features of the sand particle when the maximum SH degree is greater than 15. Therefore, the maximum SH degree was set to 15 in this study.

The amplitude at each SH frequency can be measured by

$$L_n = \sqrt{\sum_{m=-n}^{n} \|c_n^m\|^2}, (n = 0 \cdots 15), \tag{E.2}$$

where $\|\cdot\|$ is the L_2 norm and L_n values are also normalised by L_0 to eliminate the influence of particle volume. Moreover, because L_1 does not influence much the SH-reconstructed particle morphology as that in 2D Fourier transformation (Mollon and Zhao, 2012), L_1 is set to 0. Then, the so-called SH descriptors are defined as:

$$\begin{cases} D_0 = 1 \\ D_n = L_n/L_0, (n = 2,3,4 \cdots) \end{cases}. \tag{E.3}$$

As in Figure 5.1(b). the exponential relations between D_n and n of wide ranges of real particles have been found that:

$$D_n \propto n^{\beta}, \tag{E.4}$$

where $\beta = -2H$ is the slope of the regression plot of log (D_n) versus log (n) was the Hurst coefficient that is related to the Fractal Dimension (D_f) of Fourier transformation by the following expression (Russ 2013):

$$D_f = 3 - H = (6 + \beta)/2. \tag{E.5}$$

By substituting Equation (5.4) into Equation (E.5), the remaining SH descriptors can be quantified by:

$$D_n = D_2 \cdot \left(\frac{n}{2}\right)^{2D_f-6}, \tag{E.6}$$

Random SH coefficients of virtual grains with given D_f and D_2.

Two following important numerical properties of SH coefficients can be deduced from Equations (5.2) and (5.3):

$$c_n^m = (-1)^m \cdot (c_n^m)^*. \tag{E.7}$$

$$c_n^0 \in R. \tag{E.8}$$

The randomness in particle shapes of given D_f and D_2 is in the values of complex SH coefficients. We first generate one set of whole SH coefficients (c'_n) for a particle with stochastic complex numbers, which follow the formula in Equations. (E.7) and (E.8):

$$c'_n = \begin{pmatrix} C'_0 \\ C'_1 \\ \vdots \\ C'_{n-1} \\ C'_n \\ C'_{n+1} \\ \vdots \\ C'_{n_{max}} \end{pmatrix}^T = \cdot \begin{pmatrix} C'_0 \\ \begin{pmatrix} C'^{-1}_1 & C'^{0}_1 & C'^{1}_1 \end{pmatrix}^T \\ \vdots \\ \begin{pmatrix} C'^{-(n-1)}_{n-1} & \cdots & C'^{0}_{n-1} & \cdots & C'^{n-1}_{n-1} \end{pmatrix}^T \\ \begin{pmatrix} C'^{-n}_{n} & \cdots & C'^{0}_{n} & \cdots & C'^{n}_{n} \end{pmatrix}^T \\ \begin{pmatrix} C'^{-(n+1)}_{n+1} & \cdots & C'^{0}_{n+1} & \cdots & C'^{n+1}_{n+1} \end{pmatrix}^T \\ \vdots \\ \begin{pmatrix} C'^{-n_{max}}_{n_{max}} & \cdots & C'^{0}_{n_{max}} & \cdots & C'^{n_{max}}_{n_{max}} \end{pmatrix}^T \end{pmatrix}. \tag{E.9}$$

Then with given D_f and D_2, D_n can be determined, except for $D_1 = 0$. Consequently, the final SH coefficients of target SH coefficients, c_n, is

$$c'_n = \begin{pmatrix} \frac{D_0 \cdot c_0}{\sqrt{\sum_{m=0}^{0} \|c'^m_n\|^2}} \cdot C'_0 \\ \frac{D_1 \cdot c_0}{\sqrt{\sum_{m=-1}^{1} \|c'^m_n\|^2}} \cdot \begin{pmatrix} C'^{-1}_1 & C'^{0}_1 & C'^{1}_1 \end{pmatrix}^T \\ \vdots \\ \frac{D_{n-1} \cdot c_0}{\sqrt{\sum_{m=-(n-1)}^{n-1} \|c'^m_n\|^2}} \cdot \begin{pmatrix} C'^{-(n-1)}_{n-1} & \cdots & C'^{0}_{n-1} & \cdots & C'^{n-1}_{n-1} \end{pmatrix}^T \\ \frac{D_n \cdot c_0}{\sqrt{\sum_{m=-n}^{n} \|c'^m_n\|^2}} \cdot \begin{pmatrix} C'^{-n}_{n} & \cdots & C'^{0}_{n} & \cdots & C'^{n}_{n} \end{pmatrix}^T \\ \frac{D_{n+1} \cdot c_0}{\sqrt{\sum_{m=-(n+1)}^{n+1} \|c'^m_n\|^2}} \cdot \begin{pmatrix} C'^{-(n+1)}_{n+1} & \cdots & C'^{0}_{n+1} & \cdots & C'^{n+1}_{n+1} \end{pmatrix}^T \\ \vdots \\ \frac{D_{n_{max}} \cdot c_0}{\sqrt{\sum_{m=-n_{max}}^{n_{max}} \|c'^m_{n_{max}}\|^2}} \cdot \begin{pmatrix} C'^{-n_{max}}_{n_{max}} & \cdots & C'^{0}_{n_{max}} & \cdots & C'^{n_{max}}_{n_{max}} \end{pmatrix}^T \end{pmatrix}^T . \quad \text{(E.10)}$$

After obtaining c_n, Equation (5.1) is implemented to generate particle surfaces using 1,280 faced icosahedron-geodesic structures. Such generation process is very efficient in producing realistic virtual particle shapes. For more information, please referred to Wei et al. (2018).

Considering the volume element in polar coordinate system, $dV = r \sin\theta \, d\theta \cdot r d\varphi \cdot dr$, V can be rigidly determined (Wei et al., 2021),

$$V = \int_0^{r(\theta,\varphi)} \int_0^{\pi} \int_0^{2\pi} r(\theta,\varphi)^2 \sin\theta d\varphi d\theta dr. \quad \text{(E.11)}$$

By inserting Equation (5.1) into Equation (E.11),

$$V = \frac{C_0^3}{6\sqrt{\pi}} + \frac{3C_0^3}{6} \cdot \sum_{n=2}^{n_{max}} \left(D_2 \cdot \left(\frac{n}{2}\right)^{2D_f-6} \right)^2 = \frac{c_0^3}{6\sqrt{\pi}} (1 + 3R_r^2), \quad \text{(E.12)}$$

where $V_{n=0}$ is the volume of its c_0-determined sphere with radius, $c_0^0 \cdot Y_0^0(\theta,\varphi) = \frac{c_0^0}{2\sqrt{\pi}}$. In our study, $c_0^0 = 0.002\sqrt{\pi}$, so particle radius r = 1mm.

F. The determined method for relative roughness (R_r) of particle

The following deviation process of particle relative roughness (R_r) can be found in the supplementary paper by Wei et al. (2021).

Roughness of one specific particle surface is defined from the Parseval's formula and orthogonality of SH function,

$$MSD = \frac{1}{4\pi}\sum_{n=0}^{\infty}\sum_{m=-n}^{n}\|c_n^m\|^2. \quad \text{(F.1)}$$

Roughness existing on a surface is not meaningless is not meaningless, when it is compared with a specific surface. If the SH coefficients of two compared surfaces are $c_{1,n}$ and $c_{2,n}$, the global differences between them can be defined as root mean square distance (RMSD),

$$RMSD = \sqrt{\frac{1}{4\pi}\sum_{n=0}^{\infty}\sum_{m=-n}^{n}\|c_n^m\|^2}. \quad \text{(F.2)}$$

Due to the periodicity of spherical angles, $\int_0^{2\pi}\int_0^{\pi} r(\theta,\varphi)\,d\theta d\varphi$ is rotational invariant. If the roughness is defined as how different it is from it c_0-determined sphere, we obtain:

$$c_{2,n} = c_{1,n}^0. \quad \text{(F.3)}$$

It is also necessary to normalize the roughness by the c_0-determined sphere:

$$R_r = \frac{\sqrt{\frac{1}{4\pi}\sum_{n=1}^{n_{max}}\sum_{m=-n}^{n}\|c_n^m\|^2}}{c_0^0\cdot Y_0^0(\theta,\varphi)}. \quad \text{(F.4)}$$

where R_r is the defined relative roughness. Then Equations (E.2-3) and (E.5) imported into Equation (E.6), the relations between R_r and D_2 and D_f are:

$$R_r = \frac{\sqrt{\frac{1}{4\pi}\left({L_1}^2+\sum_{n=2}^{n_{max}}\left(c_0^0\cdot D_2\cdot\left(\frac{n}{2}\right)^{2D_f-6}\right)^2\right)}}{c_0^0\cdot Y_0^0(\theta,\varphi)}. \quad \text{(F.5)}$$

Since L_1 is set to zero and $Y_0^0(\theta,\varphi) = \frac{1}{2\sqrt{\pi}}$, R_r reads

$$R_r = \sqrt{\sum_{n=1}^{n_{max}}\left(D_2\cdot\left(\frac{n}{2}\right)^{2D_f-6}\right)^2}. \quad \text{(F.6)}$$

With n_{max} = 15 in this study, it is clear that if two of R_r and D_2 and D_f are known, the third one is determined automatically. Based on 320 faces particles, we summarized the correlation of D_2 and D_f corresponding to R_r in Figure F.5.

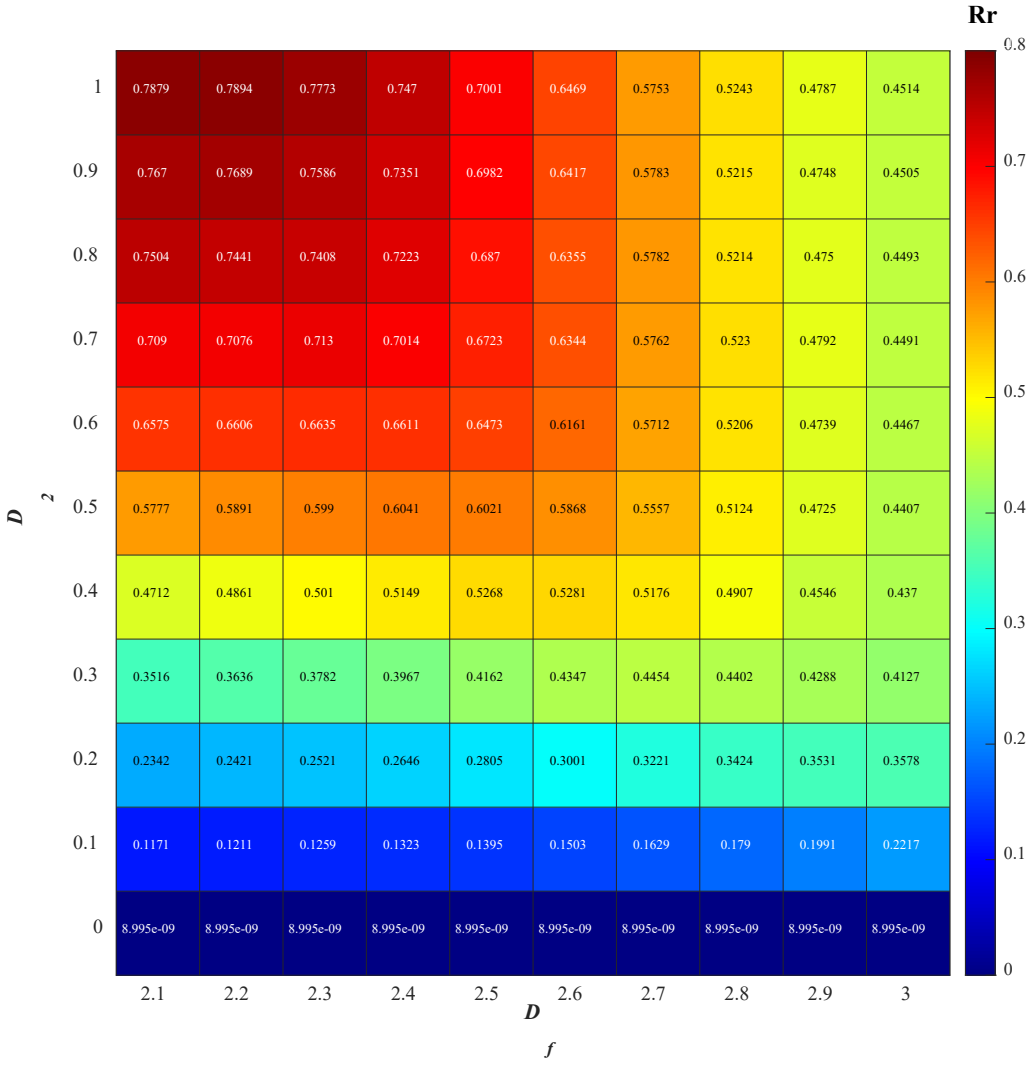

Figure F.5 The effect of D_2 and D_f on R_r.

G. Comparison of number of faces on the particle geometric parameters

The influence of the number of faces on the particle geometric parameters (e.g., sphericity, aspect ratio, roundness, convexity. etc.) was compared. The number of faces per particle ranges from 80 to 20480, resulting in slight variations in particle shape (see Figure G.6(a)). This discrepancy arises from two factors: firstly, the varying number of faces influences the shape, and secondly, the particles are randomly generated from the same D_2 and D_f. We observed that roundness increases as the number of faces increase (see Figure G.6(b)). However, this adjustment only changes particle roundness, minimally affects sphericity, particle aspect ratio, and convexity (see Figure G.6(c)).

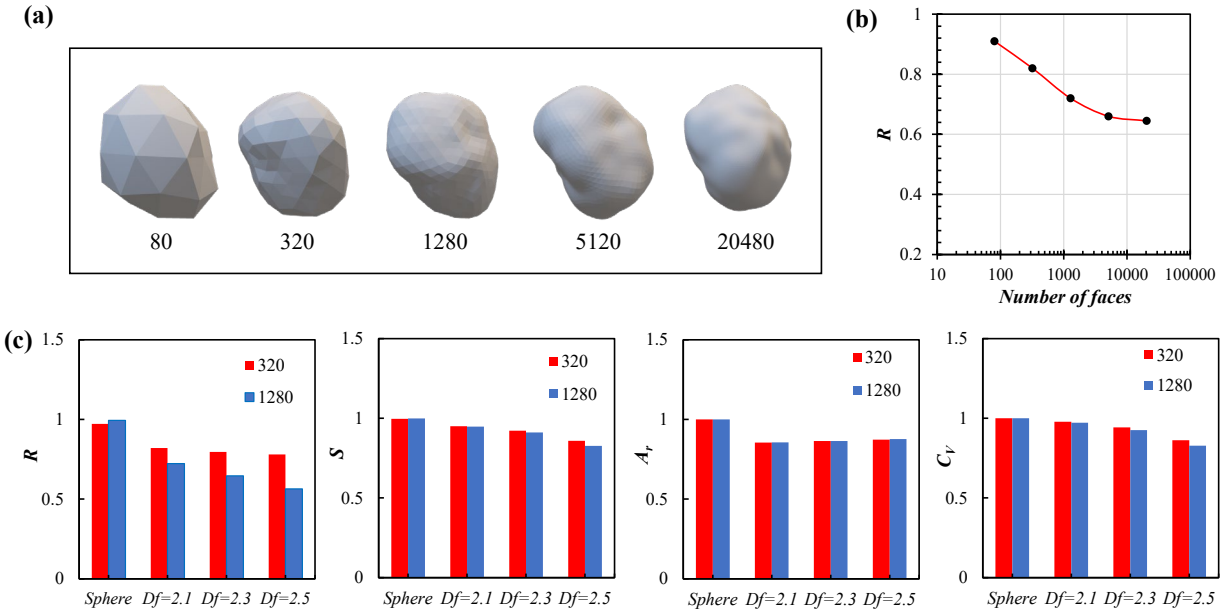

Figure G.6 (a) Typical STL files of shaped particles with D_f = 2.1 and D_2 = 0.1, featuring particle faces ranging from 80 to 20480. (b) the relationship between particle faces and average particle roundness. Roundness (R) quantifies the local mean curvature distribution at corners, calculated as $R_M = \sum(S_L \cdot \frac{K_{in}}{K_{M,l}}) / \sum S_L \,, \forall\, K_{M,l} \leq K_{in}$, where S_L is the area of the *l-th* triangle, of which the mean median curvature value of its three vertices is $K_{M,l}$, and K_{in} is the curvature value of maximum inscribed sphere of the particle. (c) Comparison of particle shape parameters (e.g., roundness, sphericity) between 320 and 1280 faces.